Study of γ rays emitted from giant resonances of ^{12}C and ^{16}O

Iwa Ou
Okayama University
Graduate School of Natural Science and Technology

August 30, 2017

概要

重力崩壊型の超新星爆発では、全種類のニュートリノが平均 10-20MeV のエネルギーを持って放出され、重力崩壊エネルギーの約 99%を宇宙空間へと持ち出す。

これらのニュートリノはスーパーカミオカンデ (水チェレンコフ検出器) や KamLAND(液体シンチレータ検出器) 等のニュートリノ検出器で観測する事ができる。主な信号は荷電カレント相互作用による陽子との逆 β 崩壊反応 ($\bar{\nu}_e + p \rightarrow e^+ + n$) であるが、反電子ニュートリノしか測定できない。一方で 2 番目に多いと期待される信号は、ニュートリノと炭素・酸素原子核の中性カレント (NC) 反応によって放出される γ 線は超新星爆発時に放出されるニュートリノ (超新星ニュートリノ) の検出に有用である。

超新星爆発では全種類のニュートリノが平均エネルギー 10~20MeV を持って放出され、重力崩壊エネルギーの約 99%を宇宙空間へと持ち出す。これらのニュートリノはスーパーカミオカンデ (水チェレンコフ検出器) や KamLAND(液体シンチレータ検出器) 等のニュートリノ検出器で観測する事ができる。主な信号は荷電カレント (CC) 相互作用による逆 β 崩壊反応 ($\bar{\nu}_e + p \rightarrow e^+ + n$) が主な信号であるが、反電子ニュートリノしか検出できない。2 番目に多いと期待される中性カレント (NC) 信号ではミュー型やタウ型の (反) ニュートリノの検出が可能であり、超新星爆発の機構解明において非常に重要である。NC 信号は超新星ニュートリノとの NC 相互作用により酸素・炭素原子核が巨大共鳴状態へと励起された後に放出される γ 線の検出により同定されると理論的に予想されているが、実験的にその放出機構や放出率は確認されていなかった。

そこで、392MeV の陽子ビームと磁気スペクトロメータ"Grand Raiden"を用いて、非弾性散乱反応により原子核を巨大共鳴状態へと励起させ、放出される γ 線を NaI(Tl) シンチレータで同時測定した。実験は大阪大学の核物理研究センターにて行った。その結果以下の新たな知見が得られた。

1. 炭素・酸素原子核の巨大共鳴状態から放出される γ 線のエネルギースペクトル・放出率が世界で初めて系統的に、励起エネルギーの関数として初めて測定された。

2. 放出される γ 線のエネルギースペクトルから、原子核は核子崩壊後に娘核の励起状態へ遷移し、その後に γ 線を放出する事が確認された。

3. γ 線放出率は 2 核子を放出するエネルギー閾値までは、励起エネルギーの上昇に伴い上昇し ($\Gamma_\gamma/\Gamma(E_x)$=0.69±0.05 for ^{12}C at E_x=27 MeV and 0.87±0.10 for ^{16}O at E_x=23 MeV)、その後は次第に減少する傾向が測定された。

4. γ 線放出率の散乱角依存性を調べ、3 度付近での γ 線放出率は 0.5 度付近よりも大きい値を持つことがわかった。0 度付近の散乱ではスピン非反転型の励起 (GDR) が支配的であり、3 度付近においてはスピン反転型の励起 (SDR) が支配的であることが他の実験データで測定されている。このことから SDR は GDR よりも大きい γ 線放出率を持つ、つまり娘核の励起状態へと崩壊し易いと示唆される。

5. 炭素原子核の崩壊モデル計算を多数の核子を放出するエネルギー閾値まで行い、測定値を定性的に再現する事が確認された。

6. 測定された放出率を用いて、超新星爆発時のニュートリノ 観測にて期待される NC 信号数の見積もりを行った。

Abstract

A core-collapse supernova emits all types of neutrinos with mean energy of 10∼20 MeV, which carry away nearly 99% of the total gravitational energy. These neutrinos can be detected by neutrino detectors such as Super Kamiokande (water, H_2O) and KamLAND (liquid scintillator, $C_{12}H_{26}$). The main signal is induced by charged-current (CC) inverse β-decay reaction with proton ($\bar{\nu}_e + p \rightarrow e^+ + n$) and sensitive only to $\bar{\nu}_e$. The 2nd largest signal comes from the neutral-current (NC) inelastic scattering of neutrinos and anti-neutrinos with ^{16}O and ^{12}C. NC events are dominated by ν_μ and ν_τ and their anti-particles, since their mean energies are higher than those of ν_e and $\bar{\nu}_e$. Therefore, the detection of NC events is important for understanding of the underlying mechanism of supernova explosion.

^{12}C and ^{16}O can be excited to giant resonances through NC ν-^{12}C and ν-^{16}O inelastic scatterings. NC events can be identified by detecting γ-ray emitted from these giant resonances. However, there have been no systematic experimental data of the γ-ray emission from giant resonances of ^{16}O and ^{12}C.

We have carried out an experiment at RCNP (Osaka Univ.) in 2014 to measure γ rays from giant resonances of ^{16}O and ^{12}C using 392 MeV proton beam and magnetic spectrometer "Grand Raiden" to excite the nuclei to the giant resonances, and an array of NaI(Tl) γ-ray counters.

The results are summarized as follows.

1. The energy spectrum of γ rays from giant resonances of ^{12}C and ^{16}O and the emission probability ($\Gamma_\gamma/\Gamma(E_x)$) have been measured for the first time as a function of excitation energy (E_x).

2. The γ-ray energy spectra clearly show that γ rays are emitted from the excited states of the daughter nuclei after particle decay of the parent nuclei.

3. The γ-ray emission probability increases as excitation energy up to $\Gamma_\gamma/\Gamma(E_x)$=0.69±0.05 for ^{12}C at E_x=27 MeV and 0.87±0.10 for ^{16}O at E_x=23 MeV until the energy threshold for two nucleons decay, and then decreases gradually.

4. The γ-ray emission probability has been further estimated for each proton scattering angle ($\theta_p = 0^\circ \sim 3^\circ$) for 16 MeV< E_x <26 MeV. For $E_x > 20$ MeV, it is found that it increases as the scattering angle. Previous experiments found that non-spin-flip dipole excitation (GDR) dominates at scattering angle around 0°, while spin-flip dipole excitation (SDR) dominates at scattering angle around 4°. Considering the previous results, our data suggest qualitatively that SDR has larger γ-ray emission probability than GDR.

5. Decay model calculation has been performed for ^{12}C until the energy threshold for multi-nucleon decay and compared to the experimental data. The decay model successfully reproduces the data qualitatively.

6. Using the present results, the number of NC events from a core-collapse supernova explosion has been estimated.

Contents

Chapter 1

Introduction

1.1 Nuclear structure and giant resonance

Nuclear structures have been studied by variety of nuclear reactions. From those we know nucleus which consists of protons and neutrons (nucleons) shows both independent-particle behavior and collvetive. The former behavior gives the shell model structure just as arrangement of electrons in atoms and the latter gives giant resonance.

In Fig.1.1, a typical response of a nucleus to the scattering by an incident proton is shown as a function of energy transfer to the nucleus (ω) [1]. The first peak seen at 0 MeV is the elastic scattering where the proton is scattered by the mean field of the nucleus and all the nucleons of the nucleus stay in the lowest levels (Fig.1.2.a). Up to 10 MeV the nucleus responds through the simple states where only one or few nucleons are excited (Fig.1.2.b). In the energy range between 10 and 30 MeV several broad peaks are seen. These broad peaks are so called "giant resonances" and correspond to a collective motion involving all the particles in the nucleus where the energy of the incident proton is transferred to the system as vibrations or rotations (Fig.1.2.c).

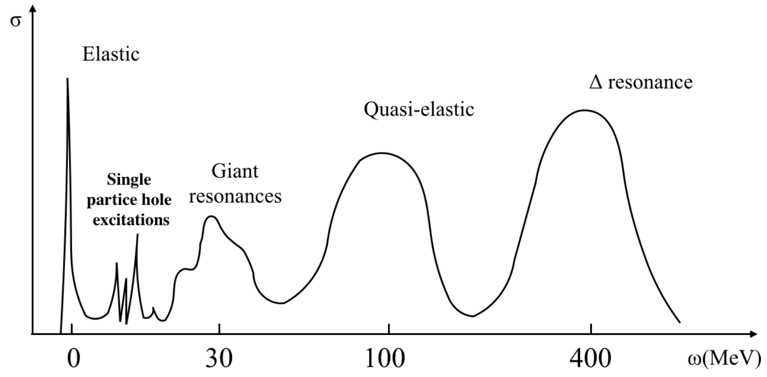

Figure 1.1: Typical response of a nucleus to the scattering of a particle.

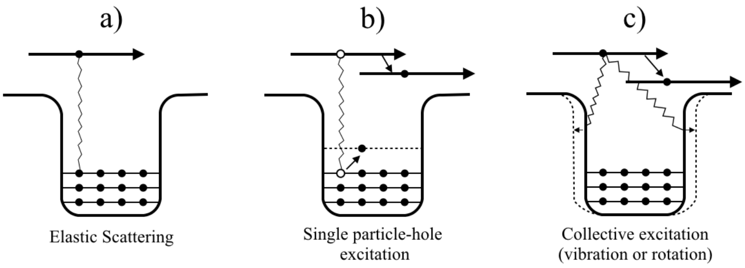

Figure 1.2: Schematic figure of nuclear reactions.

1.1.1 Scattering theory and optical potential

Consider a scattering process of a particle by the mean field created by a nucleus [2, 3]. The Schrödinger equation

$$\{-\frac{\hbar^2}{2\mu}\nabla^2 + V_c(r)\}\psi(\boldsymbol{r}) = E\psi(\boldsymbol{r}), \tag{1.1}$$

where μ is the reduced mass, V_c is an one-body central nuclear potential, E is the total energy and r is the relative coordinate, can be solved using a boundary condition

$$\psi(\boldsymbol{r}) \to e^{ikz} + f(\theta)\frac{e^{ikr}}{r}, \quad (r \to \infty). \tag{1.2}$$

The first term corresponds to the incoming plane wave in the z-axis and the second to the outgoing wave. $f(\theta)$ is called a scattering amplitude with a unit of length and is related to the differential cross section by $d\sigma/d\Omega = |f(\theta)|^2$. Applying partial wave expansion, asymptotic form

$$\begin{aligned} e^{ikz} &\to \frac{1}{2irk}\sum_l (2l+1)\{e^{ikr} - (-1)^l e^{-ikr}\}P_l(cos\theta), \quad (r \to \infty), && (1.3) \\ f(\theta) &\to \frac{1}{2ik}\sum_l (2l+1)(S_l - 1)P_l(cos\theta), \quad (r \to \infty), && (1.4) \end{aligned}$$

can be derived where P_l is the Legendre function and $S_l - 1$ is the coefficient of the expansion. Inserting these into Eq.(1.2), one can write the wave function as

$$\psi(\boldsymbol{r}) \to \frac{1}{2irk}\sum_l (2l+1)\{S_l e^{ikr} - (-1)^l e^{-ikr}\}P_l(cos\theta) \quad (r \to \infty). \tag{1.5}$$

By comparing Eq.(1.4) and Eq.(1.5), S_l can be understood as the distortion effect in the incoming plane wave by the mean field of the nucleus, therefore, called scattering matrix.

An absorption effect on the incoming wave can be considered by introducing an imaginary part to the potential as

$$U(r) = V(r) + iW(r). \tag{1.6}$$

Inserting it into the Schrödinger equation (Eq.(1.1)), mulitplying by ψ^* from left and taking the imaginary part, one obtains

$$\nabla \boldsymbol{j}(\boldsymbol{r}, t) + \frac{\partial}{\partial t}\rho(\boldsymbol{r}, t) = \frac{2}{\hbar}W(\boldsymbol{r})\rho(\boldsymbol{r}, t), \tag{1.7}$$

where ρ and $\boldsymbol{j}$ are the charge density and the current density, respectively,

$$\rho = \psi^* \psi, \quad \boldsymbol{j}(\boldsymbol{r}, t) = \frac{\hbar}{2i\mu}(\psi^* \nabla \psi - \nabla \psi \psi^*).$$

The incoming particles are absorbed per unit time by the imaginary potential, $2|W\boldsymbol{r}|/\hbar$. This one-body potential $U(r)$ is called optical potential. A general form is the sum of central part and spin($\boldsymbol{\sigma}$)-orbital($\boldsymbol{l}$) part as

$$\begin{aligned} U(r) &= U_c(r) + U_{so}(r)\boldsymbol{\sigma} \cdot \boldsymbol{l}, & (1.8) \\ U_c(r) &= V_{coul} - V f_0(r) - iW f_w(r) + 4iW_s \frac{d}{dr} f_{ws}(r), & (1.9) \\ U_{so}(r) &= (\frac{\hbar^2}{m_\pi c})^2 \frac{1}{r} [V_{so} \frac{d}{dr} f_{vso}(r) + iW_{so} \frac{d}{dr} f_{wso}(r)], & (1.10) \\ & & (1.11) \end{aligned}$$

where V_{coul} is a Coulomb potential. $f_i(r)$ has the Woods-Saxon form as

$$f_i(r) = \frac{1}{1 - \exp[\frac{r - r_i A^{1/3}}{a_i}]}, \tag{1.12}$$

where r_i is the radius parameter and a_i is the diffuseness parameter. The parametrization of optical potential is determined phenomenologically by fitting to the elastic scattering data. The optical potential considering mass dependence and energy dependence is called global optical potential. In Fig.1.3 the angular distribution of elastic scattering cross section of proton on ^{12}C at 398 MeV [4] (black dotted point) was compared with a global optical potential calculation (dashed red line) [5]. The global potential reproduces the data very well and was used for the distorted wave impulse approximation as described in the next section.

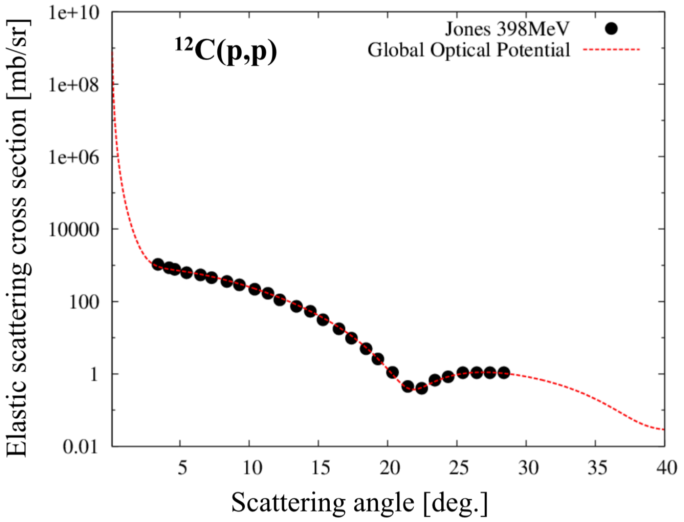

Figure 1.3: Angular distribution of elastic scattering of proton on ^{12}C at 398 MeV. Data (black dotted point) was taken from Jones *et al.* [4] and global optical potential calculation (red dashed line) [5].

1.1.2 Distorted wave Born approximation (DWBA)

In the case for high energy inelastic proton scattering where the interaction part is relatively small, projectile interact with the nucleon in the nucleus only one or few times. This process is classified as direct reaction. Then the differential cross section of $X(a,b)Y$ reaction can be described simply by the plane wave Born approximation as

$$\begin{aligned} \frac{d\sigma}{d\Omega} &= \frac{M_a M_b}{(2\pi\hbar)^2}\frac{k_b}{k_a}|T|^2, && (1.13)\\ T &= \int e^{-i\boldsymbol{k}_b\cdot\boldsymbol{r}}\langle Y|V|X\rangle e^{i\boldsymbol{k}_a\cdot\boldsymbol{r}}d\boldsymbol{r} && (1.14)\end{aligned}$$

where M_a (M_b) is the reduced mass in the entrance (exit) channel, k_i (k_f) is the incoming (outgoing) momenta, V is the interaction potential and T is the transition matrix element (T-matrix). In the plane wave Born approximation, the distortion effect of the wave function by the interaction is ignored. This distortion effect can be taken into account by using the distorted incoming wave $\phi_{aX}(\boldsymbol{k}_a,\boldsymbol{r})$ by the optical potential $U_{aX}(\boldsymbol{r})$ at the entrance channel and the distorted outgoing wave $\phi_{bY}(\boldsymbol{k}_b,\boldsymbol{r})$ by $U_{bY}(\boldsymbol{r})$ at the exit channel. This approximation is known as the distorted wave Born approximation (DWBA).

The DWBA gives T-matrix as

$$T = \int \phi^*_{bY}(\boldsymbol{k}_b,\boldsymbol{r})\langle Y|V|X\rangle\phi_{aX}(\boldsymbol{k}_a,\boldsymbol{r})d\boldsymbol{r}. \tag{1.15}$$

The incoming distorted wave $\phi_{aX}(\boldsymbol{k}_a,\boldsymbol{r})$ can be easily derived by solving the Schrödinger equation using the optical potential $U_{aX}(\boldsymbol{r})$ which reproduce the elastic scattering cross section ($X(a,a)X$) in the entrance channel as

$$\{-\frac{\hbar^2}{2M_X}\boldsymbol{\nabla}^2 + U_{aX}(\boldsymbol{r})\}\phi_{aX}(\boldsymbol{k}_a,\boldsymbol{r}) = E_{aX}\phi_{aX}(\boldsymbol{k}_a,\boldsymbol{r}),\ E_{aX} = \frac{\hbar^2 k_a^2}{2M_{aX}}. \tag{1.16}$$

$\phi_{bY}(\boldsymbol{k}_b,\boldsymbol{r})$ can be also derived in the same way.

For the inelastic scattering $X(a,a')X'$, the differential cross section is given by

$$\begin{aligned} \frac{d\sigma}{d\Omega} &= \frac{M_a^2}{(2\pi\hbar)^2}\frac{k_f}{k_i}|T_{if}|^2, && (1.17)\\ T &= \int \phi^*_{fX}(\boldsymbol{k}_f,\boldsymbol{r})\langle X'|V|X\rangle\phi_{iX}(\boldsymbol{k}_i,\boldsymbol{r})d\boldsymbol{r}. && (1.18)\end{aligned}$$

where $i(f)$ denotes the initial (final) state of the nucleus.

1.1.3 Giant resonance

The schematic picture of a typical and the most well-known giant resonance is shown in Fig.1.4. In this mode, all the neutrons oscillate against all the protons. This vibration mode is known as giant dipole resonance (GDR). Historically, GDR was the first giant resonance measured through (γ, n) reaction in 1937 by Bothe and Gentner [6]. GDR is also measured from light nuclei such as ^{4}He to heavy nuclei such as ^{238}U [1, 2, 7].

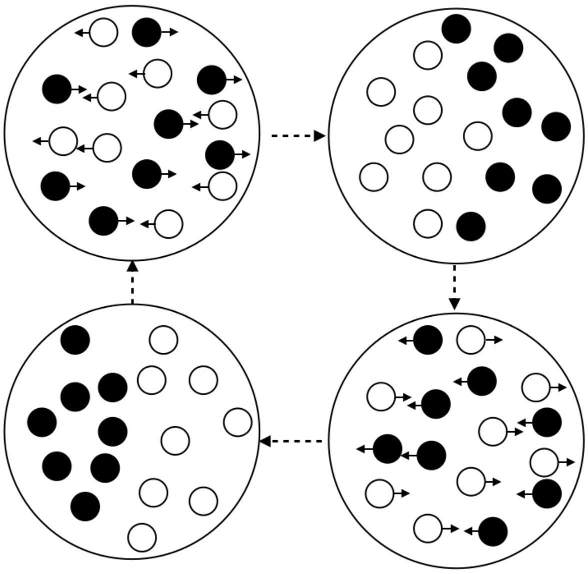

Figure 1.4: Schematic picture of giant dipole resonance. Open circles denote neutrons and filled circles denote protons.

Giant resonances can be classified by the quantum numbers of each collective mode; multipolarity (L), Spin (S) and isospin (T) [7]. Example of various collective modes with $\Delta L = 0$ (monopole) and $\Delta L = 1$ (dipole) and $\Delta L = 2$ (quadrupole) are shown in Fig.1.5.

In electric ($\Delta S = 0$) and isoscalar (ΔT =0) modes, neutrons and protons oscillate in the same phase with a multipole pattern. While in electric ($\Delta S = 0$) and isovector ($\Delta T = 1$) modes, neutrons and protons oscillate in the opposite phases against each other.

In magnetic ($\Delta S = 1$) isoscalar (ΔT =0) modes, nucleons with spin up oscillate against nucleons with spin down with a multipole pattern. In magnetic ($\Delta S = 1$) isovector ($\Delta T = 1$) modes, protons with spin up oscillate against neutrons with spin down and vice versa.

Sum rule

In quantum mechanics, a resonance can be understood as a transition from the ground state to the collective states. This means a collective state is a coherent superposition of all possible particle-hole states for a given multipolarity and parity. Consequently, the total transition strength is limited by a sum rule which depends only on the ground-state properties.

For a hermitian operator F, the ground state $|0\rangle$ and an excited state $|n\rangle$, the strength function of S_F can be written as

$$S_F(\omega) = \sum_n |\langle n|F|0\rangle|^2 \delta(\omega - \omega_n) \tag{1.19}$$

where ω denotes the excitation energy ($E_n - E_0$) and natural unit with $\hbar = c = 1$ is taken. p-th moment of $S_F(\omega)$ is defined as

$$m_p = \int S_F(\omega)\omega^p d\omega = \sum_n |\langle n|F|0\rangle|^2 (E_n - E_0)^p. \tag{1.20}$$

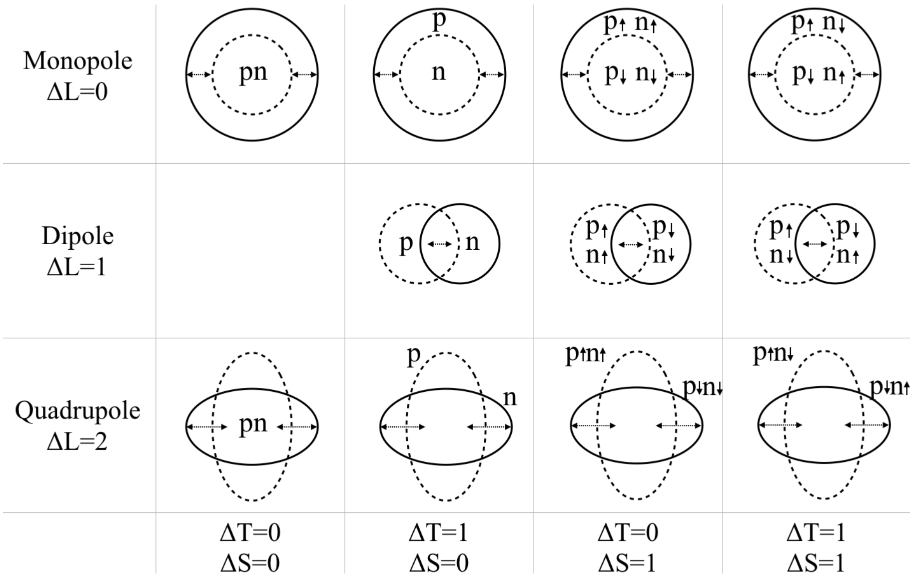

Figure 1.5: Categorization of giant resonances by quantum numbers.

If the p is odd, m_p can be rewritten by the commutator relation of F and H. For example, m_1 can be written using the completeness of the states ($\sum_n |n\rangle\langle n| = 1$) as

$$\begin{aligned} m_1 &= \sum_n |\langle n|F|0\rangle|^2(E_n - E_0) \\ &= \frac{1}{2}\sum_n \{\langle 0|F|n\rangle\langle n|(E_n - E_0)F|0\rangle - \langle 0|(E_0 - E_n)F|n\rangle\langle n|F|0\rangle\} \\ &= \frac{1}{2}\sum_n \{\langle 0|F|n\rangle\langle n|HF - HF|0\rangle - \langle 0|HF - FH|n\rangle\langle n|F|0\rangle\} \\ &= \frac{1}{2}\sum_n \{\langle 0|F|n\rangle\langle n|[H,F]|0\rangle - \langle 0|[H,F]|n\rangle\langle n|F|0\rangle\} \\ &= \frac{1}{2}\langle 0|[F,[H,F]]|0\rangle. \end{aligned} \tag{1.21}$$

This means m_p can be calculated from the expected value of the ground state by the double commutator, even without the specific information of $|n\rangle$.

For example, the transition operator for a isovector dipole resonance is given as

$$F = \sum_{i=1}^{A} t_z(z_i - R_z), \tag{1.22}$$

with $t_z = +1/2$ for protons and $-1/2$ for neutrons, R_z to be z-axis component of the center of mass coordinate. Using the commutator relation between the H and F, one gets

$$m_1 = \frac{NZ}{2A}\frac{\hbar^2}{m}(1 + K), \tag{1.23}$$

where N and Z is the number of neutrons and protons of a nucleus and $A = N + Z$. The first and the second terms in Eq.(1.23) denote the contributions from the kinetic energy and the interaction, respectively. The sum rule for a photo-absorption cross section is given as

$$\sigma_{total} = \frac{4\pi^2 e^2}{\hbar c} \sum_n |\langle n|F|0\rangle|^2 (E_n - E_0) = \frac{2\pi^2 e^2 \hbar}{mc} \frac{NZ}{A}(1+K). \tag{1.24}$$

The factor (N/A) is due to c.m. correction. For $K = 0$, this is known as Thomas-Reiche-Kuhn (TRK) sum rule.

Decay of giant resonance

Since giant resonances are located above the particle separation energies, a nucleus excited to the giant resonances may decay into either the ground states or excited states of daughter nuclei by particle emission (p, n, d and α), namely, hadronic decays. Level diagrams of ^{12}C and ^{16}O and their daughter nuclei after nucleon emission are shown in Fig.1.6 [8]. When the parent nucleus decays to the excited states of daughter nuclei below their particle emission threshold, the daughter nuclei further decay to their ground states by γ-ray emission [9]. Only proton and neutron decays are shown in the figure. For isoscalar excitation (ΔT = 0), alpha decay is the dominant decay due to the lower separation energy, while it is forbidden for isovector excitation (ΔT =1) due to the isospin conservation. The separation energies (S_i) for various decay channels (i) of ^{12}C and ^{16}O are listed in Tab.1.1 and Tab.1.2. Although the authors of Ref.[9] have calculated the emission probability of γ rays for this process, there has been no systematic experimental data, therefore, this process has not been confirmed experimentally.

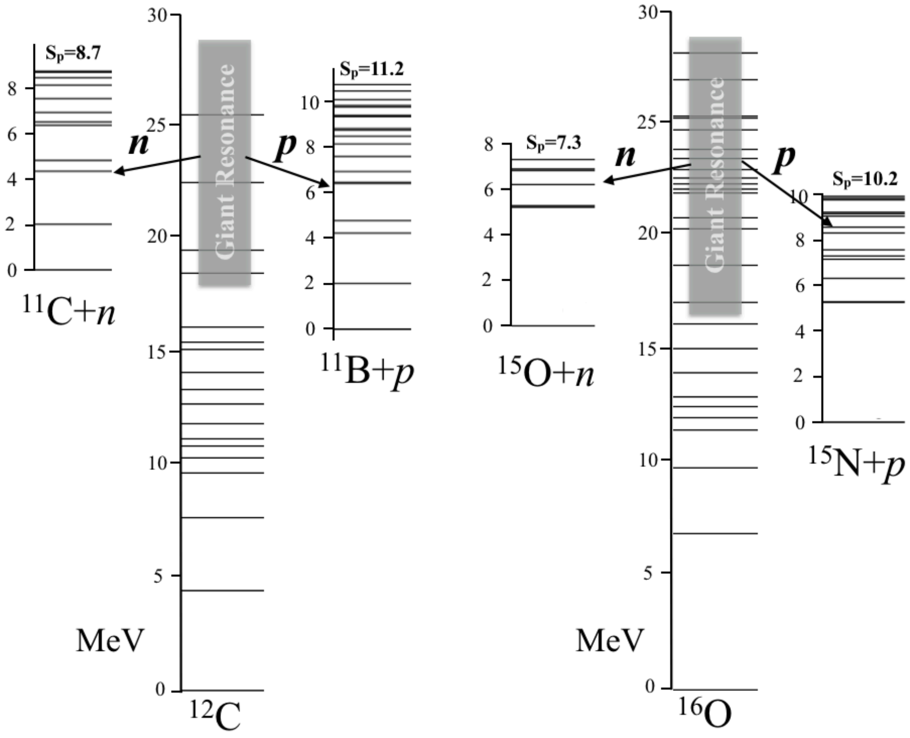

Figure 1.6: Level diagram of ^{12}C (left) and ^{16}O (right) and their daughter nuclei after nucleon emission. S_p denotes the proton emission threshold of daughter nuclei in MeV.

Table 1.1: Separation energies of ^{12}C for various decay channels.

Decay channel	Separation energy [MeV]
$\alpha +^{8}$ Be	7.37
$p +^{11}$ B	15.96
$n +^{11}$ C	18.72
$d +^{10}$ B	25.19
$2p +^{10}$ Be	27.19
$t +^{9}$ B	27.37
$p + n +^{10}$ B	27.41
$2n +^{10}$ C	31.84

Table 1.2: Separation energies of ^{16}O for various decay channels.

Decay channel	Separation energy [MeV]
$\alpha +^{12}$ C	7.16
$p +^{15}$ N	12.13
$n +^{15}$ O	15.66
$d +^{14}$ N	20.74
$2p +^{14}$ C	22.33
$p + n +^{14}$ N	22.96
$t +^{13}$ N	25.03
$2n +^{14}$ O	28.89

1.1.4 Theory of decay model

The excited nucleus can decay via two modes:
1) Hadronic decay: The excited nucleus A* decays into either ground state or excited states of daughter nuclei B by particle emission via strong interaction. The excited daughter nuclei (B^*) can further de-excite by γ-ray emission. This is the prominent decay mode as already mentioned in the previous section.
2) Electromagnetic decay: The excited nucleus A* can always directly decay to their ground state (A) with high energy γ-ray emission via electromagnetic interaction. This rate is smaller than that of the hadronic decay if A* is located above the particle emission threshold, since the EM coupling constant (α_{EM}) is 1/137 of the strong coupling constant (α_s).

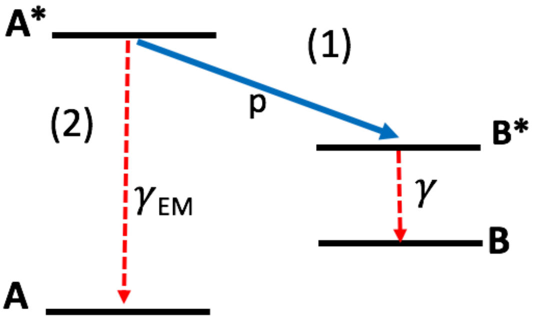

Figure 1.7: Different decay modes for excited nuclei.

The total decay width (Γ) is given by

$$\Gamma = \Gamma_{EM} + \Gamma_{had}. \tag{1.25}$$

The γ-decay width is given by

$$\Gamma_\gamma = \Gamma_{EM} + \Gamma_{had}(E_x \to B^*) \times Br(B^* \to \gamma), \tag{1.26}$$

where Br is the γ-ray branching ratio of daughter nuclei. The γ-ray emission probability is given as

$$\frac{\Gamma_\gamma}{\Gamma} \approx \frac{\Gamma_{had}(E_x \to B^*) \times Br(B^* \to \gamma)}{\Gamma_{had}}, \tag{1.27}$$

where Γ_{EM} is neglected since Γ_{EM}/Γ is O(10^{-4}) [1]. It further simplifies as,

$$\frac{\Gamma_\gamma}{\Gamma} \approx P(E_x \to B^*) \times Br(B^* \to \gamma), \tag{1.28}$$

where $P(E_x \to B^*)$ is calculated using decay model and $Br(B^* \to \gamma)$ is well known [8].

In this Section, the assumptions and formulae for the decay model are described. A compound nucleus is assumed to be formed in statistical equilibrium with respect to all degrees of freedom. Then Hauser-Feshbach formalism is used for the calculation of decay rate of compound nucleus by the particle emission [10]. The width (Γ) for the decay from compound nucleus x (with excitation energy E_x, spin J_x, parity π_x) to residual nucleus 1 (with E_1, J_1, π_1) by emitting a particle 2 is proportional to

$$\Gamma \propto I.C.G. \times \phi_2 \times \sum_{S=|J_1-s_2|}^{J_1+s_2} \sum_{L=|J_x-S|}^{J_x+S} T_L, \tag{1.29}$$

where ϕ_2 is the two-body phase-space factor, T_L is the transmission coefficient for the the decay ($x \to 1+2$). Eq.(1.25) has been modified by adding Isospin Clebsch-Gordon Coefficients (I.C.G.) for isospin conservation. s_2 is the spin of particle 2 and S is the channel spin ($|J_1-s_2| < S < J_1+s_2$). All the above mentioned factors will be discussed in detail.

Transmission coefficient

The Schrödinger equation for the relative motion of two-body collision system in potential V' is given by

$$\left(-\frac{\hbar}{2\mu} \bigtriangledown^2 + V'\right) \phi(r) = E'\phi(r), \tag{1.30}$$

where E' is the energy of the system and μ stands for the reduced mass defined by

$$\mu = \frac{m_p m_t}{m_p + m_t}, \tag{1.31}$$

where m_p (m_t) is the mass of the projectile (target). The radial part of the Schrödinger equation for the orbital angular momentum quantum number l and the total angular quantum number j can be written as

$$\left(\frac{d^2}{dr^2} - \frac{l(l+1)}{r^2} + k^2 + V\right) \phi_l^j(r) = 0, \tag{1.32}$$

where k is the wave number as

$$k^2 = \frac{2\mu E'}{\hbar^2}, \qquad V = -\frac{2\mu V'}{\hbar^2}. \tag{1.33}$$

The asymptotic form of the wave function $\phi_l^{(j)}$ in Eq.(1.28) can be written as

$$\phi_l^{(j)}(r) \to u_l^{(j)}(\rho) = \frac{i}{2}[u_l^{(-)}(\rho) - \eta_l^{(j)} u_l^{(+)}(\rho)]e^{i\sigma_l}, \qquad \rho = kr, \tag{1.34}$$

where the functions $u_l^{(-)}$ and $u_l^{(+)}$ stands for incoming and outgoing waves. They are given by the Coulomb wave functions $G_l(\rho)$ and $F_l(\rho)$,

$$u_l^{(\pm)} = G_l(\rho) \pm F_l(\rho). \tag{1.35}$$

The coefficient $\eta_l^{(j)}$ is the quantity that relates with the scattering phase shift. Solving the Schrödinger equation for asymptotic wave function, one gets transmission coefficient as

$$T_l^{(j)} = 1 - |\eta_l^{(j)}|^2. \tag{1.36}$$

Transmission coefficients depend only on the energy and the orbital angular momentum. The summation over L is restricted by parity selection rule $\pi = \pi_1\pi_2(-1)^L$. The program code CASCADE[10] numerically solves the Schrödinger equation to obtain T_l as function of l. The code provides various choices of optical potential for which the Schrödinger equation could be solved. The optical model potentials for neutron [11], proton [12] and alpha [13] were used and transmission coefficients for each decay mode were obtained.
The validity of the code has been checked by comparing the transmission coefficients with other calculations [14] as shown in Fig.1.8.

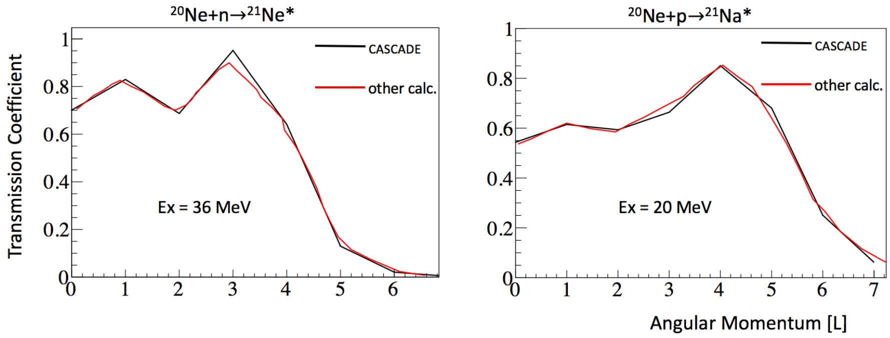

Figure 1.8: Transmission coefficients as a function of angular momentum from CASCADE [10] (black) and other calculations [14] (red).

Phase-space factor

A phase-space factor is the number of states per unit volume in the momentum space available in the final state. The element of n-body phase-space is given by

$$d\phi_n(P; p_1, ..., p_n) = \delta^4(P - \sum_{i=1}^{n} p_i) \prod_{i=1}^{n} \frac{d^3p_i}{(2\pi)^3 2E_i} \tag{1.37}$$

Solving for two-body decay (in c.m. coordinate), where a nucleus of mass m_i decays to daughter nucleus of mass m_1 by emitting a particle of mass m_2 with momentum p_1 and p_2, respectively, one gets

$$\phi_2 = \frac{1}{128\pi^5 m_i^2} \sqrt{[m_i^2 - (m_1 + m_2)^2][m_i^2 - (m_1 - m_2)^2]} \tag{1.38}$$

When the nucleus is excited (E_x) with $m_i^* = m_i + E_x$ and further it decays to daughter nucleus which is also excited (E_1), the phase-space is modified to

$$\phi_2 = \frac{1}{128\pi^4 m_i^*2} \sqrt{[m_i^*2 - ((m_1 + E_1) + m_2)^2][m_i^*2 - ((m_1 + E_1) - m_2)^2]} \tag{1.39}$$

For example, phase-space factors as function of E_x for various channels and phase-space factors as function of E_1 for p+^{11}B channel for E_x= 20 MeV are shown in Fig.1.9. The phase space factor for α-decay is much larger than other channels since the separation energy is much lower (see Tab. 1.1).

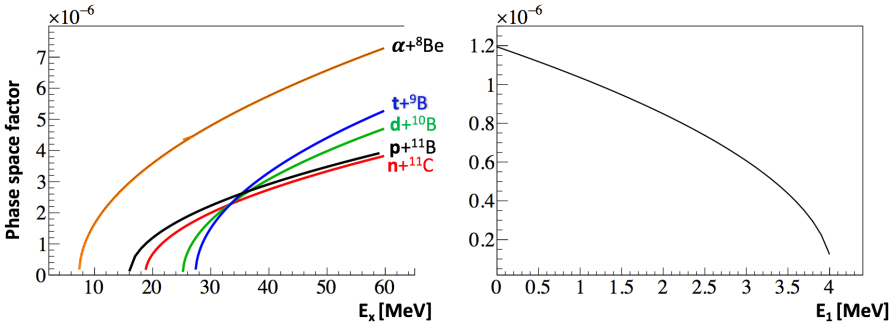

Figure 1.9: Phase-space factors as function of excitation energy of the parent nucleus (E_x) for various channel (left) and phase-space factor as function of excitation energy of daughter nucleus (E_1) for p+^{11}B channel at E_x= 20 MeV (right).

Decay Width

Once all the factors are calculated, the decay width for a given E_x and J^π information of the parent nucleus to all possible excited states of daughter nucleus can be calculated by E.q.1.29.

For example, consider ^{12}C nucleus which decays to ^{11}B by emitting a proton ($S_p = 15.9$ MeV), ^{11}C by emitting a neutron ($S_n = 18.7$ MeV) and other channels which open up with increase in excitation energy. At $E_x = 20$ MeV and $T = 1$, ^{12}C can only decay to 3 states; the ground state of ^{11}B, the ground state of ^{11}C and the first excited state of ^{11}B at E_1=2.12 MeV. Here alpha decay is neglected since it is forbidden for T=1 transition due to the isospin conservation. Calculated P($\Gamma_i/\sum\Gamma_i$) is summarized in Tab.1.3 for initial state with$J^\pi = 1^-$ and in Tab.1.4 for initial state with $J^\pi = 2^-$. The 2.12 MeV state decays to ground state to give 2.12-MeV γ-ray emission with a 100% emission probability [8]. Consequently, the γ-ray emission probability from the ^{12}C state at $E_x = 20$ MeV is calculated by Eq.(1.28) to be 0.256 for 1^- and 0.148 for 2^- (Tab.1.5).

It is clear that the γ-ray branching ratio depends upon J^π state of the parent nucleus.

Table 1.3: Calculation for ^{12}C (E_x =20 MeV) , $T = 1$, $J^\pi = 1^-$

Decay State	J^π	T (for allowed L)	Phase-space Factor (10^{-6})	Decay width(Γ_i) (Arbitrary units)	P ($\Gamma_i/\sum\Gamma_i$)
^{11}B(g.s.)	$3/2^-$	$T_0 + 2T_2 = 1.752$	11.94	10.46	0.474
^{11}B(2.12 MeV)	$1/2^-$	$T_0 + T_2$=1.359	8.27	5.61	0.256
^{11}C(g.s.)	$3/2^-$	$T_0 + 2T_2 = 1.742$	6.71	5.85	0.267

Table 1.4: Calculation for ^{12}C (E_x =20 MeV) , $T = 1$, $J^\pi = 2^-$.

Decay State	J^π	T (for allowed L)	Phase-space Factor (10^{-6})	Decay width(Γ_i) (Arbitrary units)	P ($\Gamma_i/\sum\Gamma_i$)
^{11}B(g.s.)	$3/2^-$	$T_0 + 2T_2 + T_4 = 1.753$	11.94	10.47	0.545
^{11}B(2.12 MeV)	$1/2^-$	$2T_2$=0.786	8.27	3.25	0.148
^{11}C(g.s.)	$3/2^-$	$T_0 + 2T_2 + T_4 = 1.744$	6.71	5.85	0.306

Table 1.5: γ-ray emission probability($\frac{\Gamma_\gamma}{\Gamma}$) from ^{12}C ($E_x$ =20 MeV, T =1) for different J^π states.

J^π	P($\Gamma_i/\sum\Gamma_i$) (from decay model)	Br(2.12→ g.s.) [8]	$\frac{\Gamma_\gamma}{\Gamma}$
1^-	0.256	1.00	0.256
2^-	0.148	1.00	0.148

1.2 Core-collapse supernova and neutrino emission

A massive star with a mass about 10 times larger than the solar mass($M_\odot$) evolves to an onion-like structure through the thermonuclear burning of nuclear fuels [15, 16]. The process begins with the fusion of hydrogen to helium and continues to terminate till the formation of iron, the nucleus with the maximum binding energy per nucleon. Thus, the massive star develops a central core primarily of iron group nuclei. Once the mass of the core exceeds the Chandrasekhar mass limit (1.4 $M_\odot$), it cannot support itself by the electron degeneracy pressure anymore, becomes unstable to the gravitational self-attractive force and eventually collapses gravitationally. The gravitational energy released from a core-collapse supernova explosion (ΔE) can be estimated roughly by

$$\Delta E = -\frac{GM_{core}^2}{R_{Fe}} - \frac{GM_{core}^2}{R_{NS}} \sim 1.5 \times 10^{53}\ erg, \tag{1.40}$$

where G is the gravitational constant, $M_{core} \sim 0.7M_\odot$ is the mass of the core and $R_{Fe} \sim 10^8$ cm and $R_{NS} \sim 10^6$ cm is the radius of the Fe core before the explosion and neutron star after the explosion The most of this energy (about 99%) is carried away by neutrinos, since they interact most weakly with matter. Therefore, the neutrinos plays a very important role in a core-collapse supernova.

1.2.1 Supernova neutrino

The emission mechanism of neutrinos from a supernova is schematically shown in Fig1.10 [17].

1. gravitational collapse
   Once the Fe core is formed and the temperature (T) reaches about 5×10^{10}K, Fe is decomposed into He and then to proton and neutron by photodissociation and electron capture as

$$^{56}Fe + \gamma \to 13^4He + 4n - 124.4[MeV], \tag{1.41}$$

$$^4He + \gamma \to 2p + 2n - 28.3[MeV], \tag{1.42}$$

$$p + e^- \to n + \nu_e. \tag{1.43}$$

   Consequently, the number of electrons decreases and electrons degenerate eventually and the core-collapses gravitationally. Since these reactions are endothermic, the collapse is accelerated and the core is contracted. At the early stage of core-collapse, the mean free path of neutrinos is larger than the core radius, therefore, neutrino emitted by Eq.(1.43) escapes from the core. The energy released by neutrino in this process is $\sim 10^{51}$ erg.

2. neutrino trapping
   Once the core density exceeds 3×10^{10}gcm^{-3}, the core becomes opaque to neutrino due to the coherent scattering with nuclei A as

$$\nu + A \to \nu + A. \tag{1.44}$$

   Therefore, neutrinos emitted by Eq.(1.43) are trapped and the corresponding surface is called a neutrino sphere.

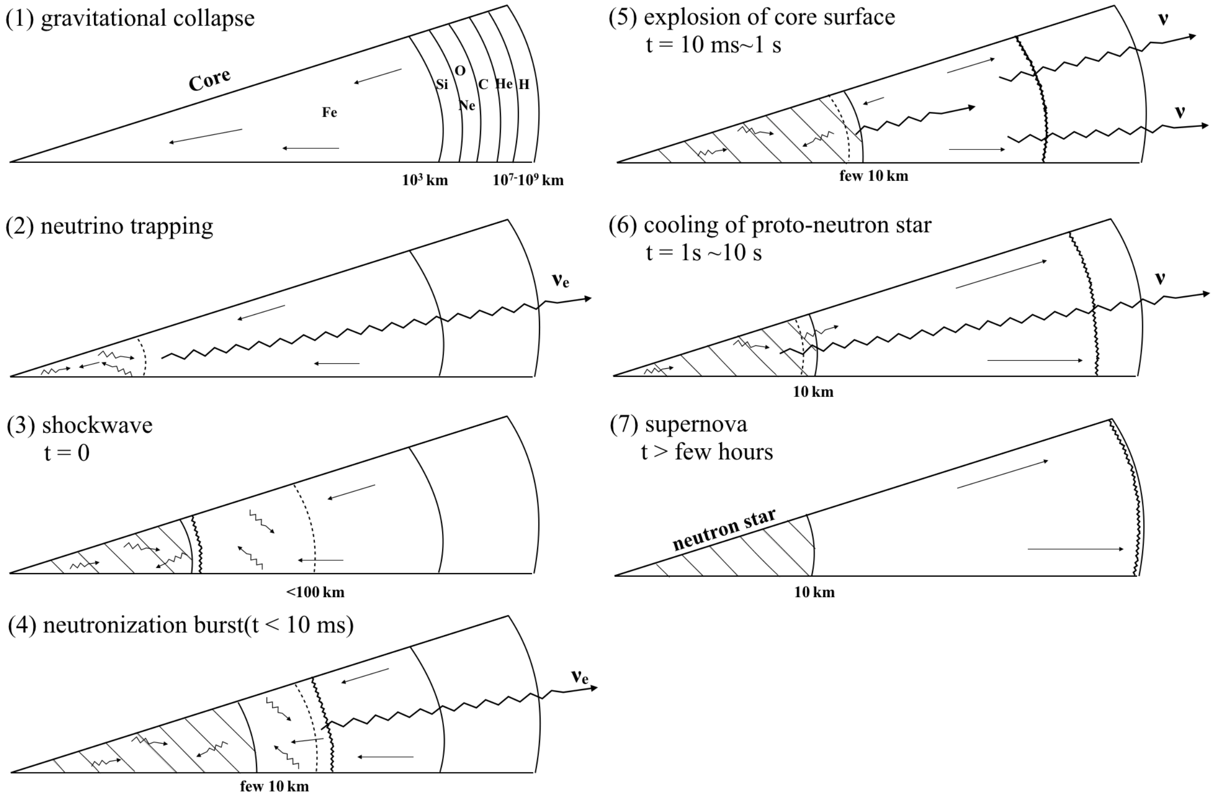

Figure 1.10: Emission mechanism of neutrinos from a supernova explosion process (1)-(7) [17]. Shaded area corresponds to hydrostatic equilibrium neutron star, dotted line to neutrino sphere, wavy line to shock wave. Full allow shows the matter transfer and wavy allow shows the neutrino transfer. t = 0 is the bounce time of inner core, when the shockwave is formed.

3. shockwave emergence(t=0)
   Once neutrinos are trapped, they also begin to degenerate, which equilibrates the electron capture reaction (Eq.(1.43)). This is called β equilibrium. Once the core density exceeds the nuclear density (3×10^{14}gcm^{-3}), there is no distinction between nuclei and free nucleons and they behave as a gas. Due to the repulsive effect of the nuclear force, the inner core starts to expand rapidly while the outer core still contracts. These two opposite phenomena create a shockwave which moves toward outside of the star. The central core is called a proto-neutron star because the lepton number per nucleon ($Y_L \sim 0.4$) is higher than that of a typical neutron star ($Y_L \sim 0.05$).

4. neutronization burst (t$\leq$10msec)
   Once the shockwave passes through the neutrino sphere, nuclei are decomposed into free nucleons and a huge number of electron neutrinos are emitted again by electron capture (Eq.(1.43)) within very short time ($\sim$10 ms). Although the luminosity is as high as $\sim 10^{53}$ $erg\ s^{-1}$, the time scale is so short that the total energy emitted is $\sim 10^{51}$ erg. This neutrino emission process is called neutronization burst. Neutrinos emitted until this stage are all electron neutrinos (ν_e).

5. core explosion (t=10msec-1sec)
   After the burst, matter consists of high temperature nucleons and electron-positron pairs. ν_e and $\bar{\nu}_e$ are created by electron capture (Eq.(1.43)) and positron capture (Eq.(1.45)), respectively.

   $$e^+ + n \rightarrow \bar{\nu}_e + p. \tag{1.45}$$

   In addition, all types of neutrinos (ν_e, ν_e, ν_e and their anti-particles) are created by electron-positron pair annihilation as

   $$e^- + e^+ \rightarrow \nu + \bar{\nu}. \tag{1.46}$$

   Therefore the matter gradually falls into the inner core by changing its gravitational energy into thermal energy, which is carried away by neutrinos during a time scale of 100 ms - 1s.

6. proto-neutron star cooling (t=1sec-10sec)
   A proto-neutron star is formed by the inner core and the falling matter. Within the proto-neutron star, neutrinos are in equilibrium with matter and diffused gradually (~10s). These neutrinos carry away the thermal energy (several 10^{53}erg) and the lepton number of the proto-neutron star and it cools down to become a neutron star.

7. supernova (t>several hours)
   Once the shockwave propagates to the core surface, it blows off the outer layer. Since the temperature and the density at the outer layer are low, the shockwave propagates without loss. Several hours after the core bounce, the shockwave reaches the stellar surface and the star starts to shine.

Energy of supernova neutrino

The energies (E) of the neutrinos and anti-neutrinos show the ordering of $\langle E_{\nu_x}\rangle > \langle E_{\overline{\nu}_e}\rangle > \langle E_{\nu_e}\rangle$ where ν_x denotes the ν_τ (ν_μ) neutrinos and their anti-particles. As an example, neutrinos spectra from a core-collapse supernova calculated by the authors of [18] are shown in Fig.1.11. The energy hierarchy comes from the fact that the material is neutron rich, therefore, the interactions with ν_e are more likely to occur than with $\overline{\nu}_e$, and consequently, the neutrino sphere of $\bar{\nu}_e$ is located deeper (and then hotter) than that of ν_e. The neutrino sphere of ν_x is located, relatively, much deeper since ν_x can only have neutral current (NC) interactions with the matter in the core, whereas the ν_e and $\bar{\nu}_e$ have both charged current (CC) and NC interactions with the matter.

1.2.2 Detection of core-collapse supernova neutrinos

SN1987A

On 24th February 1987, a supernova, SN1987A, was discovered by the optical telescope in the Large Magellanic Cloud, which is 50 kpc away from the earth [19]. SN1987A was identified as a Type II supernova (regarded as a core-collapse driven supernova) since hydrogen lines were seen in the optical spectrum. The neutrino burst from SN1987A was actually observed by water-Cherenkov detectors by KAMIOKANDE II (11 events) and IMB (8 events) [20, 21].

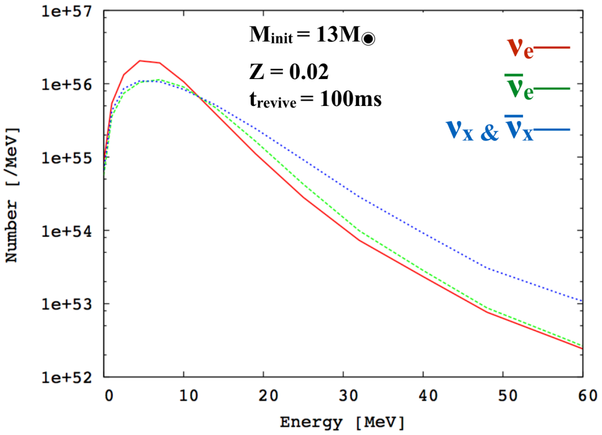

Figure 1.11: Neutrinos energy spectra from a core-collapse supernova with initial mass (M) of 13 solar mass (M∘), metallicity (Z) of 0.02 and shock revival time of 100 msec [18].

Expected number of events by existing large scale neutrino detectors

Although SN1987A was the only supernova in which neutrinos have been observed, many large scale neutrino detectors are running in order to detect the supernova neutrinos. For example, the expected numbers of neutrino events from a core-collapse supernova at 10 kpc distance are summarized in Table.1.6 for Super Kamiokande (22.5 kton water-Cherenkov detector) [22] and in Table1.7 for KamLAND (1 kton liquid scintillator detector) [23].

Table 1.6: Expected numbers of events in Super Kamiokande for a supernova at 10 kpc [22].

Reaction	No. of events
$\bar{\nu}_e + p \to e^+ + n$	8830
$\nu_x + {}^{16}\mathrm{O} \to \nu_\mathrm{x} + \gamma + \mathrm{X}$	710
$\nu_e(\bar{\nu}_e) + e^- \to \nu_e(\bar{\nu}_e) + e^-$	200
$\nu_x + e^- \to \nu_x + e^-$	120

Table 1.7: Expected numbers of events in KamLAND for a supernova at 10 kpc [23]. For $\nu_x +^{12} C$, only the excitation to the $E_x = 15.11$ MeV state was taken into account.

Reaction	No. of events
$\bar{\nu}_e + p \to e^+ + n$	330
$\nu_x + {}^{12}\mathrm{C} \to \nu_\mathrm{x} + \gamma_{15.1} + {}^{12}\mathrm{C}$	58
$\nu_x + e^- \to \nu_x(\bar{\nu}_e) + e^-$	16
$\bar{\nu}_e + {}^{12}\mathrm{C} \to \mathrm{e}^+ + {}^{12}\mathrm{B}$	7
$\nu_e + {}^{12}\mathrm{C} \to \mathrm{e}^- + {}^{12}\mathrm{N}$	2

The main signal is induced by CC inverse β decay reaction with proton, which can only detect $\bar{\nu}_e$. Notable number of signals come from the NC inelastic scattering of neutrinos (anti-neutrinos) with ^{16}O and ^{12}C in addition to NC elastic scattering with electrons. For $\nu_x +^{12} C$, only the excitation to the $E_x = 15.11$ MeV state has been taken into account and γ rays from giant resonances had been ignored until now. NC inelastic scattering events are dominated by ν_x because of their higher energies as shown in Fig.1.11. Therefore, the detection of NC inelastic scattering events is important for understanding of the underlying mechanism of supernova explosion.

Neutral current inelastic scattering events

By ν_x-^{16}O and ν_x-^{12}C inelastic reactions, nuclei can be excited to giant resonances. The theoretical calculations of NC reactions, in the energy range of supernova neutrinos ($E_\nu < 100$ MeV), predict the dominant excitations to spin-dipole resonances (SDR) with spin-parities (J^p) of 1^- and 2^- [24, 25, 26, 27]. For example, the differential cross sections for $^{16}\mathrm{O}(\nu, \nu')$ predicted by authors of Ref.[24] at an average neutrino energy of 31.5 MeV for different multipolarities are shown in Fig.1.12. Giant resonances dominated by J^π of 1^- and 2^- excitations are seen in the excitation energy range between 15 and 30 MeV.

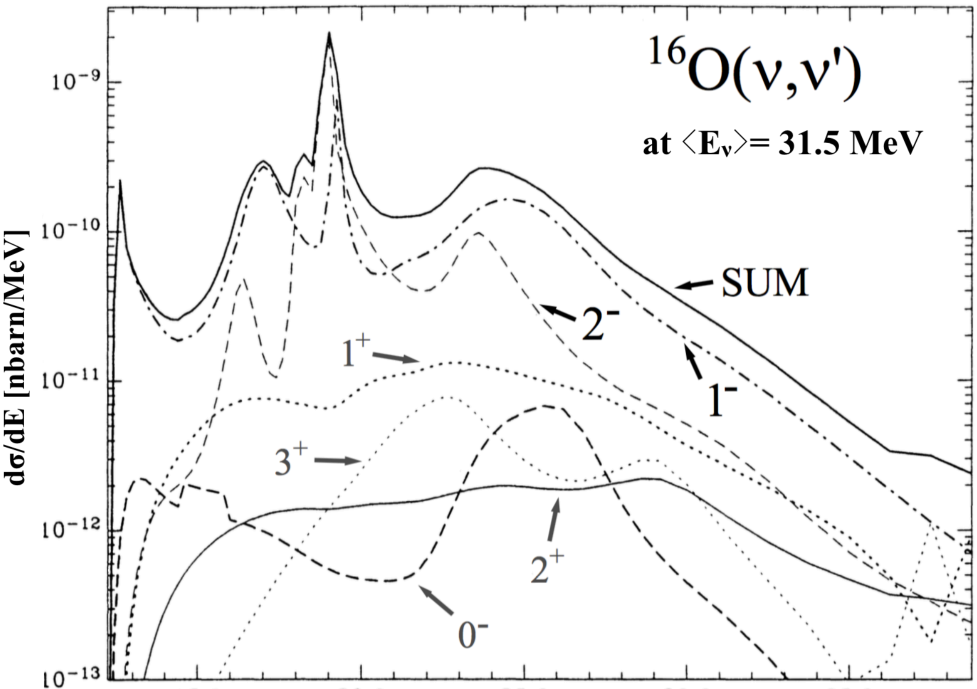

Figure 1.12: Predicted differential cross sections for $^{16}\mathrm{O}(\nu, \nu')$ for different multipolarities [24].

The γ rays can be emitted from giant resonances as mentioned in Sec.1.1.3. Since the energies of the γ rays (5-10 MeV for ^{16}O and 2-11 MeV for ^{12}C) are higher than the detector threshold (5 MeV for Super Kamiokande and 0.2 MeV for KamLAND), NC inelastic events can be identified by measuring these γ rays. In addition to SDR, the $J^\pi = 1^+$ state at E_x =15.11 MeV can also contribute for ^{12}C, which emits a 15.11-MeV γ ray [28].

1.3 Purpose of this work

NC event induced by ν_x emitted from a core-collapse supernova are expected to be identified by measuring the γ rays emitted from the giant resonances of ^{12}C and ^{16}O. But the γ-ray emission process has not been measured systematically (relative intensity has been measured for ^{16}O using bremsstrahlung γ rays [29]). Therefore, an experiment to measure γ rays from giant resonances of ^{12}C and ^{16}O was carried away using a high resolution magnetic spectrometer "Grand Raiden" and a γ-ray detector (NaI(Tl) scintillation counters) at Research Center for Nuclear Physics (RCNP). The purposes of the experiment are summarized as follows.

1. Tagging the giant resonances by (p,p') inelastic scattering and measurement of the γ rays from them.
2. Measurement of the energy and emission probability of the γ rays.
3. Study of the γ-ray emission mechanism.
4. Verification of the decay model.
5. Estimation of number of NC events from a core-collapse supernova.

In Chap.2, the experimental setup and conditions are summarized. In Chap.3, the analysis procedure and calibration of the spectrometer and the γ-ray detector are described. In Chap.4, experimental results are summarized. In Chap.5, the γ-ray emission process is discussed and experimental results are compared to theoretical predictions. In Chap.6, The present experimental results are used to estimate the number of NC events from a core-collapse supernova. Summary and conclusion of this work are given in Chap.7.

Chapter 2

Experiment

An experiment to measure the γ rays emitted from giant resonances of ^{12}C and ^{16}O was carried out at Research Center for Nuclear Physics (RCNP), Osaka University, under the project number E398. An overview of the RCNP facility is illustrated in Fig.2.1. A 392 MeV unpolarized proton beam bombarded targets. Scattered protons at scattering angle (θ) of 0° were momentum analyzed by the magnetic spectrometer "Grand Raiden" [31]. In coincidence with scattered protons, γ rays were measured by 25 NaI(Tl) scintillation counters. In this Chapter, experimental setup and conditions are described.

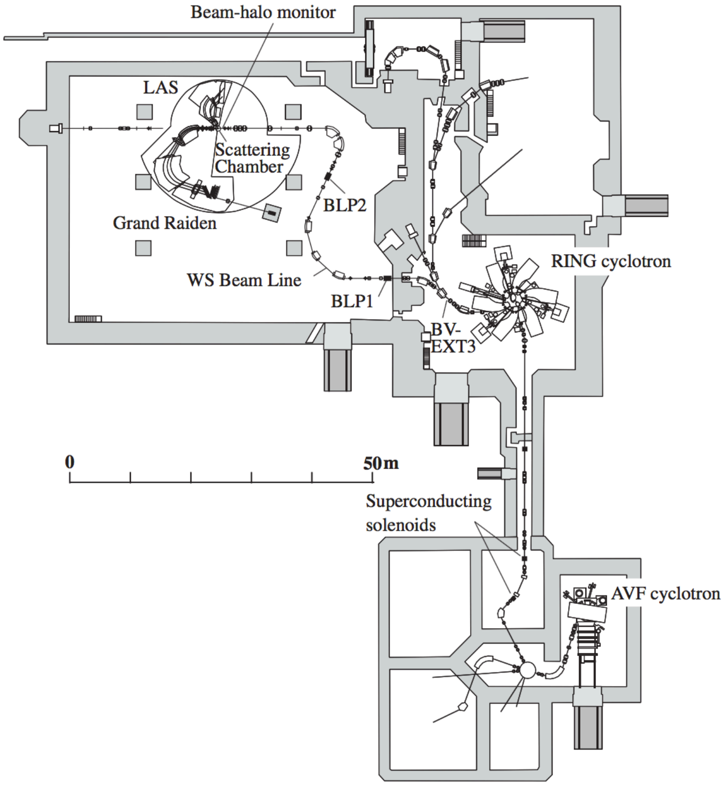

Figure 2.1: RCNP facility [31].

2.1 Beam line

An unpolarized proton beam was produced by an Electron Cyclotron Resonance ion source, NEOMAFIOS [32]. The proton beam was injected to an Azimuthally Varying Field (AVF) cyclotron and was accelerated up to 65 MeV. The 65-MeV proton beam was further injected to a Ring cyclotron and was accelerated up to 392 MeV. Finally, the 392-MeV proton beam was achromatically transported by WS beam line and bombarded targets. The beam current was monitored by a Faraday cup located at the beam dump. The typical beam intensity was 0.5 - 1.5 nA. The intensity was limited by the counting rate of the γ-ray detector in order to avoid the piling-up effect and the scattered charged particle effects. The energy resolution of 80 - 200 keV (FWHM) was achieved. Since the γ-ray detector was placed as close as 10 cm from the target position, the background γ rays and charged particles created by the primary beam had to be taken into account. In order to minimize these backgrounds, the beam was finely tuned (halo-free mode beam).

Charge correction and beam transmission

The primary beam was injected to Faraday cups (FC) and the charge, namely the number of protons, was recorded throughout the experiment. Q1 Faraday cup installed at the Q1 magnet in Fig.2.4 (Q1FC) was used for the calibration run at $\theta = 2.5°$. 0° Faraday cup installed at the beam dump in Fig.2.4 and Fig.2.5 (0°FC) was used for the main measurement at $\theta = 0°$. The beam transmission at Q1 Faraday cup was 100 %, since it was located very close to the main target. On the other hand, the 0° Faraday cup was located about 30-m downstream of the target and the transmission could be decreased depending on the magnet setting.

The beam transmission was monitored by the Beam Line Polarimeter (BLP) indicated as BLP1 in Fig.2.1 in the calibration runs. The BLP consisted of two pairs of two plastic scintillator counters (L-L' and R-R') as shown in Fig.2.2.

A thin aramid BLP target with thickness of 4 microns was periodically installed into the beam line. Each pair counted scattered proton and recoiled proton in coincidence. By comparing the BLP counts and the charge recorded by the two FC's, the beam transmission was relatively estimated. The result is summarized in Tab.2.1, where BLP counts indicate the sum of L-L' counts and R-R' counts. The beam transmission at the 0° Faraday cup was 100 % within the statistical error of 3 %.

Table 2.1: The beam transmission measurement result.

Faraday cup	Charge (Q) [nC]	BLP counts	BLP/Q
Q1	485	1869	3.85±0.09
0°	525	2083	3.97±0.09

2.2 Targets & scattering chamber

A natural carbon target and a cellulose ($C_6H_{10}O_5$) target with thickness of 36.3 mg/cm^2 and 28.2 mg/cm^2, respectively, were mounted to a target frame (left pane in Fig.2.3). The purity was higher than 99.9 % for both targets. The natural abundance of ^{12}C and ^{16}O are 98.93% and 99.757%, respectively [30]. The ^{16}O data were estimated by subtracting the carbon data

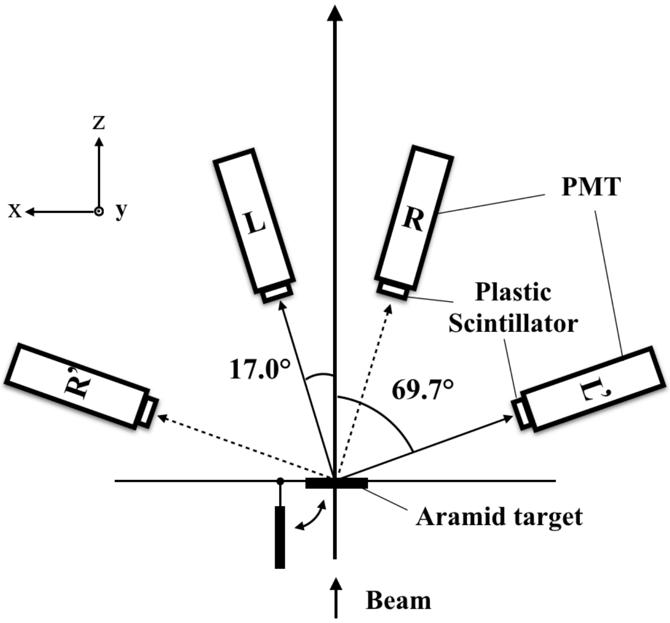

Figure 2.2: The schematic view of the Beam Line Polarimeter (top view).

from the cellulose data. The target frame was mounted to the electric target ladder system, which was fixed on the scattering chamber (right panel in Fig.2.3). In order to minimize the absorption of the γ rays, a relatively small scattering chamber was used. The design drawings can be found in Appendix B.

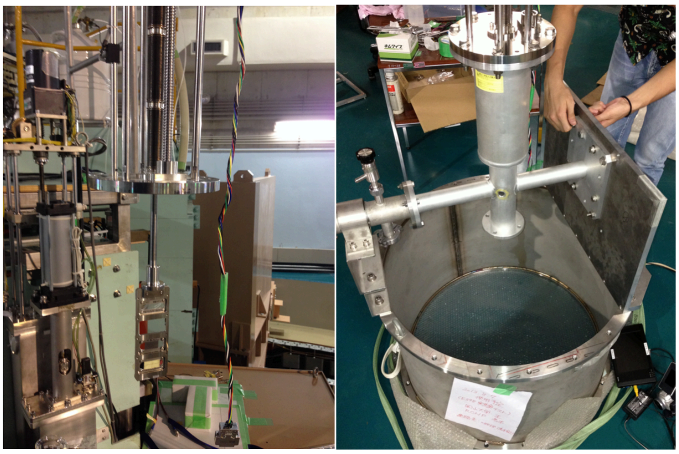

Figure 2.3: Target ladder system (left) and scattering chamber (right).

2.3 Magnetic spectrometer ”Grand Raiden”

An overview of the high energy resolution spectrometer Grand Raiden (GR) at 0° mode is illustrated in Fig.2.4. The specification of GR is summarized in Tab.2.2. GR was placed at $\theta = 0°$, which covers the scattering angle range of 0° - 3.5°. The magnetic configuration of GR has QSQDMDD type, where D, Q, S, and M stand for the dipole, quadrupole, sextupole and multipole, respectively. This configuration provides a high momentum (p) resolution of $p/\Delta p = 37000$. GR was designed to minimize almost all aberration terms in a third order matrix calculation. The primary beam was transported inside the GR to the beam dump located 12 m downstream of focal plane detectors. Inside the beam dump, the primary beam current was monitored by 0°FC. The beam dump was shielded by iron and concrete to reduce the backgrounds for the focal plane detectors and the γ-ray detector.

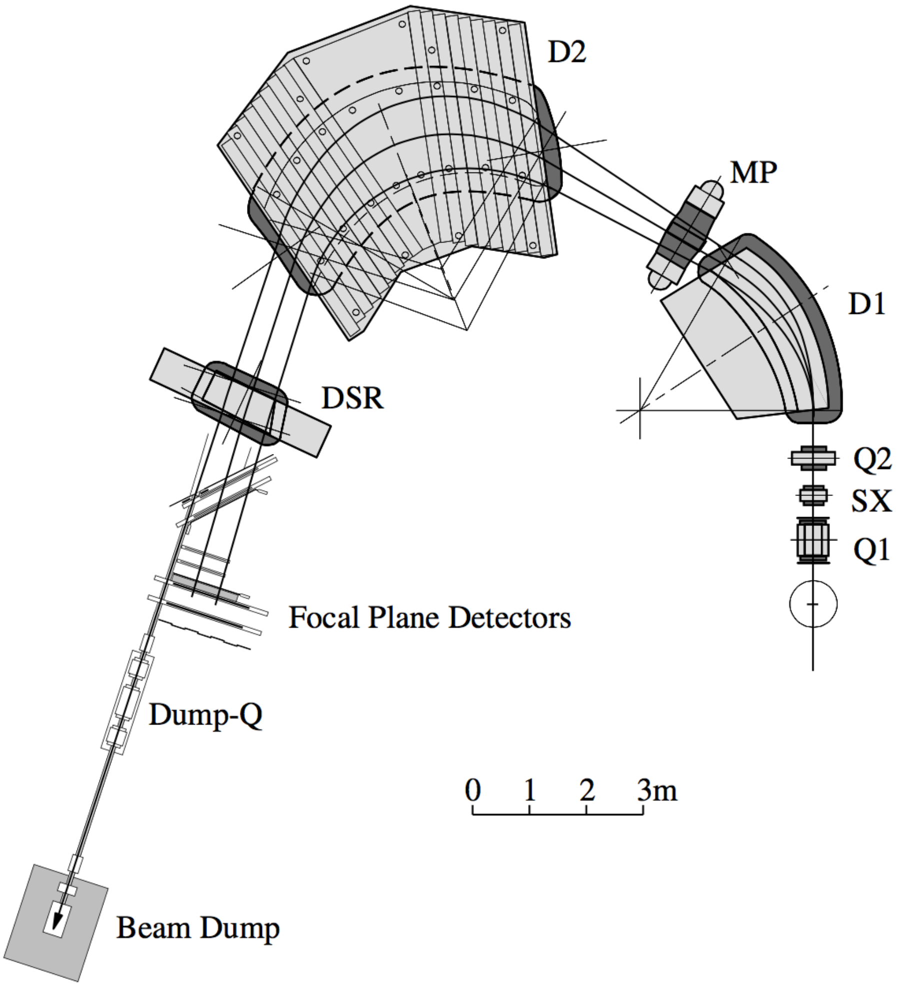

Figure 2.4: Magnetic spectrometer ”Grand Raiden” [31].

Table 2.2: Specification of GR

Magnetic configuration	QSDMDD
Mear orbit radius	3m
Total deflection angle	162°
Focal plane tilting angle	45°
Maximum particle rigidity	5.4Tm
Vertical magnification (y|y)	5.98
Horizontal magnification (x|x)	-0.417
Momentum range	5%
Momentum resolution (p/ Δ p)	37076
Scattering angle setting	0°
Acceptance of horizontal angle	± 20mr
Acceptance of vertical angle	± 70mr

2.3.1 Focal plane detector system

The focal plane detector system consisted of two multi-wire drift chambers (MWDC1 and MWDC2) and two plastic scintillators (PS1 and PS2) as shown in Fig.2.5. The primary beam was guided to the beam dump through the pipe located at higher momentum side of focal pane detectors, while the scattered protons with less momentum passed through the focal plane detectors. The MWDC's were used to track the scattered charged particles and then to calculate the momentum and scattering angles at the target point. The PS's were used for creating the fast trigger signal for data acquisition system and particle identification.

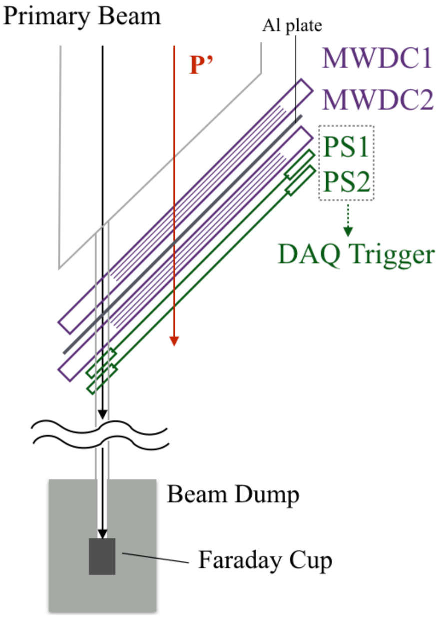

Figure 2.5: Focal plane detectors of Grand Raiden.

The wire configuration and the structure of MWDC are illustrated in Fig。2.6 (up). The specification of the MWDC is summarized in Tab.2.3. Each MWDC consisted of two wire planes, X and U. X planes were perpendicular to the spectrometer, whereas U planes were tilted by 48.2° in order to have the wire spacing of 6 mm in the horizontal direction.

The structure of the MWDC is illustrated in Fig.2.6 (down). A charged particle passing through the gas creates a ionization track. The gas of the counter consisted of Argon (70%), Iso-butane (30%) and Iso-propyl-alcohol (vapor pressure at 2 ℃). High voltage of -5.9 kV was applied to the cathode and a electric field was created. The electrons are drifted through this field to the anode wires. High voltage of -0.4kV (X) and -0.5kV (U) was applied to the potential wires in order to minimize the dependence of drift velocity on position. Using the drift time information, the track was reconstructed more precisely than the wire spacing. The anode wire signal was pre-amplified and discriminated by LeCroy 2735DC board. The timing information of the wires which had hits was digitized by LeCroy 3377 time to digital converter (TDC). Two plastic scintillators (PS1 and PS2) were placed downstream of MWDC. Each of them was coupled with 2 photo multiplier tubes (PMT) from both sides (L and R). The pulse height and the timing information were digitized by analog to digital converter (ADC) and TDC, respectively.

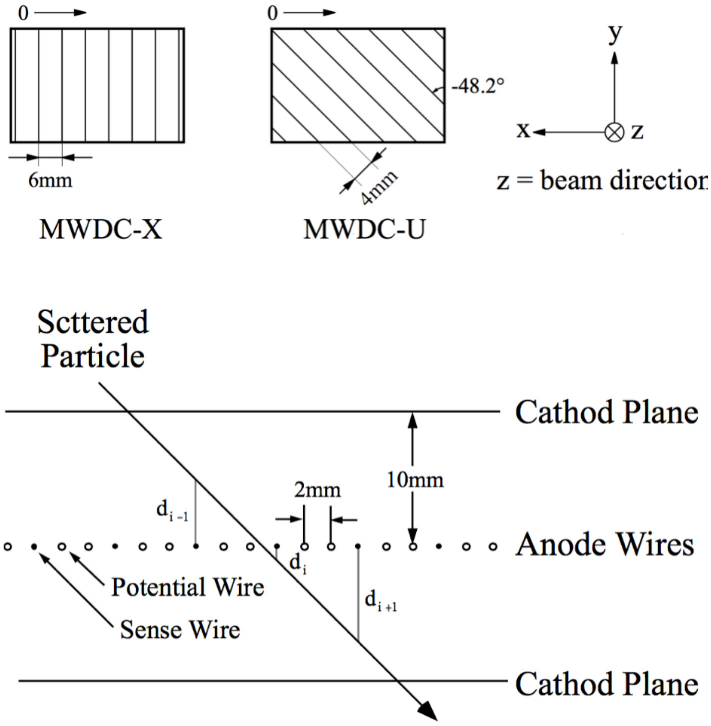

Figure 2.6: Wire configuration (up) and structure (down) of MWDC [31].

2.3.2 Off focus mode

The vertical focusing quadrupole magnet of GR was located close to the target in order to realize a large vertical acceptance. Therefore, the vertical magnification becomes small and makes the vertical angle resolution worse than 1°. To achieve better angular resolution in the

Table 2.3: Specification of MWDC.

Wire configuration	X (0°), U (48.2°)
Active area	1150mm (W) × 120mm (H)
Number of sense wires	192 (X) ,208 (U)
Cathode-anode gap	10mm
Anode wire spacing	2mm
Sense wire spacing	6mm (X), 4mm (U)
Sense wires	20μm ϕ gold-plated tungsten wire
Potential wires	50μm ϕ gold-plated beryllium copper wire
Cathode	10μm-thick carbon aramid film%
Cathode voltage	-5.9kV
Potential voltage	-0.4kV (X), -0.5kV (U)
Gas mixture	Argon (70%) + Iso-butane (30%) + Iso-propyl-alcohol (vapor pressure at 2 ℃)
Pre-amplifier	LeCroy 2735DC
TDC	LeCroy 3377

vertical direction, special ion optics mode called ”off focus mode ” was used [33]. In Fig.2.7(a), vertical trajectories of particles in the standard focus mode is illustrated. In this mode, the particles are focused at the focal plane. In the off focus mode (Fig.2.7(b and c)), the particles are focused upstream (over focus mode) or downstream (under focus mode) of the focal plane and then the vertical angle at the focus plane becomes larger, which enables better angular resolution at the target point. The under focus mode was used by changing the Q1 magnet by -7% compared to that of standard focus mode without sacrificing the solid angle.

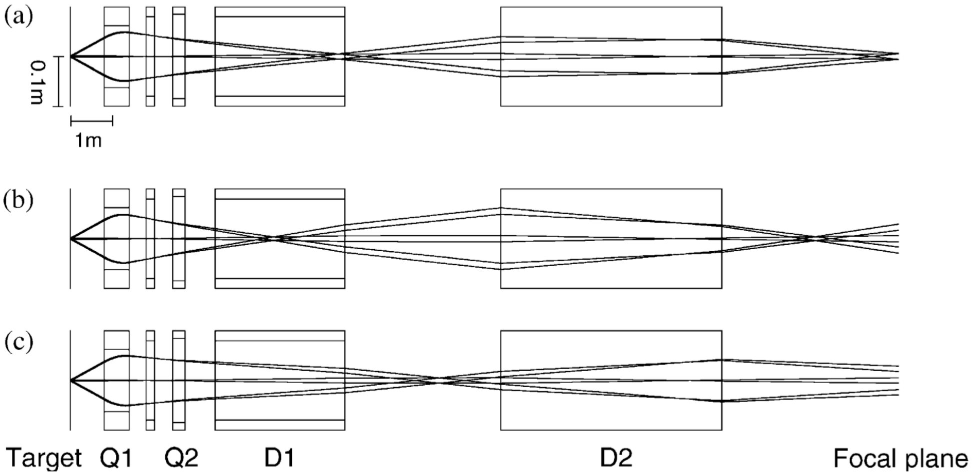

Figure 2.7: The vertical trajectories of scattered particle in the standard mode (a), the over focus mode (b) and the under focus mode (c) [33].

2.4 γ-ray detector

The γ-ray detector was designed using GEANT4 Monte Carlo Simulation [34, 35]. An array of γ-ray detector consisted of $5 \times 5 = 25$ NaI(Tl) scintillation counters (2 ” × 2 ” × 6 ”) coupled with PMTs was placed 10-cm away from the target point at $\theta_\gamma = 90°$ (Fig.2.8). The pulse height and the time information from each PMT were recorded by ADC and TDC, respectively.

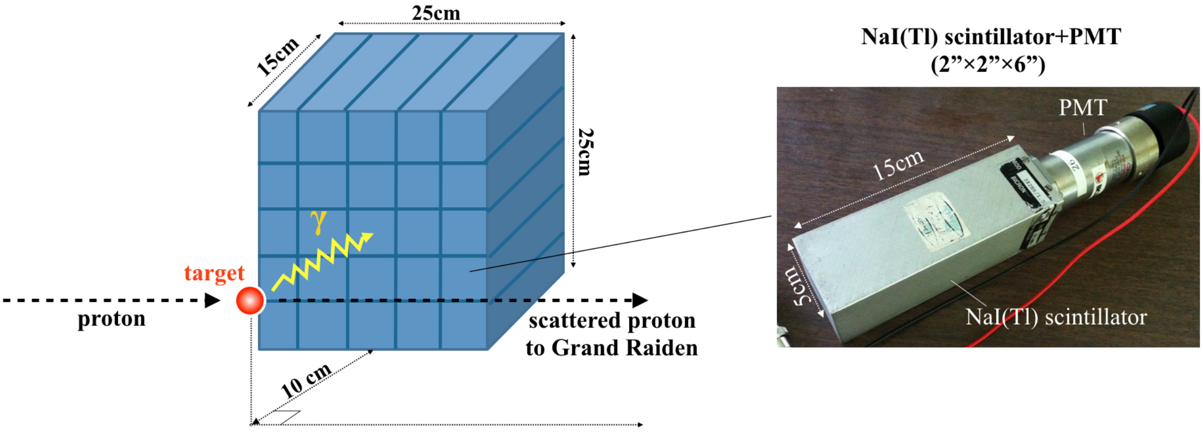

Figure 2.8: An array of γ-ray detector (left) and a NaI(Tl) scintillation counter (right).

2.4.1 Basic detector performance

A tabletop experiment with a simple ADC circuit was carried out in order to check the detector response of a NaI scintillation counter to γ rays. γ rays in the energy range of 0.7 - 9MeV from several radioactive sources listed in Tab.2.4 are used. For $^{252}\mathrm{Cf} + \mathrm{Ni}$ data, a $^{252}\mathrm{Cf}$ neutron source was put into a water tank to thermalize the neutron, then the neutron was captured by Ni followed by γ-rays emission.

Table 2.4: Radioactive sources used for the detector performance check.

Sources	E_γ [MeV]	Radioactivity [Bq]
$^{137}\mathrm{Cs}$	0.67	1.64×10^5
$^{60}\mathrm{Co}$	1.17 and 1.33	3.13×10^4
$^{241}\mathrm{Am} + \mathrm{Be}$	4.43	–
$^{252}\mathrm{Cf} + \mathrm{Ni}$	8.54 and 8.99	–

Typical energy spectra from these sources are shown in Fig.2.9. The γ-ray energy was calibrated from ADC information by a linear function as shown in the top panel of Fig.2.10. The 2.5-MeV sum peak of two γ rays from $^{60}\mathrm{Co}$ was also used in the calibration. The energy resolutions (ΔE_γ) estimated by the gaussian fits to the peaks are shown in black points in the bottom panel of Fig.2.10. The resolution arises from the statistical fluctuation of scintillation

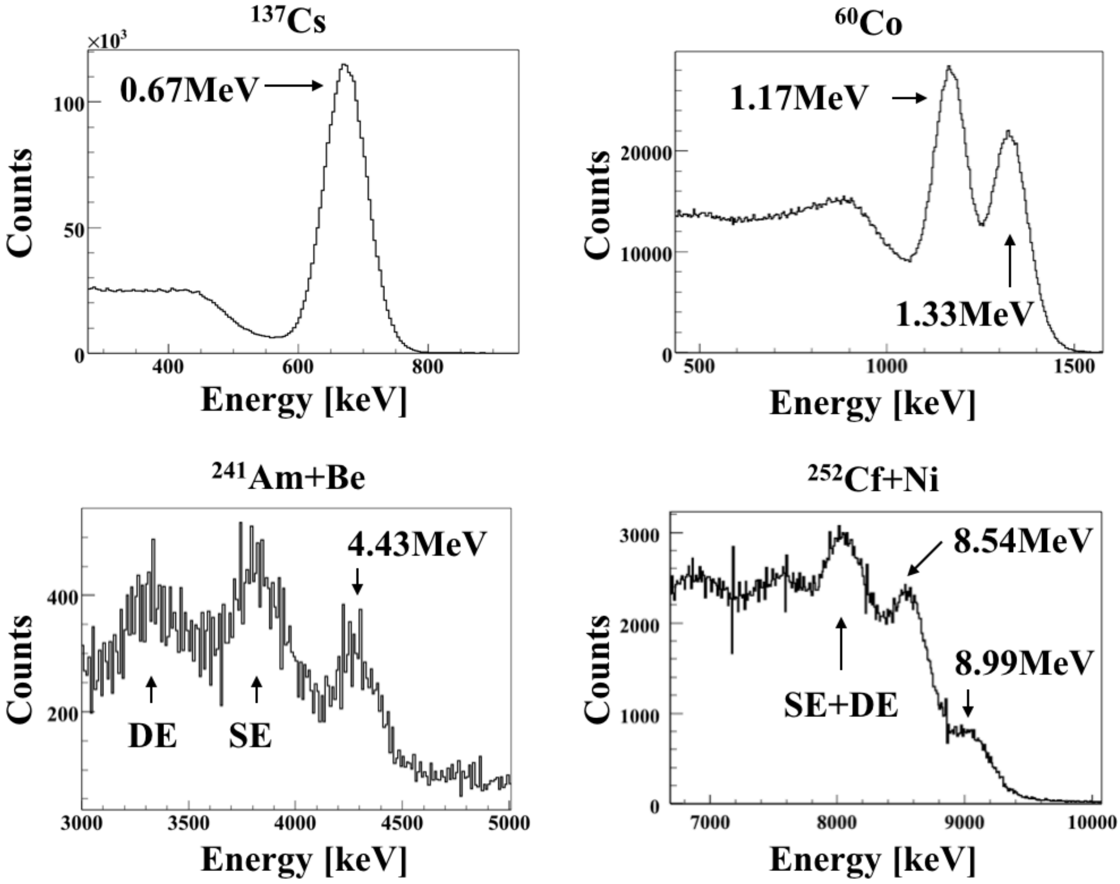

Figure 2.9: The energy spectra taken by radioactive sources. SE (DE) denotes single (double) escape peak.

light number (N_{scinti}), which is proportional to the γ-ray energy as

$$\frac{\Delta E_\gamma}{E_\gamma} \propto \frac{1}{\sqrt{N_{scinti}}} \propto \frac{1}{\sqrt{E_\gamma}}. \tag{2.1}$$

Therefore, the dependence of resolution on energy can be well fitted by Eq.(2.2) as shown in black line in Fig.2.10.

$$\Delta E = 1.1 \times \sqrt{E_\gamma(keV)} \ \ [keV]. \tag{2.2}$$

Comparison with detector simulation

In Fig.2.11, the data of ^{137}Cs and ^{60}Co (black) taken by 2 NaI counters are compared with the Monte Carlo (MC) simulation using Geant4 code (red) [36]. The distance from the source to the counter was 11.5 cm for NaI1 and 12.5 cm for NaI2. The MC were normalized by the γ-ray emission counts of the data calculated by the radioactivity and the measuring time. The MC reproduces both the shape of the spectrum and the detection efficiency quite well (Data/MC= 0.98 - 1.03).

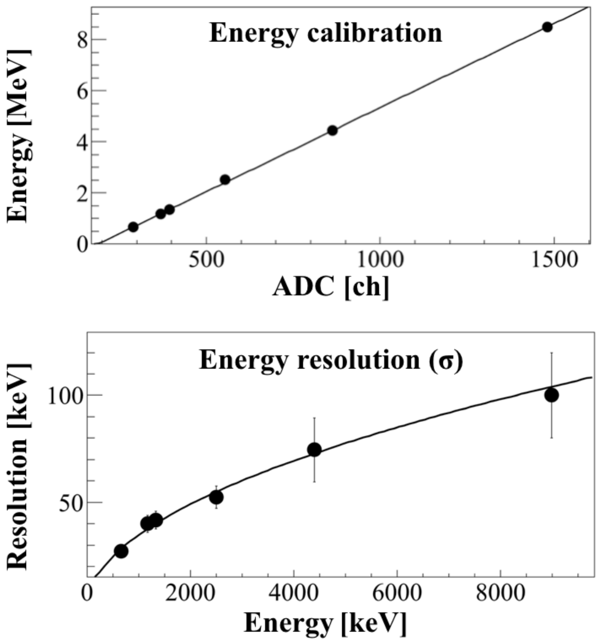

Figure 2.10: Energy calibration and energy resolution of a NaI counter.

2.5 Trigger and data acquisition system

The data acquisition system (DAQ) was divided in to two systems, GR-DAQ and γ-DAQ. The read-out diagram of the plastic scintillators (PS) at focal plane is shown in Fig.2.12. The charge from each side (Left and Right) of a PS was divided into two signals. One of them was sent to a fast encoding and reading ADC (FERA) for pulse height information. The other was discriminated by a constant fraction discriminator (CFD) and sent to a fast encoding and reading TDC (FERET) for time-of-flight information. The CFD outputs from both left and right sides were also sent to a mean timer module to generate a coincidence signal for each PS. The coincidence signals of 2 PS's were sent to a LeCroy 2346 Universal Logic Module of the field programmable gate-array (FPGA) chip. A PS trigger signal was generated by taking the coincidence of two plastic scintillators and was used for GR-DAQ trigger, PS-TDC start, PS-ADC Gate, MWDC-TDC start and NaI coincidence gate. The details of the DAQ system of Grand Raiden are described in Ref.[37].

The read-out diagram of the γ-ray detector is shown in Fig.2.13. The same ADC and TDC read-out modules as those of PS were used. The CFD outputs from 25 NaI counters were sent to a coincidence module and an OR signal was generated if at least one of the NaI counters had a hit. The OR signal was sent to another coincidence module together with the PS trigger signal. A NaI-Trigger signal was generated by taking the coincidence of the PS trigger signal and the NaI-OR signal, and was used for γ-DAQ Trigger, γ-ADC Gate and γ-TDC Start. The timing chart of PS trigger and NaI Trigger is shown in Fig.2.14.

Additionally, 2 plastic scintillators were placed in front of NaI detector and ADC and TDC information were recorded. 5 CsI scintillators were placed in backside of NaI detector and only ADC information were recorded. Although these counters were placed in order to reject the background, not analyzed in the present study.

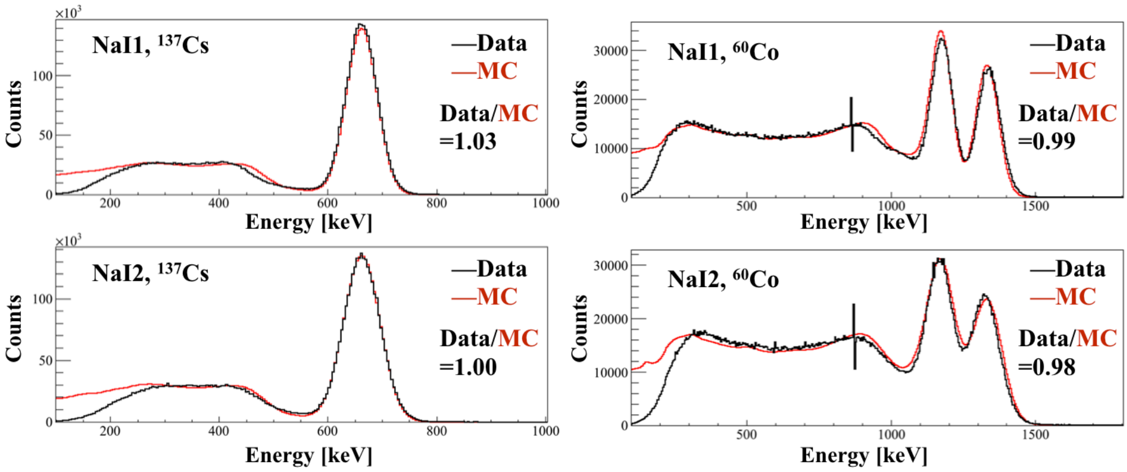

Figure 2.11: The energy spectra of data (black) and MC (red). Data/MC shown in the figures is the number of events from the data divided by that from MC with energy higher than 0.3 MeV for ^{137}Cs and 0.5 MeV for ^{60}Co.

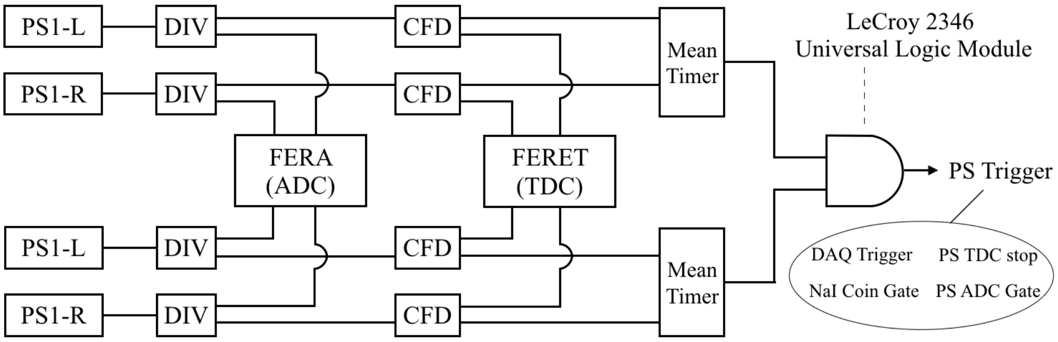

Figure 2.12: Trigger and read out diagram of the plastic scintillators.

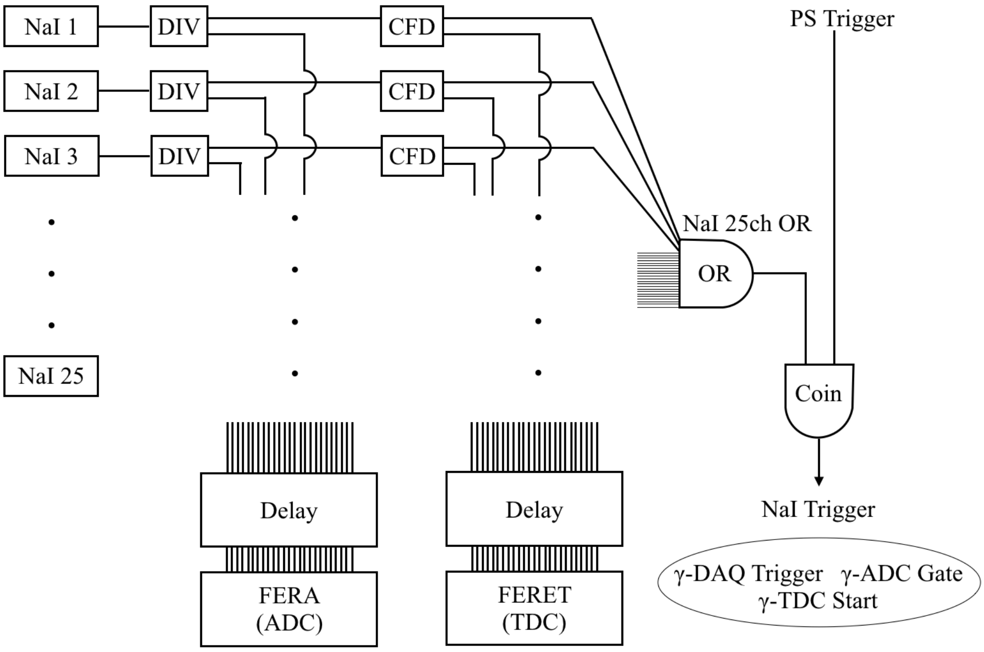

Figure 2.13: Read-out diagram of PS Trigger and NaI Trigger.

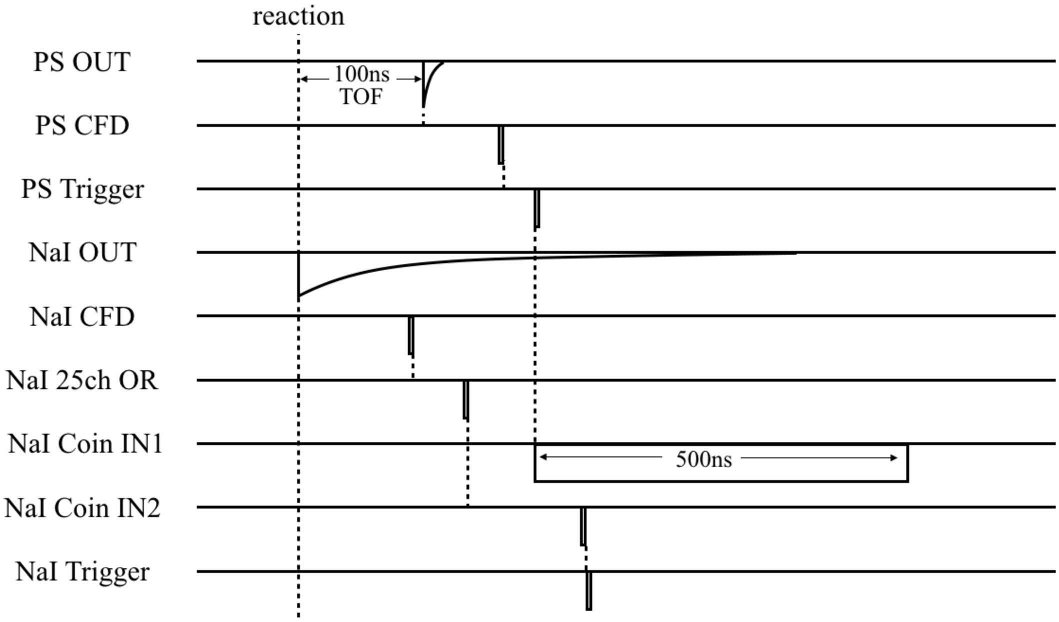

Figure 2.14: Timing chart of signals.

Chapter 3

Data Analysis

The experimental data were stored in the RCNP server and have been analyzed by Tamii analyzer code. Data sets are summarized in Tab.3.1.

Table 3.1: Experimental data sets.

Target	Beam intesity [nA]	Beam charge [nC]
^{12}C	0.5	61282
	1.0	43228
	1.5	22103
$C_6H_{10}O_5$	0.5	48531
	1.0	30115

3.1 Analysis of Magnetic Spectrometer "Grand Raiden"

Grand Raiden (GR) consists of two types of detectors, plastic scintillators (PS) and multi-wire drift chambers (MWDC). The particle identification (PID) has been carried out by PS analysis. The excitation energy of the target (E_x) and the scattering angle (θ) of the protons were measured by MWDC. The analysis procedure for each detector is described in this Section.

The definition of the coordinate system at the target position is shown in Fig.3.1. The Z axis is taken to the beam direction from upstream to downstream. X and Y axes are taken to the horizontal and vertical planes, respectively. The horizontal scattering angle (θ_t) and the vertical scattering angle (ϕ_t) of scattered protons are defined. θ_t and ϕ_t are related to polar angle (θ) and azimuthal angle (ϕ) used in a usual polar coordinate system by,

$$\begin{aligned} \tan\theta_t &= -\tan\theta\cos\phi, \\ \tan\phi_t &= \tan\theta\sin\phi. \end{aligned} \tag{3.1}$$

The total scattering angle θ is defined as, $\tan\theta = \sqrt{\tan\theta_t^2 + \tan\phi_t^2}$. For small angles, $\theta \sim \sqrt{\theta_t^2 + \phi_t^2}$.

The definition of the coordinate system at the focal plane is taken similarly and shown in Fig.3.2.

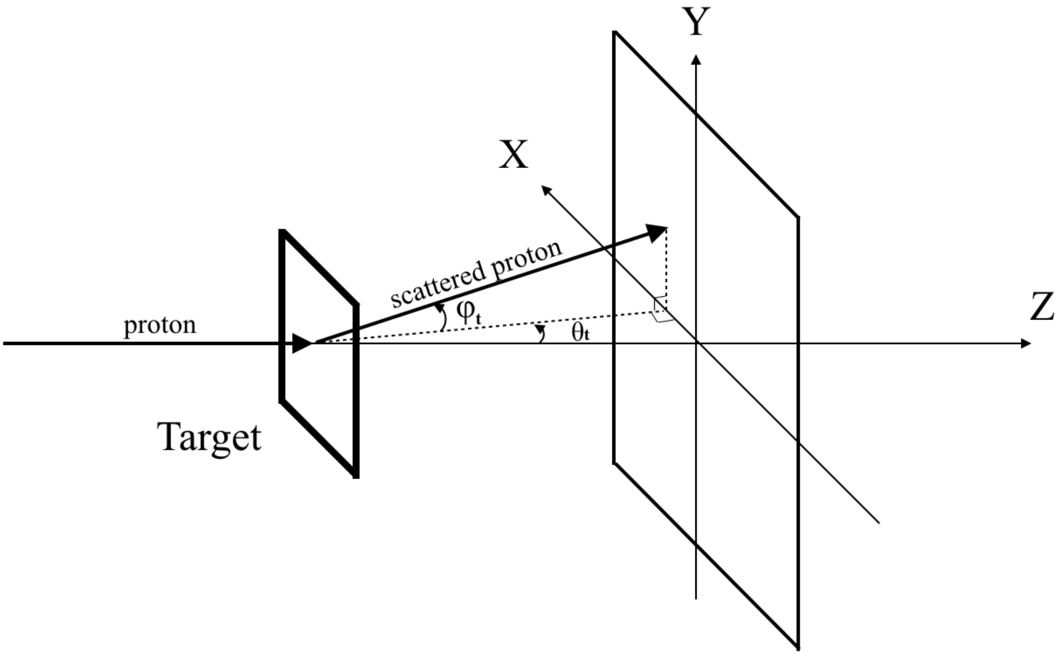

Figure 3.1: Coordinate system at the target position. Z axis is taken to the beam direction. θ_t and ϕ_t are defined as horizontal and vertical scattering angles, respectively.

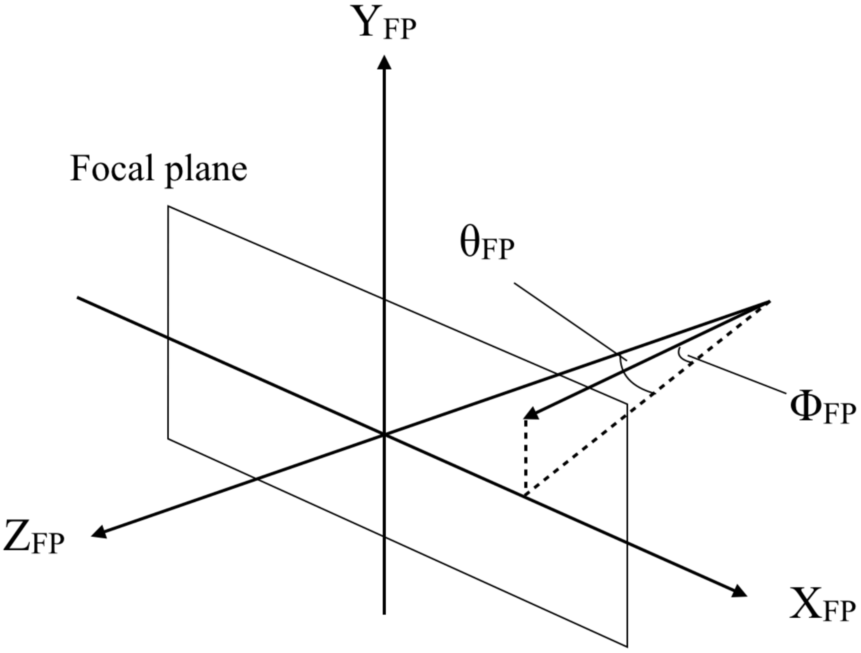

Figure 3.2: Coordinate system at the focal plane. Z axis is taken to the beam direction. θ_{FP} and ϕ_{FP} are defined as horizontal and vertical injection angles, respectively.

3.1.1 Particle identification by the plastic scintillator

The magnetic field of the two dipole magnets of GR was applied to transport scattered 392MeV-protons to the focal plane. However, other charged particles, such as 230MeV-deuterons produced by (p,d) reaction at the target, were also transported to the focal plane. In order to select only scattered protons, particle identification has been carried out using the energy deposit in the plastic scintillator and time-of-flight (TOF).

The scintillation lights in the PS2 were converted into electrons and amplified by 2 PMTs from both sides (left and right). Since the length of PS2 (L) was as long as 1m, the light attenuation has been considered. A light yield (I) detected by the PMT is written as,

$$I(x) = I_0 \exp(-\frac{x}{l}) \tag{3.2}$$

where x is the distance between the detection position and the side end, I_0 is light yield at the detection position and l is the attenuation length of the PS. However, the mean light yield of the left and right PMTs given as,

$$I = \sqrt{I(x)I(L-x)} = I_0 \exp(-\frac{L}{2l}) \tag{3.3}$$

is independent of detection position. The light yield, namely, the energy deposit spectrum is shown in Fig.3.3. The first and the second peaks corresponds to the protons and the deuterons signals, respectively, since the energy deposit of a 230-MeV deuteron in a plastic scintillator with a thickness of 1cm calculated by Bethe-Bloch formula is twice as higher as that of a 392-MeV proton. The red region has been selected as scattered proton events.

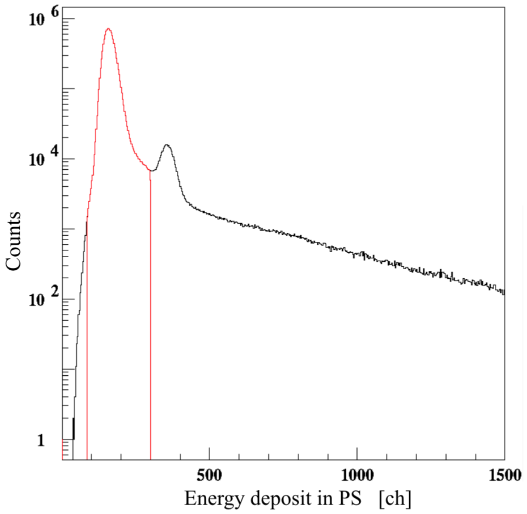

Figure 3.3: ADC histogram of plastic scintillator. The region was selected as scattered proton events.

TOF was measured as the time difference between the trigger timing created by the PS Trigger and the radio frequency signal from the AVF cyclotron. TOF was correlated with the horizontal position X and horizontal scattering angle (θ_{FP}) at the focal plane (see next section for detail). Correlation with θ_{FP} has been corrected as shown in the top panel of Fig.3.4. Subsequently, correlation with X has been corrected as shown in bottom panel of Fig.3.4.

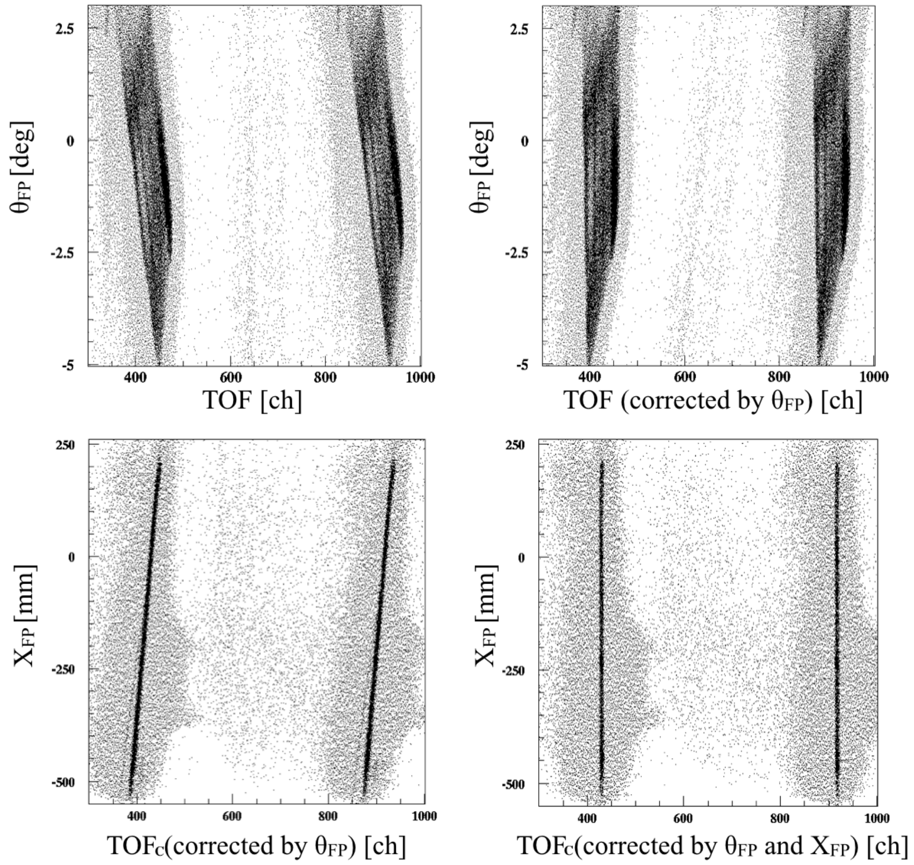

Figure 3.4: Correction of TOF with horizontal scattering angle at the focal plane (top) and horizontal position (botom).

Finally, the corrected TOF ($\mathrm{TOF_c}$) is calculated by

$$\mathrm{TOF_c} = \mathrm{TOF} + 584 \times \theta_{\mathrm{FP}} - 0.0824 \times \mathrm{X_{FP}}, \tag{3.4}$$

where units of $TOF(TOF_c)$, θ_{FP} and X are in ch, radian and mm, respectively. Fig.3.5 shows the $\mathrm{TOF_c}$ spectrum. The difference between the two peaks corresponds to the beam bunch period of 59.4 ns. The red region has been selected as scattered proton events.

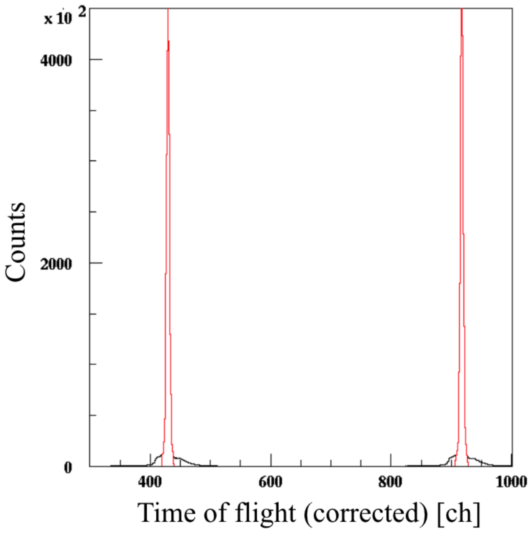

Figure 3.5: Time of flight spectrum after corrections. The red region has been selected as scattered protons.

3.1.2 Track reconstruction by MWDC analysis

The structure of MWDC is shown in Fig.2.6. The analysis of MWDC has been done as follows,

- Drift time to drift length conversion
- Trajectory reconstruction
- Optical correction
- Calibration of scattering angle at target

Drift time to drift length conversion

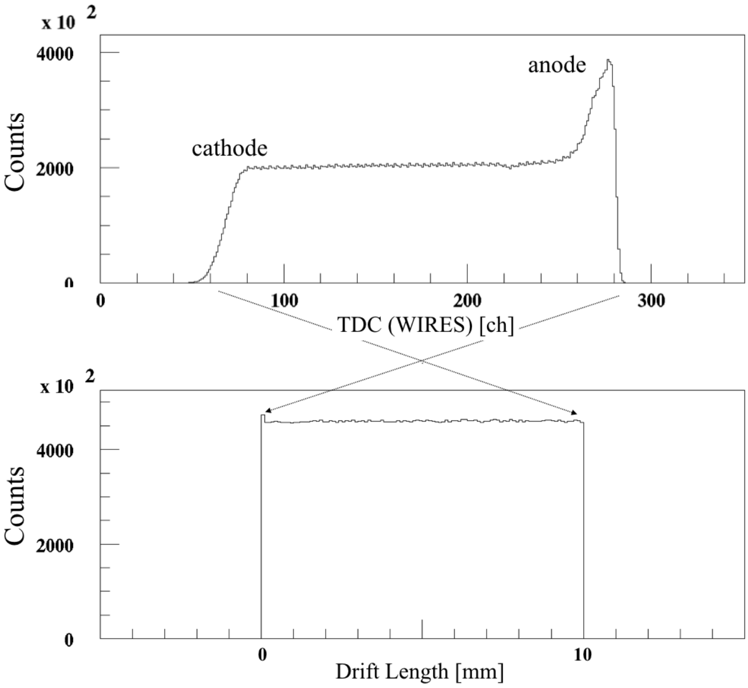

Figure 3.6: Drift time (up) to drift length (down) conversion.

A charged particle passing through the MWDC hits 3 or 4 wires. The time difference between the PS Trigger and the hit timing of each wire was recorded by TDC which corresponds to the drift time. Since the drift velocity is constant except around the wires, the vertical drift length ($\mathrm{d_{i-1}}, \mathrm{d_i}, \mathrm{d_{i+1}}$, ... in Fig.2.6) was calculated from the drift time. The conversion tables from the drift time to the drift length have been created using a flat continuum spectrum as shown in Fig.3.6.

Trajectory reconstruction

In the determination of the trajectory, each plane was required to have at least more than 2 adjacent hit wires, which are grouped as a cluster, and have only one cluster. The intercept position of a trajectory at a wire plane was calculated by a least-square fit of the drift lengths of hit wires in a cluster . By combining the positions at the four wire planes, a three-dimensional trajectory was uniquely determined. Then the vertical (horiziontal) position X (Y) in mm and the vertical (horiziontal) angle θ_{FP} (ϕ_{FP}) in radian at the focal plane have been derived.

Tracking efficiency

The tracking efficiency of X1 plane at excitations energy was estimated as a function of excitation energy (E_x) by,

$$\eta_{X1}(E_x) = \frac{N_{U1\&X2\&U2}}{N_{U1\&X2\&U2} + N_{X1\&U1\&X2\&U2}} \tag{3.5}$$

where $N_{U1\&X2\&U2}$ is the number of trajectories successfully reconstructed by U1, X2 and U2 planes and $N_{X1\&U1\&X2\&U2}$ by all the four planes. E_x was estimated form the time difference between the left and right readouts of the plastic scintillator ($\frac{\Delta E_x}{E_x}$ ~1MeV). The efficiencies of other planes were calculated in the same way as shown in Fig.3.7. Finally, the total efficiency is given by,

$$\eta(E_x) = \eta_{X1}(E_x) \times \eta_{U1}(E_x) \times \eta_{X2}(E_x) \times \eta_{U2}(E_x). \tag{3.6}$$

The total efficiency was 93% and the it's dependence on E_x was smaller than 1% (shown in black line in Fig.3.7).

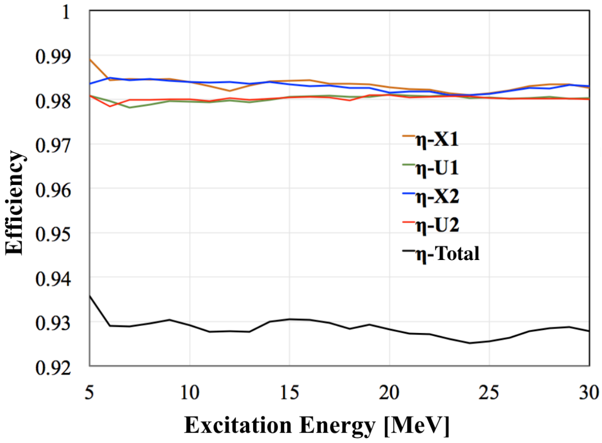

Figure 3.7: Trajectory reconstruction efficiency.

Optical correction

The correlation of X_{FP} with θ_{FP} and that of Y_{FP} with X and ϕ_{FP} due to the ion optical property of GR have been corrected as,

$$X_{FPc} = \sum_{ij} A_{ij} X^i_{FP} \theta^j_{FP} \tag{3.7}$$

$$Y_{XPc} = Y + \sum_{ij} B_{ij} X^i_{FP} \phi^j_{FP} \tag{3.8}$$

where X_{FPc} (Y_{FPc}) denotes the horizontal (vertical) position after correction and the correction parameters A_{ij} (B_{ij}) are summarized in Tab.3.2. The correction results are shown in Fig.3.8. X_{FP} correction resulted in better energy resolution and Y_{FP} correction improved the background subtraction reliability (see Sec.3.1.3).

Table 3.2: Correction parameters for X_{FPc} and Y_{FPc}.

i	j	A_{ij}	i	j	B_{ij}
0	0	$0.00 \times 10^{+0}$	0	0	$-4.11 \times 10^{+0}$
0	1	$-3.34 \times 10^{+2}$	0	1	$2.27 \times 10^{+3}$
0	2	$3.35 \times 10^{+3}$	1	0	1.16×10^{-2}
1	0	9.94×10^{-1}	1	1	$-3.14 \times 10^{+0}$
1	1	$-1.18 \times 10^{+0}$	2	0	-5.06×10^{-6}
1	2	6.67×10^{-1}	2	1	4.10×10^{-3}
2	0	-1.28×10^{-5}	3	0	4.84×10^{-8}
2	1	-7.55×10^{-4}	3	1	-1.39×10^{-5}
2	2	5.74×10^{-4}			

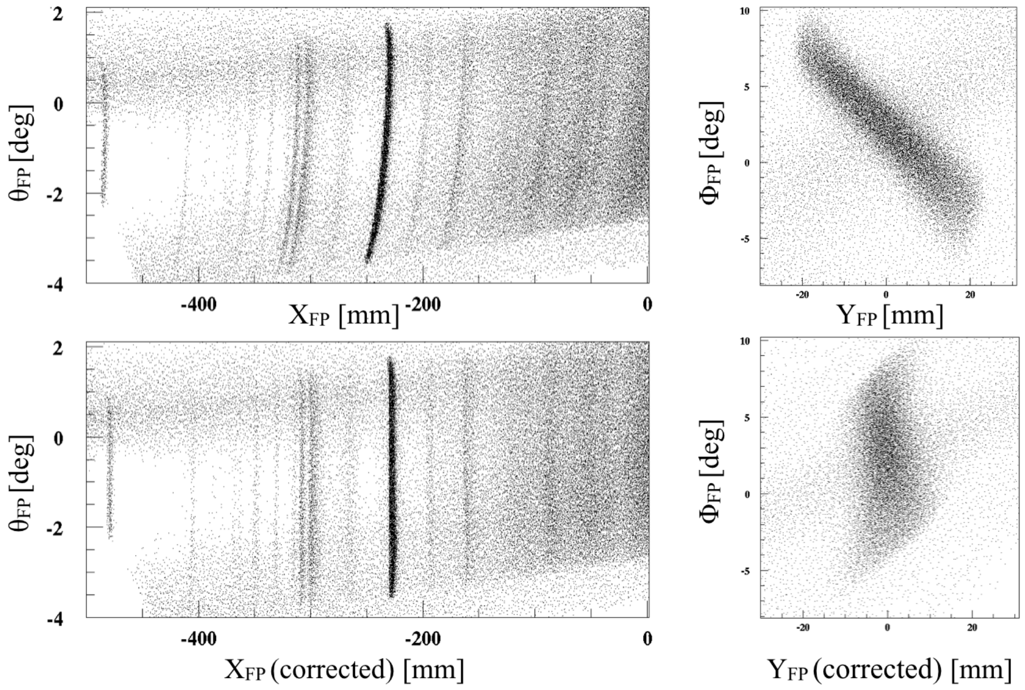

Figure 3.8: Correlation of horizontal (left) and vertical (right) position with angles at the focal plane before (top) and after (bottom) correction.

Calibration of scattering angle at target using sieve-slit data

The scattering angle was calibrated by elastic scattering data at $\theta = 2.5°$ using a sieve-slit. The sieve-slit is a plate with 25 holes as shown in Fig.3.9, which was mounted in the entrance of GR (580 mm downstream to the target). A particle passing through each hole has a unique scattering angle at the target position.

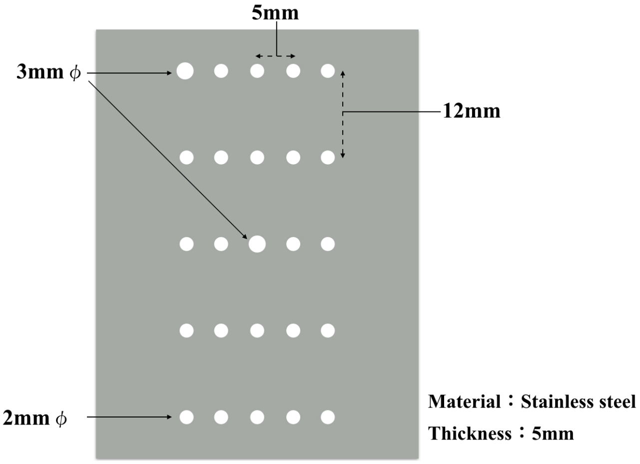

Figure 3.9: Design of a sieve-slit used for calibration of scattering angle.

The data were taken at 5 different E_x's, by changing magnet parameters. The typical correlation between θ_{FP} and Y_{FPc} is shown in the top panel of Fig.3.9. 23 holes are seen and 2 holes are missing due to the acceptance of GR. The horizontal and vertical scattering angles at the target position (θ_t and ϕ_t) have been reconstructed analytically from the trajectory at the focal plane (X_{FPc}, Y_{FPc}, θ_{FP} and ϕ_{FP}) by a multi-dimensional least squares fitting as

$$\theta_t = \sum_{ij} A_{ij} X^i_{FPc} \theta^j_{FP}, \tag{3.9}$$

$$\phi_t = \sum_{ijkl} B_{ijkl} X^i_{FPc} \theta^j_{FP} Y^k_{FPc} \phi^l_{FP}, \tag{3.10}$$

where the reconstruction parameters A_{ij} and B_{ijkl} are summarized in Tab.3.3 and Tab.3.4, respectively. The reconstruction result is shown in the bottom panel of Fig.3.10. The angular resolutions (FWHM) were derived from the gaussian fits to the points as 0.12° for θ_t and 0.7° for ϕ_t. Figure 3.11 shows an example of the scattering angle distribution (θ_t, ϕ_t) taken in $\theta = 0°$ data. The shape corresponds to the entrance of spectrometer, that is, acceptance.

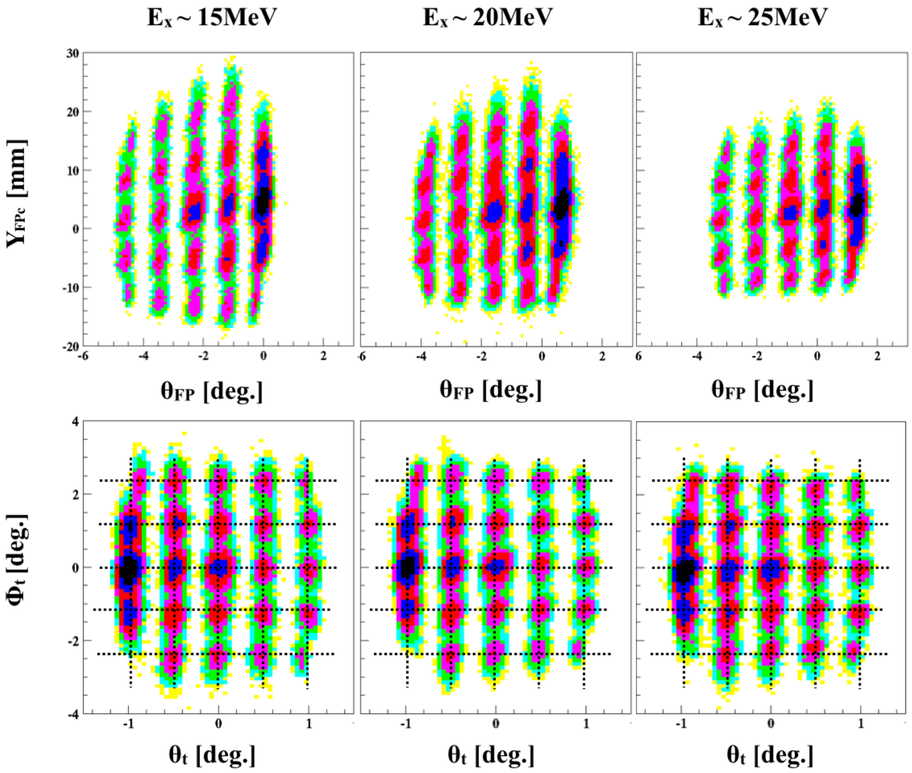

Figure 3.10: The reconstruction of the scattering angle with sieve-slit. The trajectory at the focal plane (top) was converted to the scattering angle at the target position (bottom). The cross points of dotted lines in bottom figures correspond to the true scattering angles of the holes.

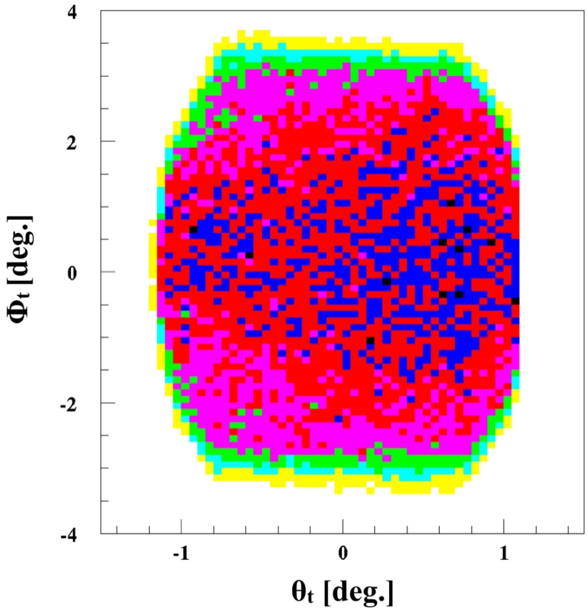

Figure 3.11: Scattering angle distribution (θ_t, ϕ_t) taken in $\theta = 0°$ data.

Table 3.3: Reconstruction parameters for θ_t.

i	j	A_{ij}
0	0	-1.30×10^{-3}
1	0	2.54×10^{-5}
0	1	$-0.441 \times 10^{+0}$

Table 3.4: Reconstruction parameters for ϕ_t.

i	j	k	l	B_{ijkl}	i	j	k	l	B_{ijkl}
0	0	0	0	-1.05×10^{-4}	1	0	0	0	1.31×10^{-5}
0	0	0	1	$2.12 \times 10^{+0}$	1	0	0	1	-2.63×10^{-3}
0	0	1	0	-2.37×10^{-3}	1	0	1	0	-1.90×10^{-6}
0	0	1	1	-9.32×10^{-3}	1	0	1	1	-1.40×10^{-5}
0	1	0	0	6.55×10^{-2}	1	1	0	0	-3.11×10^{-5}
0	1	0	1	$3.05 \times 10^{+0}$	1	1	0	1	5.52×10^{-2}
0	1	1	0	-1.52×10^{-4}	1	1	1	0	1.01×10^{-5}
0	1	1	1	-1.51×10^{-1}	1	1	1	1	-1.09×10^{-4}

3.1.3 Excitation energy spectrum and background subtraction

The momentum (p) of the scattered proton due to the circular motion with an orbit radius (ρ) of 3 m in a magnetic field of GR (B=1017mT) was calculated as a function of X_{FPc} by

$$p(X_{FPc}) = e\rho B. \tag{3.11}$$

Then the rough excitation energy E_{x_0} of the target was calculated relativistically from $p(X_{FPc})$. The excitation energy (E_x in MeV) was further calibrated by comparing the excitation energies of well-known states of ^{12}C and ^{16}O seen as peaks in the data with those from Table of Isotopes [8] by

$$E_x \text{ (keV)} = \begin{cases} E_{x_0} + 2.07 \text{ (keV)} & (E_{x_0} < 15.0). \\ 1.035 \times E_{x_0} + 2.07 & (E_{x_0} > 15.0). \end{cases} \tag{3.12}$$

After the calibration, E_x's of well-known states agreed with table values [8] within 60 keV as shown in Fig3.12.

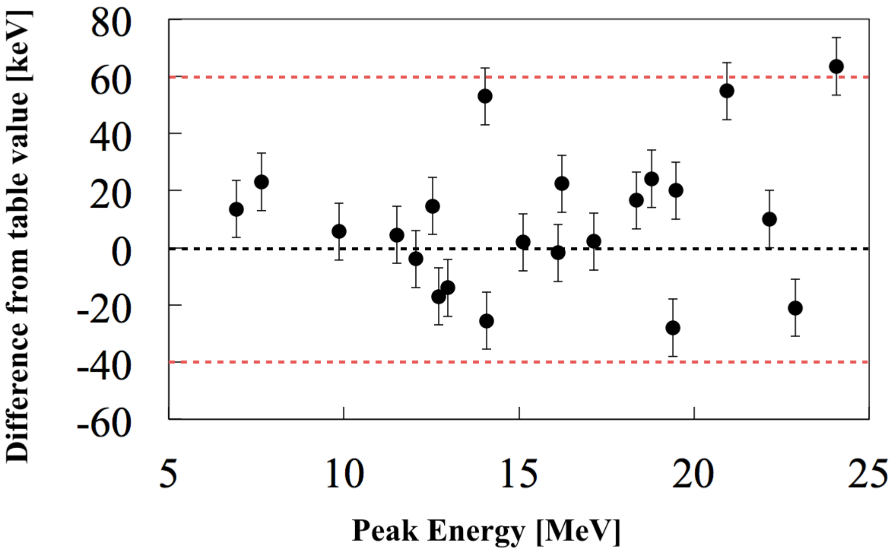

Figure 3.12: Difference of peak energies between data and table values [8].

Background subtraction

The Y_{FPc} spectrum is shown in the left panel of Fig.3.13. The peak around 0 mm (red) contains both true and background events. The background events due to multiple scatterings at the target were uniformly distributed as seen in the figure. Therefore, the background events in the red region were used to subtract the background in the true region (blue). For example, the excitation energy spectra of ^{12}C gated by Y_{FPc} true cut (blue) and Y_{FPc} background cut (red) are shown in the right panel of Fig.3.13. Below 26 MeV, the systematic uncertainty due to the background subtraction was estimated to be less than 1%. Since the background becomes larger above 26 MeV, the systematic uncertainty became as large as 13% at E_x ∼33 MeV.

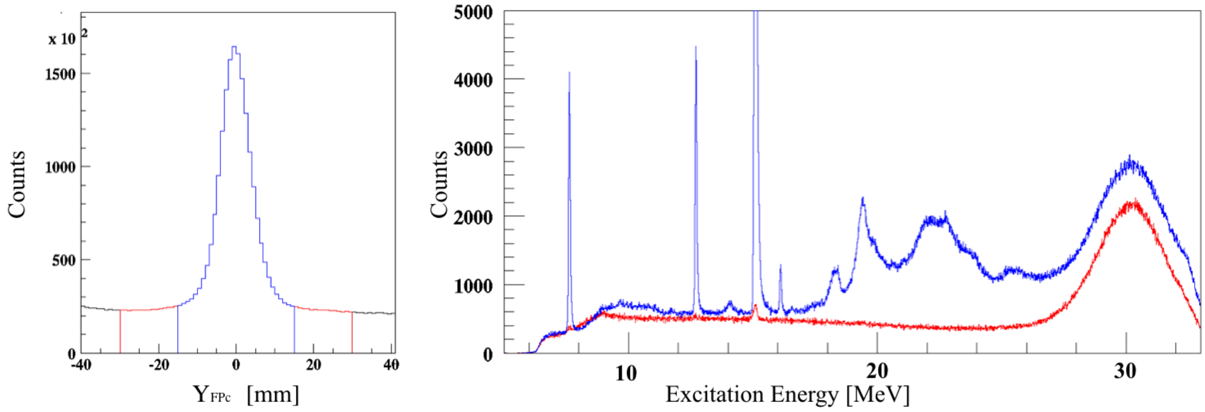

Figure 3.13: Y_{FPc} spectrum (left) and excitation energy spectrum (right). Background events were uniformly distributed in Y_{FPc} spectrum. The side band region (red) were subtracted from the true region (blue).

3.1.4 Subtraction of ^{12}C data from $C_6H_{10}O_5$ data

Excitation energy spectra of ^{12}C data target with total beam charge of 37333 nC data and cellulose ($C_6H_{10}O_5$) target with total beam charge of 63650 nC are shown in the top and middle panel of Fig.3.14. The ^{12}C spectrum was scaled by the subtraction factor (S_f) of 0.203 defined by Eq.(3.13) and then subtracted from the $C_6H_{10}O_5$ spectrum to obtain the excitation energy spectrum of ^{16}O.

$$S_f = \frac{t_{cellulose} \times M_r \times Q_{cellulose}}{t_C \times Q_C}, \tag{3.13}$$

where t is the thickness of the target, Q is the total beam charge and M_r is the mass ratio of C in $C_6H_{10}O_5$ (=72/162). On the other hand, the raw number of events of the discrete peak of ^{12}C at $E_x = 7.65$ MeV was 260669 for ^{nat}C data and 52070 for $C_6H_{10}O_5$ data, respectively. Since there is no nearby states of ^{16}O in this energy region, S_f can be directly estimated as $54070/260669 = 0.207$. The difference of 3% between the two method was taken into account as the systematic uncertainty of the subtraction.

The excitation energy spectrum of ^{16}O is shown in the bottom panel of Fig.3.14. Since the energy resolutions in ^{12}C data and $C_6H_{10}O_5$ data were different, some unusual shapes (shaded area) are seen. This effect is negligible in the giant resonances region, since the widths of the resonances are much broader. The excitation energy spectrum of ^{16}O is very similar to that measured with an ice target by Kawabata *et al.* [38], which verifies the subtraction method.

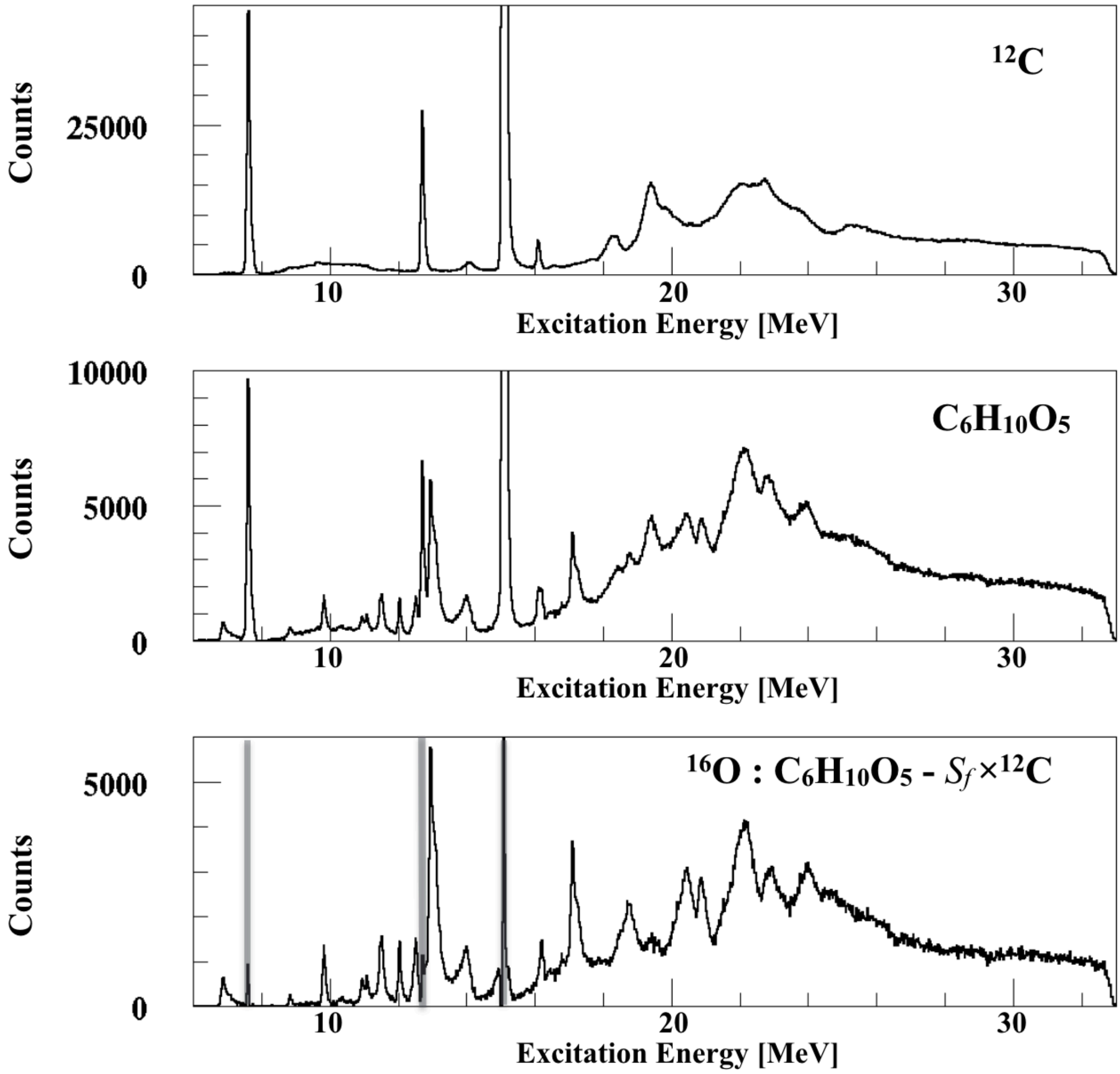

Figure 3.14: Excitation energy spectra of ^{12}C target (top), cellulose ($C_6H_{10}O_5$) target (middle) and ^{16}O (bottom). Some wired shapes in the shade area of ^{16}O were seen due to the difference of the energy resolution between targets.

3.2 Analysis of γ-ray detector

3.2.1 Coincidence with the spectrometer

The time information of γ-ray detector was recorded for each event. The time difference between γ-trigger and PS-trigger gated by the $J^{\pi} = 1^{+}$ state of ^{12}C at 15.11 MeV is plotted in the left panel of Fig.3.15. The first peak (red) was selected as coincidence events and the others (blue) to the accidental coincidence (background) events with other off-timing bunches (interval time of 60 ns). In addition, the time differences between the γ-trigger and discriminator pulse of 25 NaI counters were recorded. For example, the time differences between the γ-trigger and the discriminator pulse of NaI9 is shown in the right panel of Fig.3.15. The red region was selected as coincidence events for each counter.

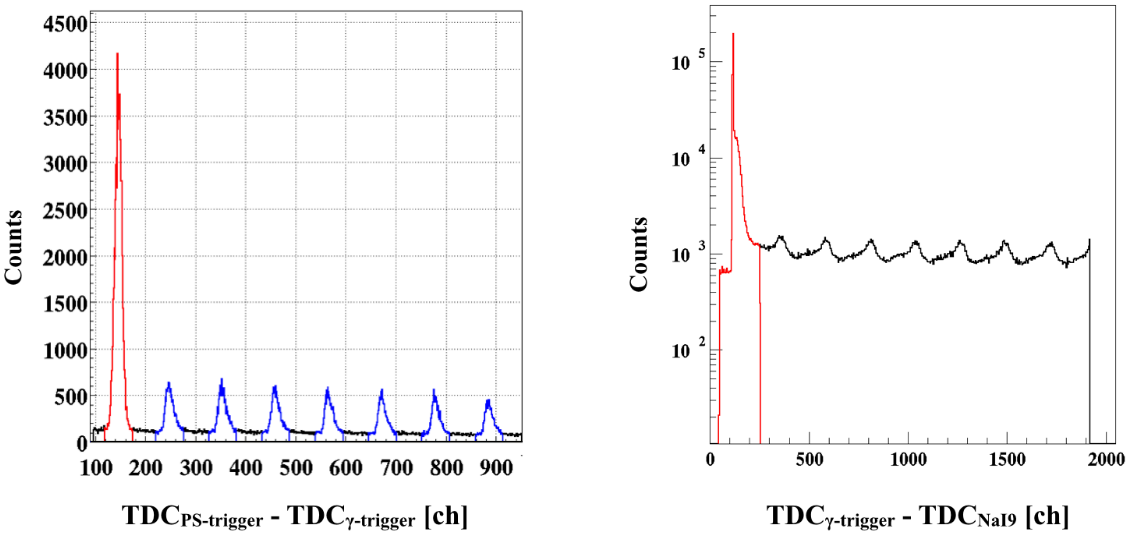

Figure 3.15: Time difference between γ-trigger and PS-trigger (left) and time difference between γ-trigger and each discriminator pulse of NaI9 counter (right).

3.2.2 Energy calibration

(1) Energy calibration before the beam time

The γ-ray energy was calibrated before the beam time using ^{60}Co source which emits 2 γ rays (1173 keV and 1332 keV). The left panel of Fig.3.16 shows a typical ADC spectrum for ^{60}Co. The sum peak with energy of $1173 + 1332 = 2505$keV is also seen. In addition to the γ rays from ^{60}Co, a clear peak with lower energy is seen. The energy was measured to be 834 ± 2 keV by Ge counter as shown in the right panel of Fig.3.16. This γ ray was emitted from the β-decay from ^{54}Mn into ^{54}Cr. ^{54}Mn was thought to be created by radioactivation of the magnets of the spectrometer. Finally, energy calibration was carried out for each counter using 834-keV, 1173-keV, 1332-keV and 2505-keV γ rays. In Fig.3.17, the calibrated energy spectra of 25 NaI counters in the energy range from 1000 keV to 1500 keV are shown (black) together with fitting lines by 2 gaussian + polynomial function (red). 1.17 MeV and 1.32 MeV peaks are clearly seen in all counters.

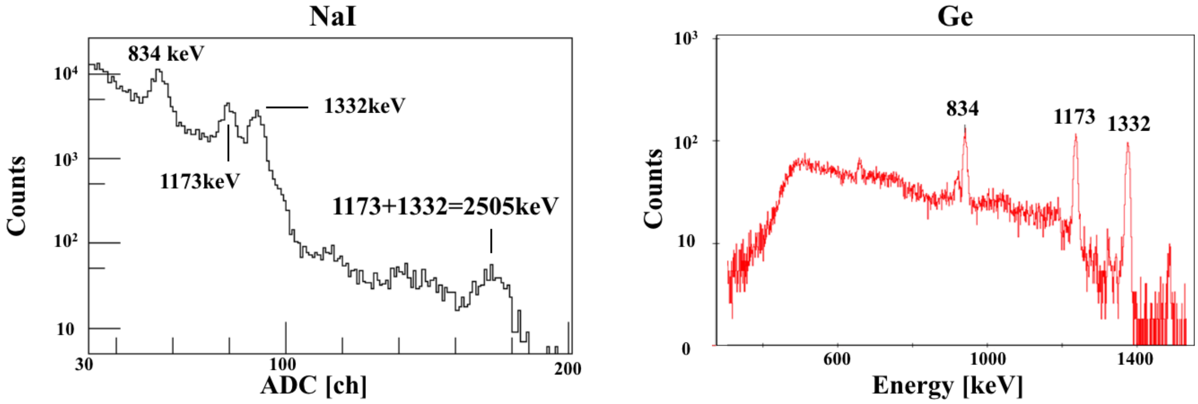

Figure 3.16: ADC spectra of ^{60}Co measured by a NaI counter (left) and a Ge counter (right).

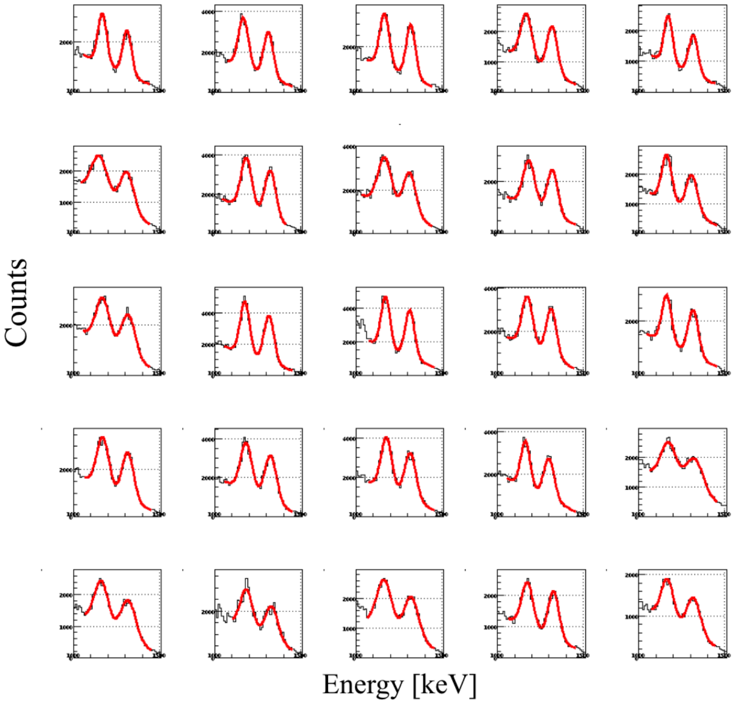

Figure 3.17: Energy spectra of ^{60}Co measured by 25 NaI counters. The X axis ranges from 1000 keV to 1500keV. 1.17 MeV and 1.32 MeV peaks are clearly seen in all counters.

Energy calibration during the beam time.

The energy was re-calibrated using following γ-ray sources for the data taken during the beam runs:

1. 15.11-MeV γ ray from the $J^\pi = 1^+$ state of ^{12}C at 15.11 MeV
   A 15.11-MeV γ ray is emitted with 88.4 % probability [39].

2. 2.12-MeV γ ray from the $J^\pi = 1/2^-$ state of ^{11}B at 2.12 MeV
   ^{12}C can decay either into the ground state of daughter nuclei without emission of γ ray or into the $J^\pi = 1/2^-$ state of ^{11}B at 2.12 MeV with emission of a 2.12-MeV γ ray.

3. 1.37-MeV γ ray in the background spectrum
   In the background spectrum, a peak was seen for all counters. The mean energy was measured to be 1.37 MeV by a Ge counter. This γ ray was emitted by

$$\mathrm{n} + {}^{27}\mathrm{Al} \rightarrow {}^{28}\mathrm{Al} \rightarrow {}^{24}\mathrm{Na} + \alpha \tag{3.14}$$

$$^{24}\mathrm{Na} \rightarrow {}^{24}\mathrm{Mg} + \mathrm{e}^- + \overline{\nu_\mathrm{e}} + \gamma\ (1.37\mathrm{MeV}) \tag{3.15}$$

   where neutron (n) is created by the radioactivation of the spectrometer by the beam and ^{27}Al is contained in the aluminum scattering chamber.

Typical energy spectra of these γ rays are shown in Fig.3.18. The peak of 15.1MeV is located slightly lower than 15.1 MeV because the photo peak and single- and double- escape overlap with each other.

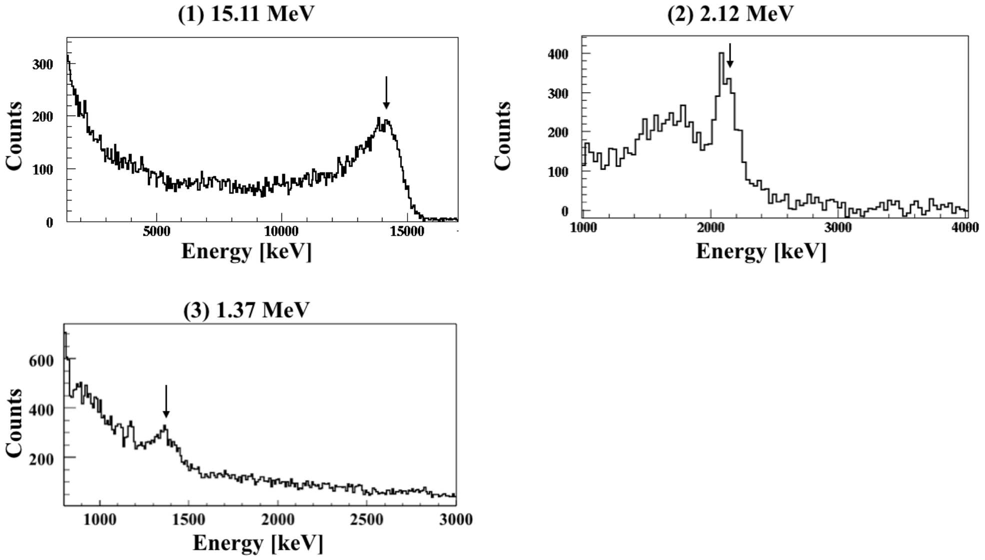

Figure 3.18: Energy spectra of different γ-ray energies in the beam time.

3.2.3 Gain shift correction

Figure 3.19 shows a typical ADC spectrum of 15.1-MeV γ ray measured at the beginning (red) and the end (blue) of the experiment. Due to the radioactivation of NaI counters by the scattered protons, the gain of the PMT have been decreased gradually during the beam time. As a result, the energy resolutions of 15 counters located downstream of the beam became very poor, only 10 counters located upstream of the beam were used in the present analysis.

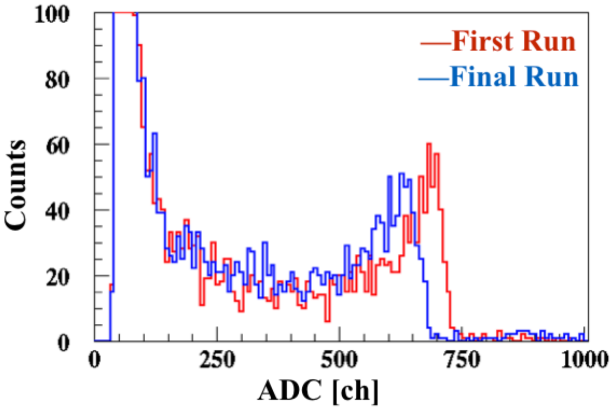

Figure 3.19: ADC spectrum of 15.1-MeV γ ray measured at the beginning (red) and the end (blue) of the experiment measured by a single NaI counter. A decrease of the gain is clearly seen.

We corrected for the gain shift using 15.1-MeV γ ray for all runs and all counters. First, the spectrum around the peak region was fitted by an asymmetric gaussian distribution defined by,

$$f(ADC) = p_0 \exp(\frac{(ADC - p_1)^2}{2\sigma(ADC)^2}), \quad \sigma(ADC) = p_3(ADC - p_1) + p_2, \tag{3.16}$$

where σ is the resolution, p_0 is the height, p_1 is the center and p_2 and p_3 are asymmetric parameters, respectively. The fit example is shown in red line in Fig.3.20.

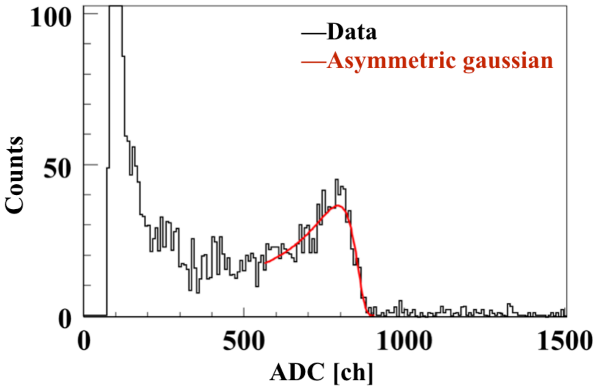

Figure 3.20: A fit example to the 15.1-MeV peak by an asymmetric gaussian.

In Fig.3.21, the gain shift parameter (g_s) defined as $g_s = p_1 + \sigma$ for each run is plotted for each NaI counter. According to the detector simulation, the peak energy (p_1) is smaller than 15.1 MeV due to the detector resolution, while g_s is closer to 15.1 MeV. Thus the energy was corrected by the gain shift parameter g_s for each run with respect to that of the first run.

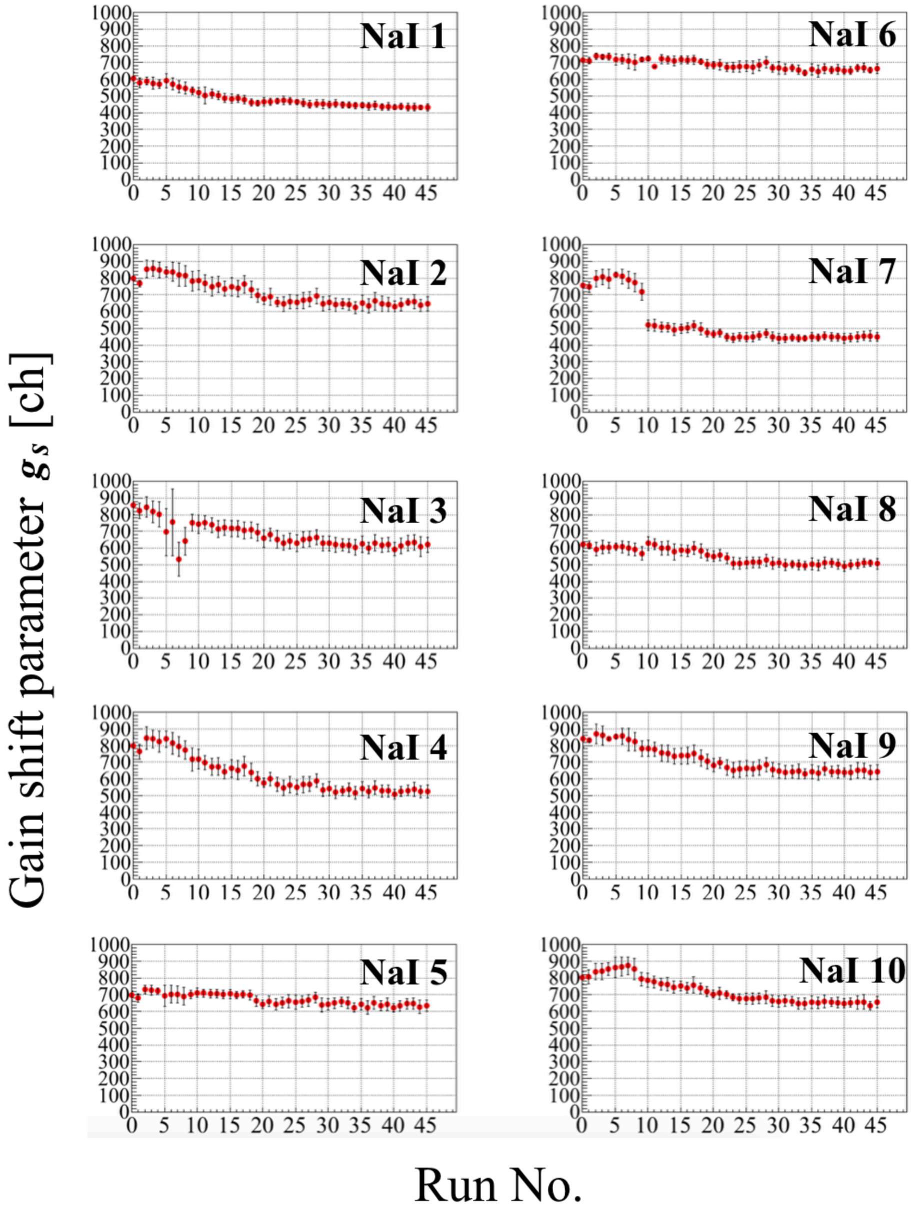

Figure 3.21: Gain shift parameter g_s for each run and each NaI counter.

3.2.4 Background subtraction

The left panel in Fig.3.22 shows the TDC spectrum gated by the $J^\pi = 1^+$ state of ^{12}C at 15.11 MeV. The coincidence peak (red) contains not only the true events, but also accidental coincidence events (background). Therefore, the energy spectrum gated by the other peaks shown in blue, which contain only the background events, was normalized and subtracted from the coincidence spectrum as described before.

Determination of the normalization factor for background subtraction.

In order to determine the normalization factor N_f, a background template TDC spectrum shown in the right panel of Fig.3.22 was used. This spectrum was derived by gating the background events in the spectrometer analysis using Y_{FPc} side band (see Sec.3.1.3). Therefore, even the first peak contains background events and N_f was directly derived from the number of events in the red region divided by the total number of events in blue region. N_f was determined for each run. For the runs with a beam intensity of 0.5 nA, a typical S_c value ranged from 0.172 to 0.181.

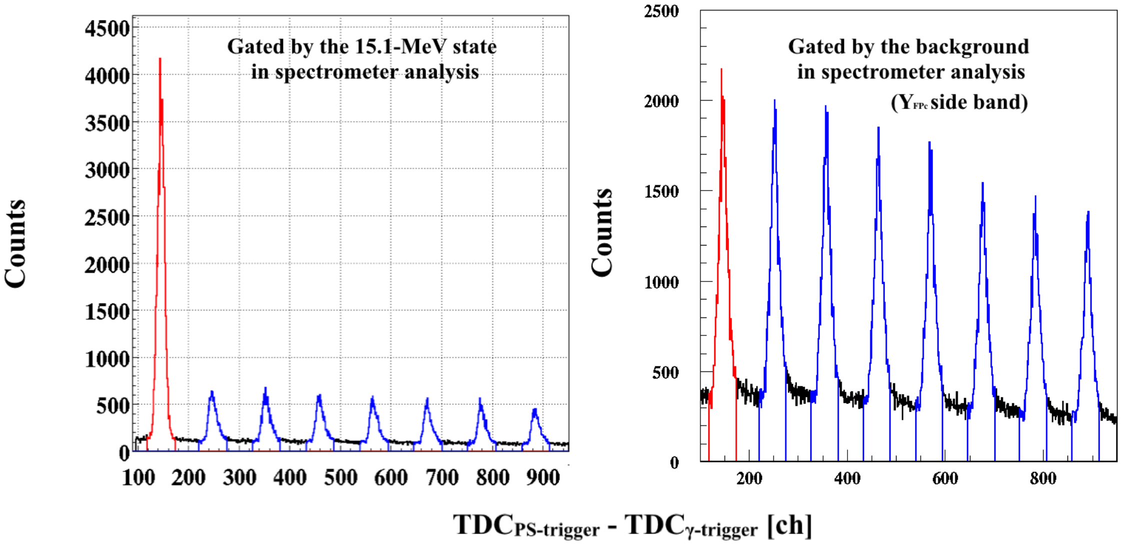

Figure 3.22: Time difference between γ-trigger and PS-trigger gated by the $J^\pi = 1^+$ state of ^{12}C at 15.11 MeV (left) and background events (right) in the spectrometer analysis.

The left panel of Fig.3.23 shows the coincidence energy spectrum from the $J^\pi = 1^+$ state of ^{12}C at 15.11 MeV (red) together with the background spectrum (blue). The background events seen as a bump at 20 MeV due to the scattered protons has been subtracted in this procedure.

Validity of the background subtraction.

The coincidence spectrum (red) and the background spectrum (blue) from the $J^\pi = 0^+$ state of ^{12}C at 7.65 MeV are plotted in the right panel of Fig.3.23. Since the decay from this state is dominated by α decay and the γ-decay probability is as small as 0.046 ± 0.012 % [39]

and can be neglected, it is the ideal state to check the validity of the background subtraction method. The total number of coincidence events was 4062 and that of the background spectrum was 4091, which resulted in the real coincidence events of -29 ± 128(stat.). The result was consistent with null event within statistical uncertainty. A systematic error of 2% was estimated for the γ-ray background subtraction.

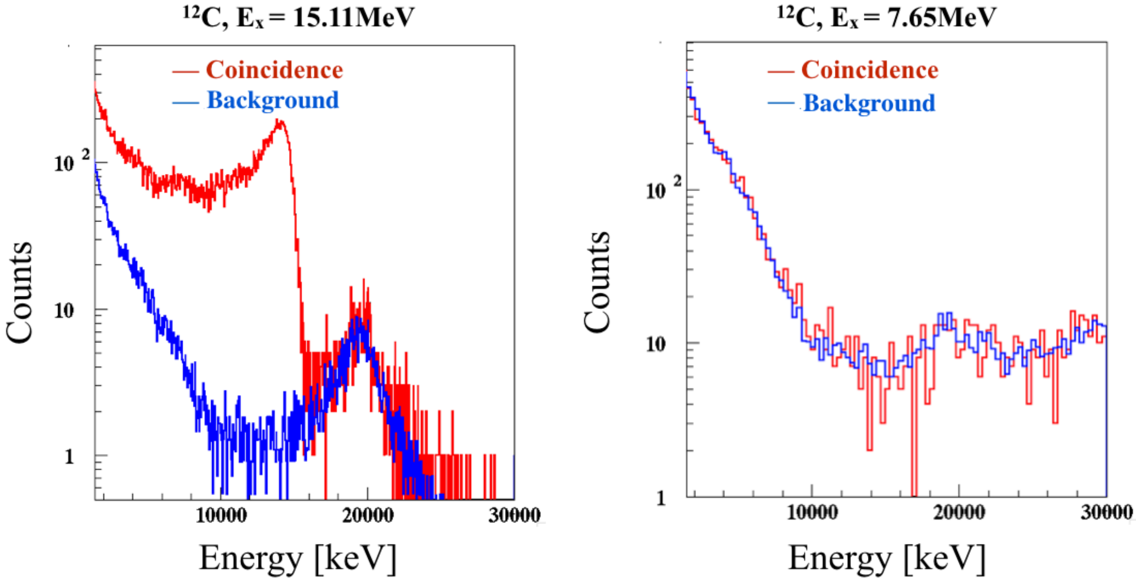

Figure 3.23: Coincidence energy spectra (red) and background energy spectra (blue) gated by the $J^\pi = 1^+$ state of ^{12}C at 15.11 MeV (left) and the $J^\pi = 0^+$ state of ^{12}C at 7.65 MeV (right).

3.2.5 Energy spectra

The sum of the energy spectra measured by 10 NaI counters was defined as an array energy spectra. Figure 3.24 shows the array energy spectra gated by several states using all runs with an intensity of 0.5 nA (black) together with the background spectra (red).

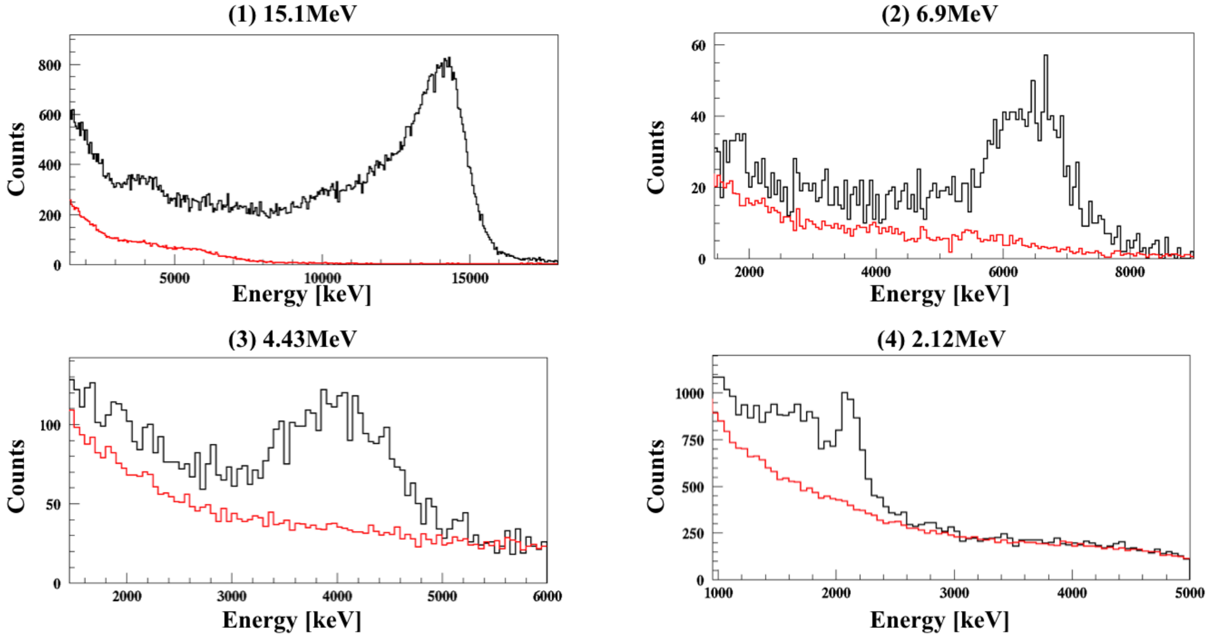
(1) 15.1MeV

(2) 6.9MeV

(3) 4.43MeV

(4) 2.12MeV

Figure 3.24: The array energy spectrum gated by the ^{12}C and ^{16}O states. Black and red lines are the coincidence and background spectra, respectively.

1. $J^\pi = 1^+$ state of ^{12}C at 15.11 MeV
   The decay width of the 15.11 MeV sate and relevant states are summarized in Tab.3.5 [39]. The γ-ray emission probability was deduced from Tab.3.5 and is summarized in Tab.3.6. Although the dominant 15.11-MeV γ ray is clearly seen as a peak in the spectrum, other cascade γ rays such as 4.43-MeV and 10.66-MeV γ rays are also seen as small bumps.

2. $J^\pi = 2^+$ state of ^{16}O at 6.92 MeV
   6.92-MeV γ ray is emitted from this state with a probability of 100 % [39]. 6.92-MeV photo peak and single- and double- escape peaks are seen as one broad peak in the spectrum.

3. $J^\pi = 2^-$ state of ^{16}O at 12.97 MeV
   The decay width is summarized in Tab.3.7 [40]. For proton decay, this state can only decay to the ground state of ^{15}N without γ-ray emission. On the other hand, the α decay to the ground state ($J^\pi = 0^+$) of ^{12}C is prohibited due to the parity conservation [41]. Therefore, it can only decay to the first excited state ($J^\pi = 2^+$) of ^{12}C at 4.43 MeV which further decays to the ground state by emitting a 4.43-MeV γ ray. 4.43-MeV photo peak and single- and double- escape peaks are seen as one broad peak in the spectrum. The direct γ-decay was not taken into account since it is less than 0.15% [8].

Table 3.5: The decay width of ^{12}C states [39]. Total decay width (Γ) is the sum of α-decay width (Γ_α), π-decay width (Γ_π) and γ-decay width (Γ_γ). Radioactive decay width (Γ_{rad}) is the sum of Γ_π and Γ_γ.

E_x [MeV]	Decay width
4.44	$\Gamma = \Gamma_\gamma = 10.8 \pm 0.6$ meV
7.65	$\Gamma = 8.3 \pm 1.0$ eV $\Gamma_\pi = 60.5 \pm 3.9$ μeV $\Gamma_{rad} = 3.7 \pm 0.5$ meV
12.71	$\Gamma = 18.1 \pm 2.8$ eV $\Gamma_\alpha = 17.7 \pm 2.8$ eV $\Gamma_\gamma(12.71 \to 0) = 0.35 \pm 0.05$ eV $\Gamma_\gamma(12.71 \to 4.44) = 0.053 \pm 0.010$ eV
15.11	$\Gamma = 43.6 \pm 1.3$ eV $\Gamma_\alpha = 1.8 \pm 0.3$ eV $\Gamma_\gamma(15.11 \to 0) = 38.5 \pm 0.8$ eV $\Gamma_\gamma(15.11 \to 4.44) = 0.96 \pm 0.13$ eV $\Gamma_\gamma(15.11 \to 7.65) = 1.09 \pm 0.1$ eV $\Gamma_\gamma(15.11 \to 12.71) = 0.59 \pm 0.14$ eV

Table 3.6: The γ-ray emission probability of the $J^\pi = 1^+$ state of ^{12}C at 15.11 MeV (calculated from Tab.3.5).

E_γ [MeV]	Probability [%]
2.40	1.4
4.44	2.2
7.45	2.6
10.66	2.2
15.11	88.4

4. ^{12}C state at 18.0-20.4 MeV
   2.12-MeV γ ray can be emitted from this state as already mentioned in Sec.3.2.2. Although the emission probability is not known, the 2.12 MeV photo peak is clearly seen in the spectrum.

Precision of measured γ-ray energy

In order to estimate the precision of measured γ-ray energy, the peak energies (E_γ^{Data}) were compared to those predicted by a detector simulation (E_γ^{MC}) in Fig.3.25 (see next section for the simulation). The uncertainty of the measured energy was estimated to be about 3% in the energy range of 2 $\sim$ 15 MeV.

Table 3.7: The decay width of $J^\pi = 2^-$ state of ^{16}O at 12.97 MeV. Total decay width (Γ) is the sum of α-decay width (Γ_α), proton decay width (Γ_p) and γ-decay width (Γ_γ) [40].

E_x [MeV]	Decay width
12.97	$\Gamma = 1.34 \pm 0.04$ keV $\Gamma_\alpha = 0.30 \pm 0.06$ eV $\Gamma_p = 1.04 \pm 0.07$ keV $\Gamma_\gamma = 1.6 \pm 0.3$ eV

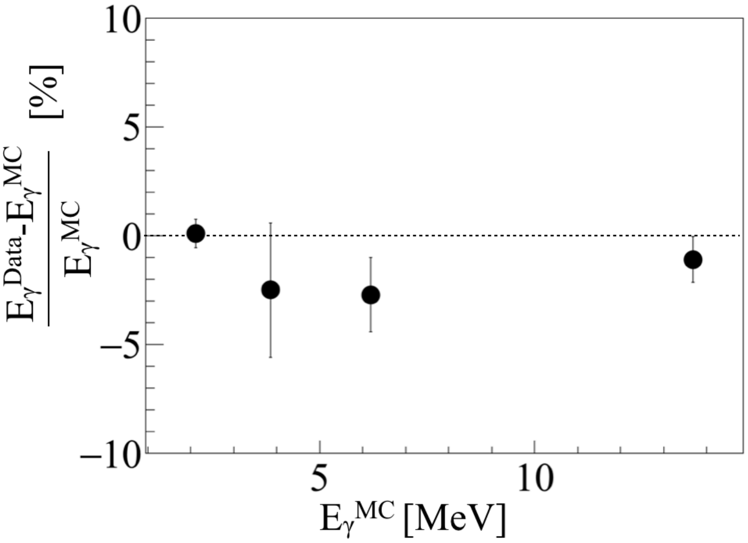

Figure 3.25: Precision of the γ-ray energy.

3.2.6 γ-ray detector simulation by Geant4 code

Geant4 is a toolkit for the Monte Carlo simulation (MC) of the passage of particles through matter [36].

Geometrical setup

We introduced NaI counters and surrounding materials such as lead, plastic scintillator, scattering chamber, target ladder, etc into the simulation. Figure 3.26 shows the geometrical setup in the simulation. Then, the response to the γ rays emitted from the target point was simulated.

Energy spectrum comparison with data for each counter.

The left panel of Fig.3.27 shows the measured energy spectra (black) gated by the ^{12}C state at 15.1 MeV together with the predictions by MC (red) for 10 counters. The MC was normalized by the excitation counts measured by the spectrometer and the γ-ray emission probability in Tab.3.6 ($N_{E_x} \times Pr_\gamma$).

Although the MC reproduces the shape of the spectrum for each counter, it is higher than

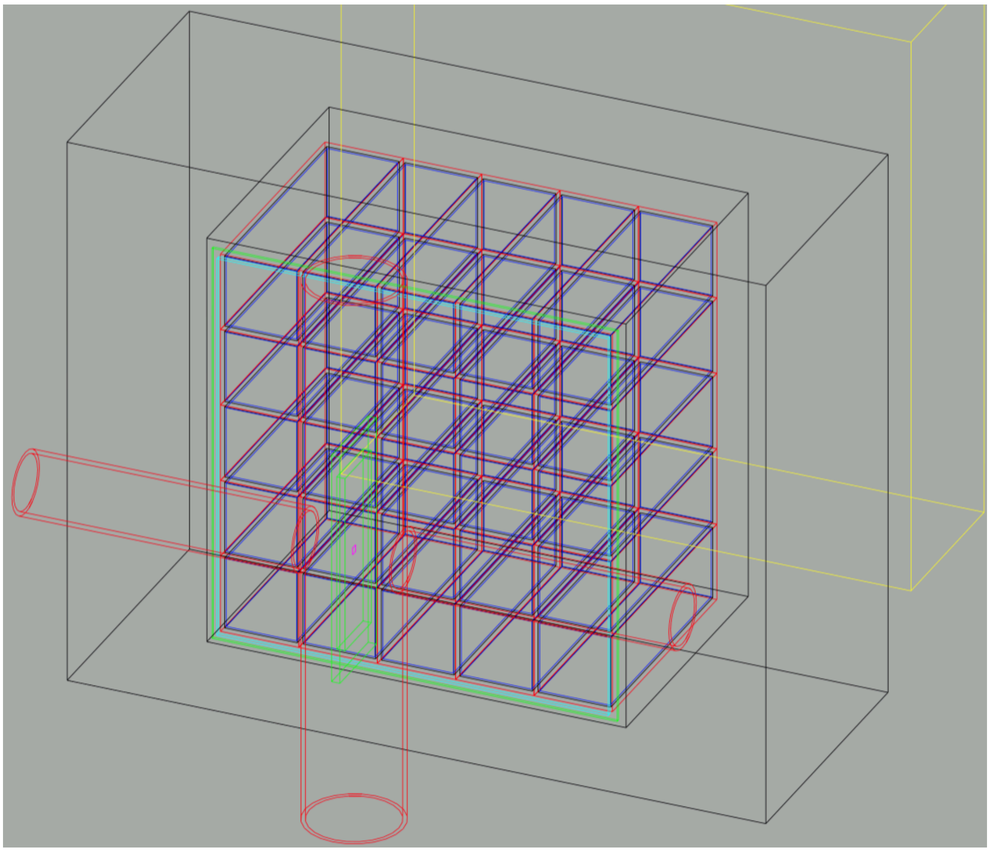

Figure 3.26: Geometrical setup in the simulation. Colors and material : blue = NaI, red = aluminum, black = lead, green = SUS, purple = target, light blue = plastic, yellow = CsI.

the data due to the dead time and pile-up of the γ-ray detector. Therefore, the MC was corrected (scaled down) by a correction factor (C_f) for each counter to reproduce the data by the relative ratio of the total number of events with energy higher than 1.5 MeV compared to that of data. The correction factor C_f is summarized in Tab.3.8. The mean value of 0.87 for C_f was derived and the systematic uncertainty of the detection efficiency was estimated to be 5 % from the standard deviation.

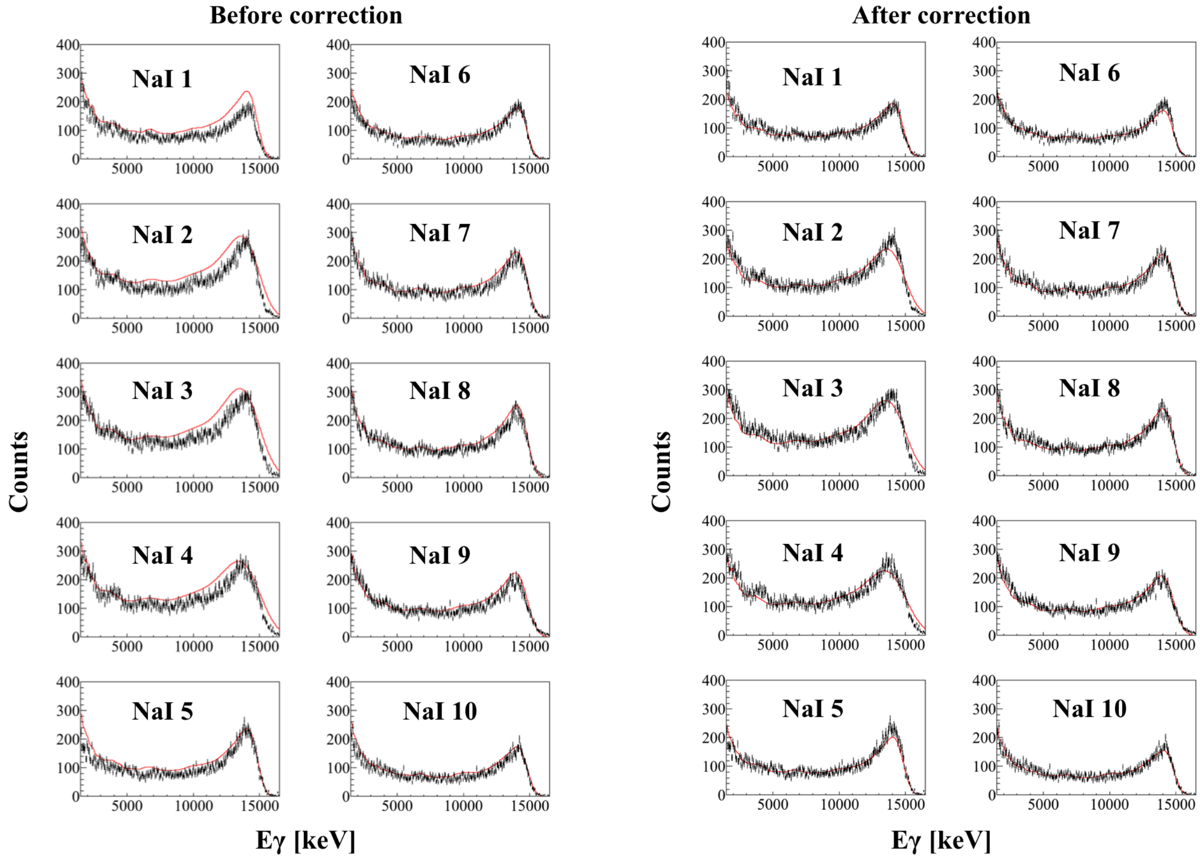

Figure 3.27: The energy spectrum from the ^{12}C state at E_x=15.11 MeV measured (black) and predicted by MC (red) for each counter before (left) and after (right) the correction to the MC.

Table 3.8: Correction factors (C_f) of MC spectra for 10 NaI counters.

Counter No.	Mf	Counter No.	Mf
1	0.78	6	0.91
2	0.82	7	0.93
3	0.85	8	0.93
4	0.85	9	0.93
5	0.85	10	0.90

Array energy spectrum comparison with data

In Fig.3.28, the array energy spectra in Fig.3.24 are also compared with corrected MC (just MC in further sentences) spectra after background subtraction. For 2.12-MeV γ ray, emission probability of 10% is assumed. MC reproduces both of the shape and the height (detection efficiency) very well.

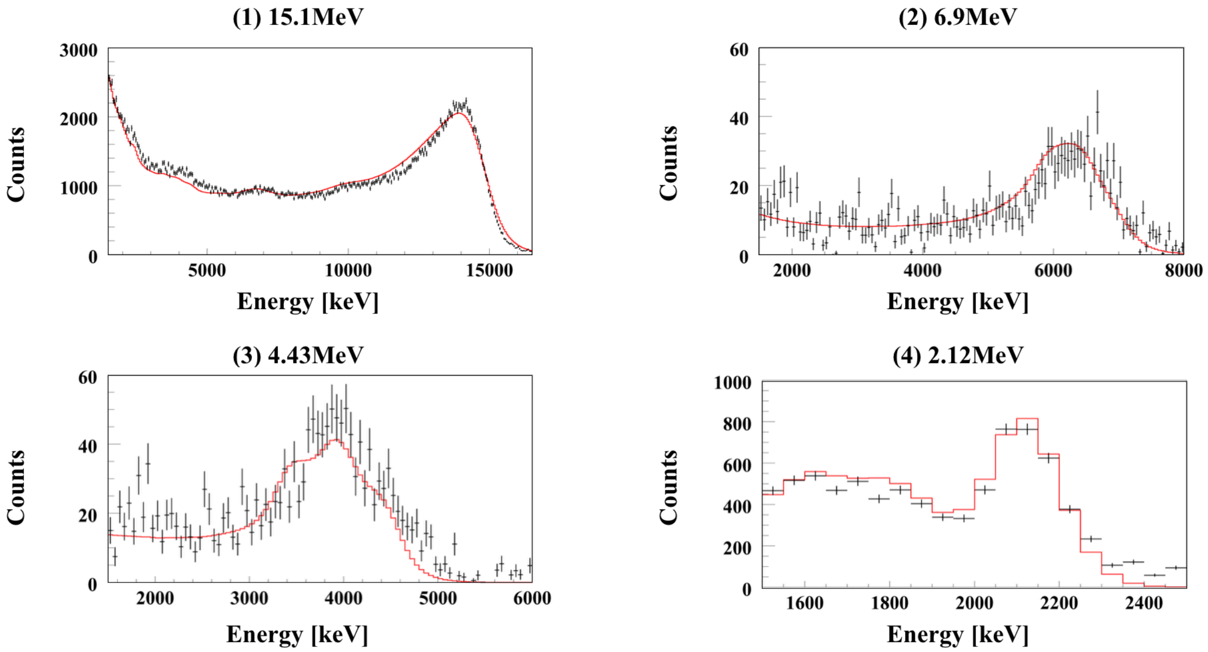

Figure 3.28: The array energy spectra from data (black point) and from corrected MC (red line). For 2.12-MeV γ ray, emission probability of 10% was assumed. Only the statistical uncertainty is shown for the data.

Detection efficiency

In Fig.3.29 the detection efficiency including solid angle $(\eta\epsilon)_{\gamma_{Data}}$ of the γ-ray detector using 10 NaI counters from the data is shown in black point together with that predicted by MC $(\eta\epsilon)_{\gamma_{MC}}$ in red line. A event with energy higher than the threshold of 1.5 MeV is defined as a detection. The difference between the data and MC is summarized in Tab.3.9. The larger error for 4.4-MeV γ ray is due to the systematic error of the emission probability (23 %) [40].

Table 3.9: Comparison of detection efficiency between data and MC.

E_γ [MeV]	$(\eta\epsilon)_\gamma$, Data/MC
4.4	1.22±0.28
6.9	0.99±0.04
15.1	1.00±0.03

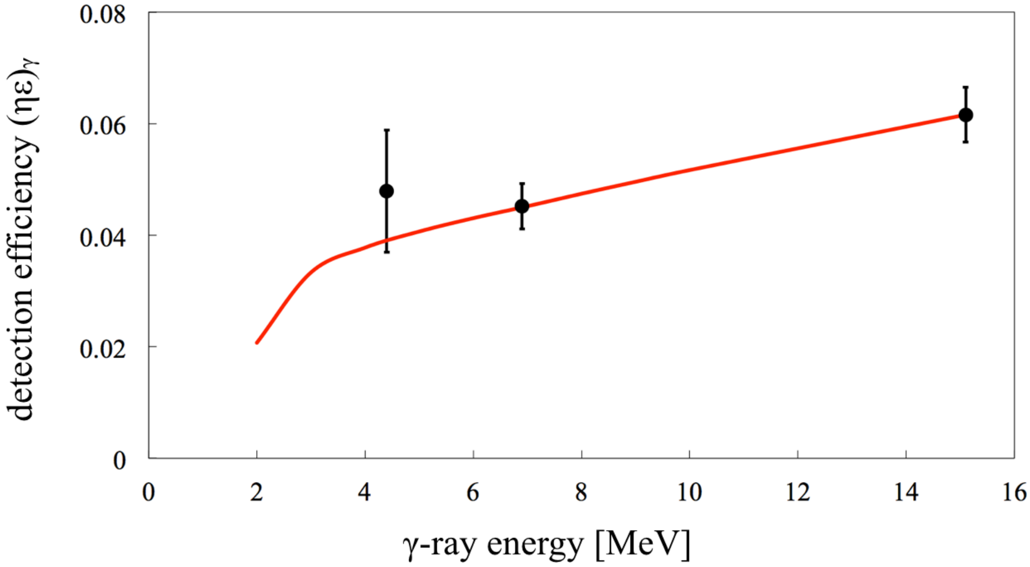

Figure 3.29: The detection efficiency including solid angle ($\eta\epsilon_\gamma$) for energy threshold of 1.5 MeV from data (black point) and from MC (red line)

Chapter 4

Experimental Results

4.1 Double differential cross section of (p,p') inelastic scattering reaction

Double differential cross sections of $^{12}\mathrm{C(p,p')}$ and $^{16}\mathrm{O(p,p')}$ reactions deduced by Eq.(4.1) are shown in the top and bottom panels of Fig.4.1, respectively. Only events with horizontal and vertical angles with $\theta_t < 0.5^\circ$ and $\phi_t < 2.5^\circ$ were used (see Sec.3.1.2). The notations of the variables are summarized in Table 4.1. In the hatched area of $^{16}\mathrm{O(p,p')}$, mean value is shown. The systematic uncertainties are summarized in Table 4.2. Giant resonances are clearly observed as broad peaks for 16 MeV$<E_x<$34 MeV.

$$\frac{d^2\sigma}{d\Omega dE} = CJ\frac{N_{E_x}}{\Omega}\frac{1}{L\eta\tau}\frac{e}{Q\epsilon}\frac{A}{N_A ta} \tag{4.1}$$

Table 4.1: Variables used for differential cross section.

variable	description	value	unit
$\frac{d^2\sigma}{d\Omega E}$	double differential cross section		[mb/sr·MeV]
C	unit conversion constant	10^{30}	[mb/cm^2·mg/g]
J	Jacobian	0.81 (^{12}C), 0.85(^{16}O)	[-]
N_{E_x}	number of events between E and $E+\Delta E$		[counts/MeV]
Ω	solid angle in laboratory frame		[sr]
L	DAQ live ratio		[-]
η	tracking efficiency	0.93	[-]
τ	trigger efficiency	0.978	[-]
e	elementary charge	1.6×10^{-19}	[C]
Q	total beam charge		[C]
ϵ	beam transmission ratio	1.0	[-]
A	target atomic wight		[g/mol]
N_A	Avogadro constant	6.02×10^{24}	[/mol]
t	target thickness		[mg/cm^2]
a	target enrichment		[−]

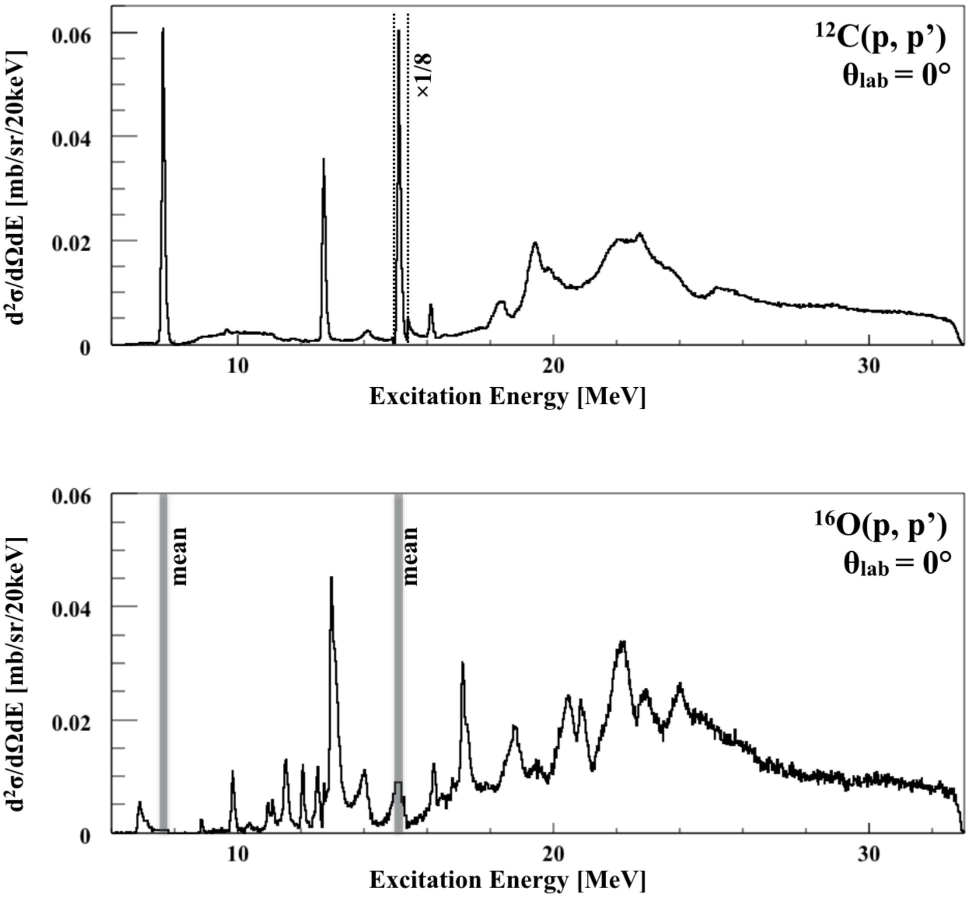

Figure 4.1: Double differential cross sections for ^{12}C(p, p$'$) reaction (top) and ^{16}O(p, p$'$) reactions (bottom).

Table 4.2: Systematic uncertainties

Description	variable	uncertainty	estimated by
solid angle	Ω	4%	sieve slit data
tracking efficiency	η	1%	energy dependence
total beam charge	Q	3%	BLP statistics and current offset
target thickness	t	2%	difference between runs
background subtraction	N_{E_x}	1%	shape of background spectrum
subtraction of ^{12}C data for ^{16}O	N_{E_x}	3%	subtraction factor
Total	-	6%	

4.1.1 Angular distribution of the cross section

Software angle cut

The angular resolution was dominated by the vertical angular resolution of $\Delta\phi_t = 0.7°$ compared to the horizontal angular resolution of $\Delta\phi_t = 0.12°$ (see Sec.3.1.2). In addition, the acceptance in vertical direction $0° < \phi_t < 3°$ was larger than that in horizontal direction $0° < \theta_t < 1°$. Therefore, software cuts to ϕ_t with 0.5° steps were applied in order to obtain the angular distribution (0°-0.5°, 0.5°-1.0°,..), while the angle cuts to θ_t were kept the same $(0.0° < \theta_t < 0.5°)$. The scattering angle $(\theta = \sqrt{\theta_t^2 + \phi_t^2})$ for each cut is plotted in Fig.4.2 for ^{12}C data.

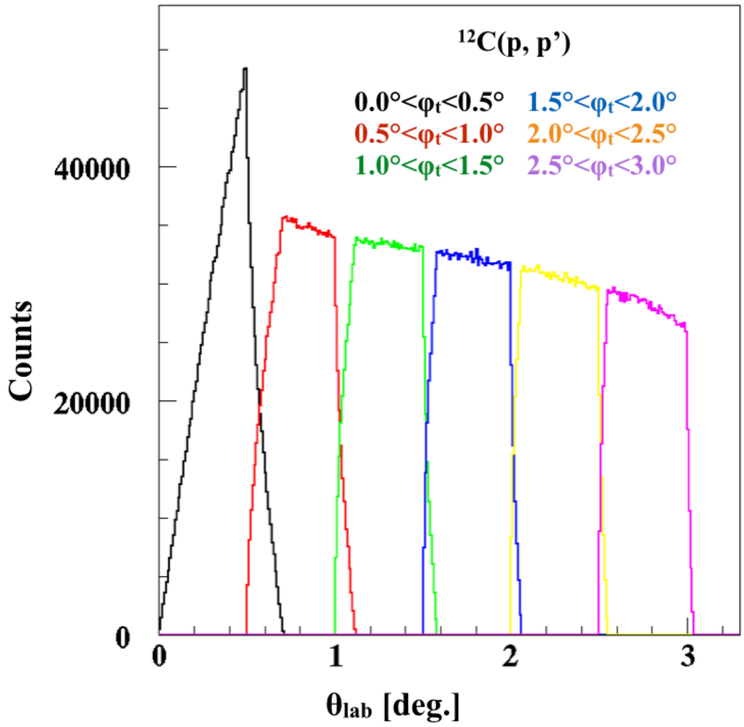

Figure 4.2: Scattering angle $(\theta = \sqrt{\theta_t^2 + \phi_t^2})$ distribution for each vertical angle (ϕ_t) cut with 0.5° steps. Horizontal angle (θ_t) cut was kept the same $(0.0° < \theta_t < 0.5°)$.

Angular distribution

Double differential cross sections $(d^2\sigma/d\Omega dE)$ with angle cuts of $0° < \phi_t < 0.5°$, $1.5° < \phi_t < 2.0°$ and $2.5° < \phi_t < 3.0°$ are plotted in Fig.4.3 for both ^{12}C (top panel) and ^{16}O (bottom panel) in giant resonances region. Since the Y_c was correlated to ϕ_t, the background subtraction method described in Sec.3.1.3 did not work. Therefore, an extended background subtraction method was applied to obtain the excitation energy spectrum with ϕ_t cut. The detail can be found in Ref.[42].

In Fig.4.3 angular dependences of the cross section are clearly observed. For example, the cross section of ^{12}C at E_x ~18.4 MeV increases as the scattering angle, while that at E_x ~22.5

MeV decreases as the scattering angle.

Angular distribution of the differential cross section ($d\sigma/d\Omega$) for discrete states and giant resonances of ^{12}C and ^{16}O are shown in Fig.4.4 and Fig.4.5, respectively, and are discussed in Sec.5.1.3.

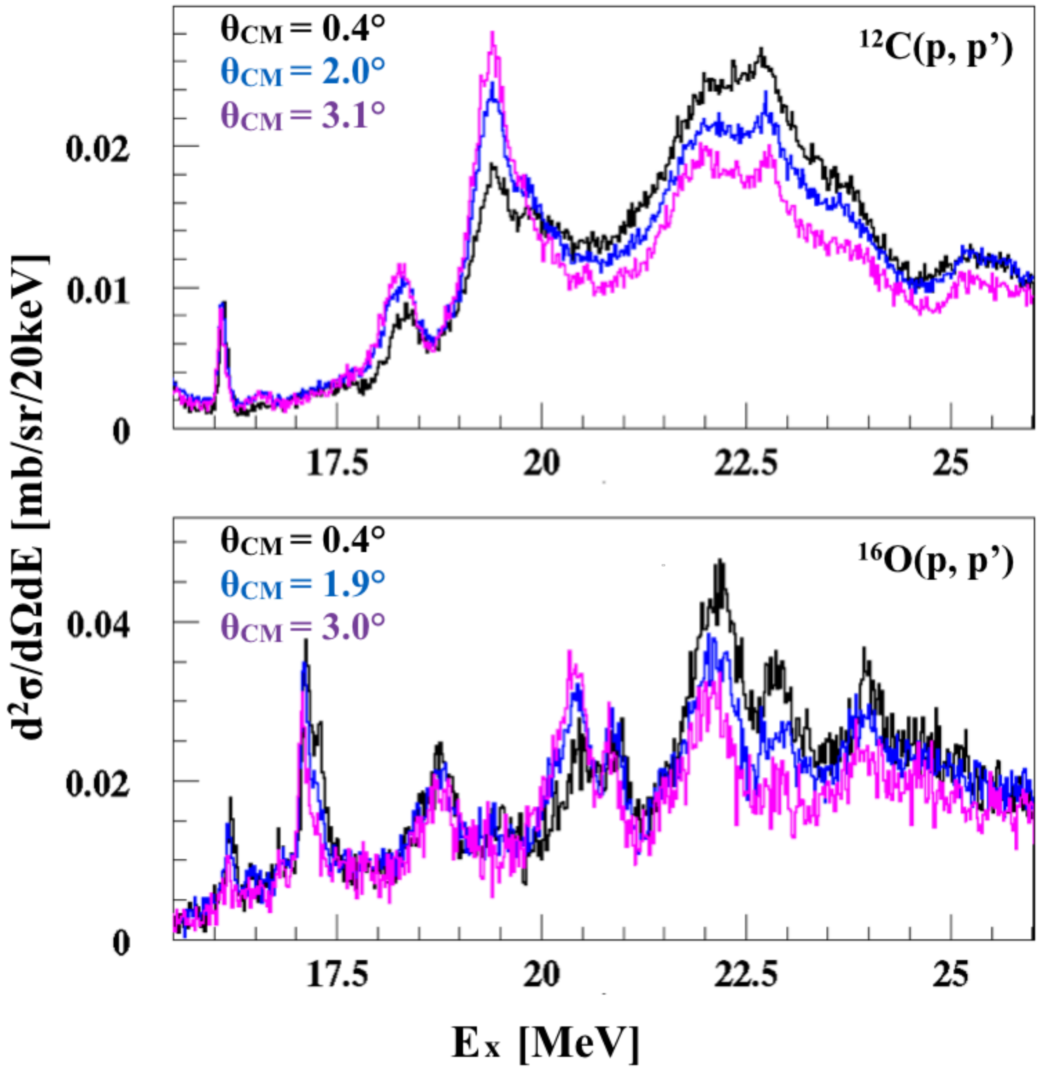

Figure 4.3: Double differential cross sections with angle cuts of 0° $< \phi_t <$ 0.5° (black), 1.5° $< \phi_t <$ 2.0° (blue) and 2.5° $< \phi_t <$ 3.0° (purple) for ^{12}C (top) and ^{16}O (bottom). The mean scattering angles in the center of mass frame are written.

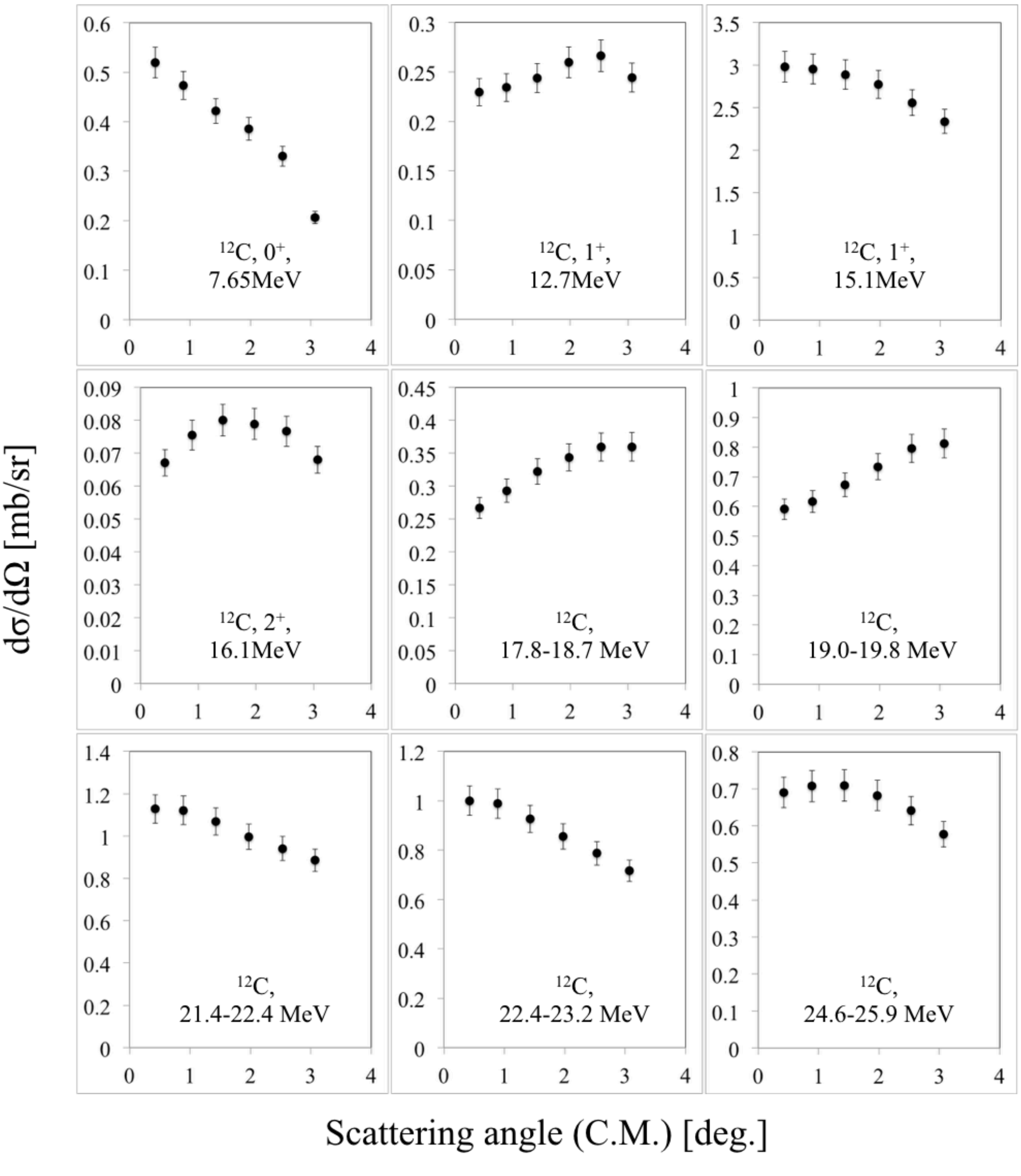

Figure 4.4: Angular distribution of ^{12}C states. The spin-parities (J^π) for the discrete states are taken from Table of Isotopes [8].

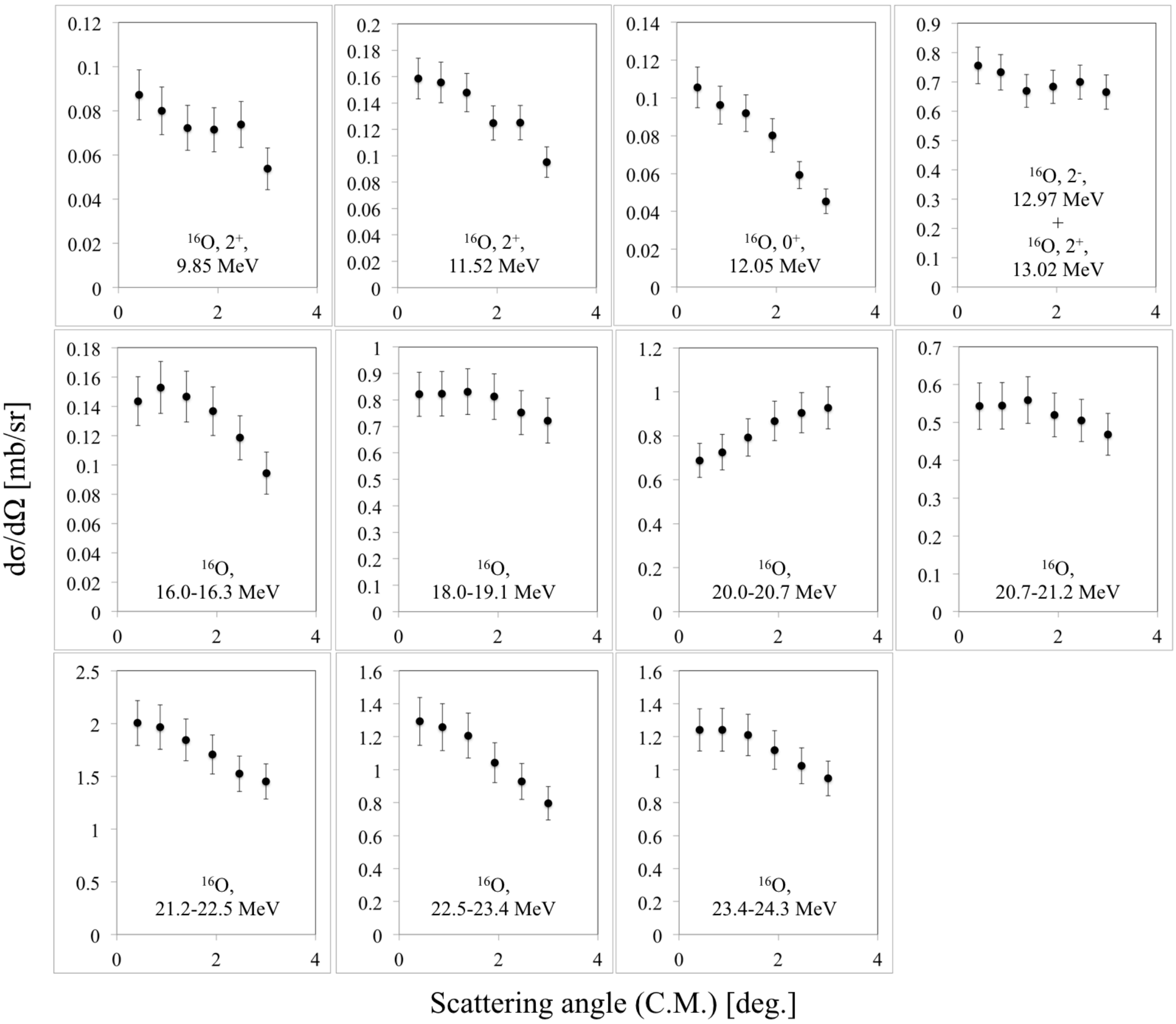

Figure 4.5: Angular distribution of ^{16}O states. The spin-parities (J^π) for the discrete states are taken from Table of Isotopes [8].

4.2 γ-rays from giant resonances

Figures 4.6-4.8 show the coincidence γ-ray energy spectra (black) of ^{12}C in the excitation energy from 16 MeV to 34 MeV with 2 MeV steps along with the background spectra (red). The same figures for ^{16}O are shown in Figs.4.9-4.11. All the runs with a beam intensity of 0.5 nA were used and no angle cut was applied. Number of excitation events (N_{E_x}) measured by the spectrometer are summarized in Tab.4.3 for each E_x range.

Table 4.3: Number of excitation events (N_{E_x}) for each E_x range.

E_x range in MeV	N_{E_x} of ^{12}C	N_{E_x} of ^{16}O	uncertainty
16-18	665973	511979	1.2%
18-20	2841454	629864	0.27%
20-22	3189985	1034694	0.61%
22-24	4077565	1207809	0.58%
24-26	2404901	966138	0.59%
26-28	1892386	624724	0.67%
28-30	1749792	518630	1.2%
30-32	1614982	506396	3.6%
32-34	719116	235346	13%

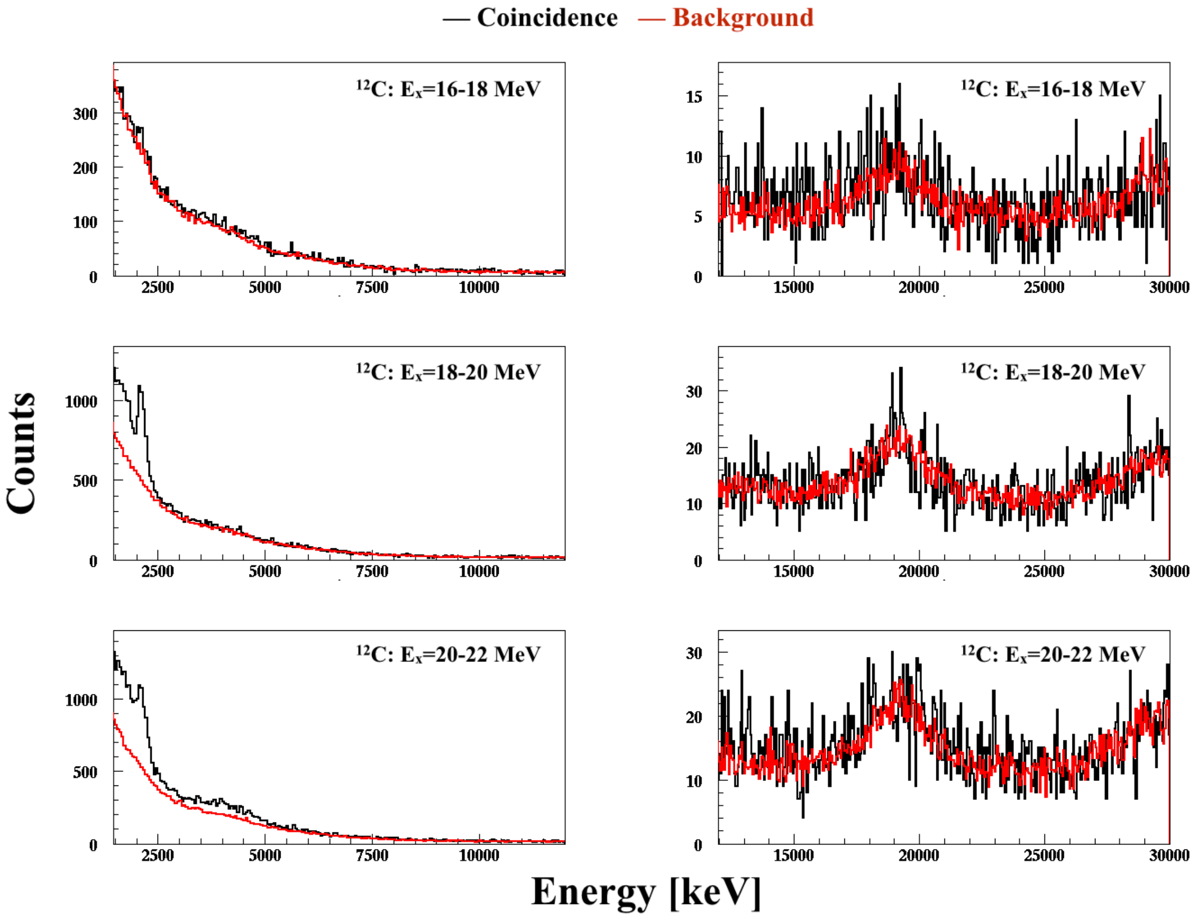

Figure 4.6: Coincidence γ-ray spectra (black) and background spectra (red) from giant resonances of ^{12}C at $E_x = 16 \sim 22$ MeV with 2 MeV steps.

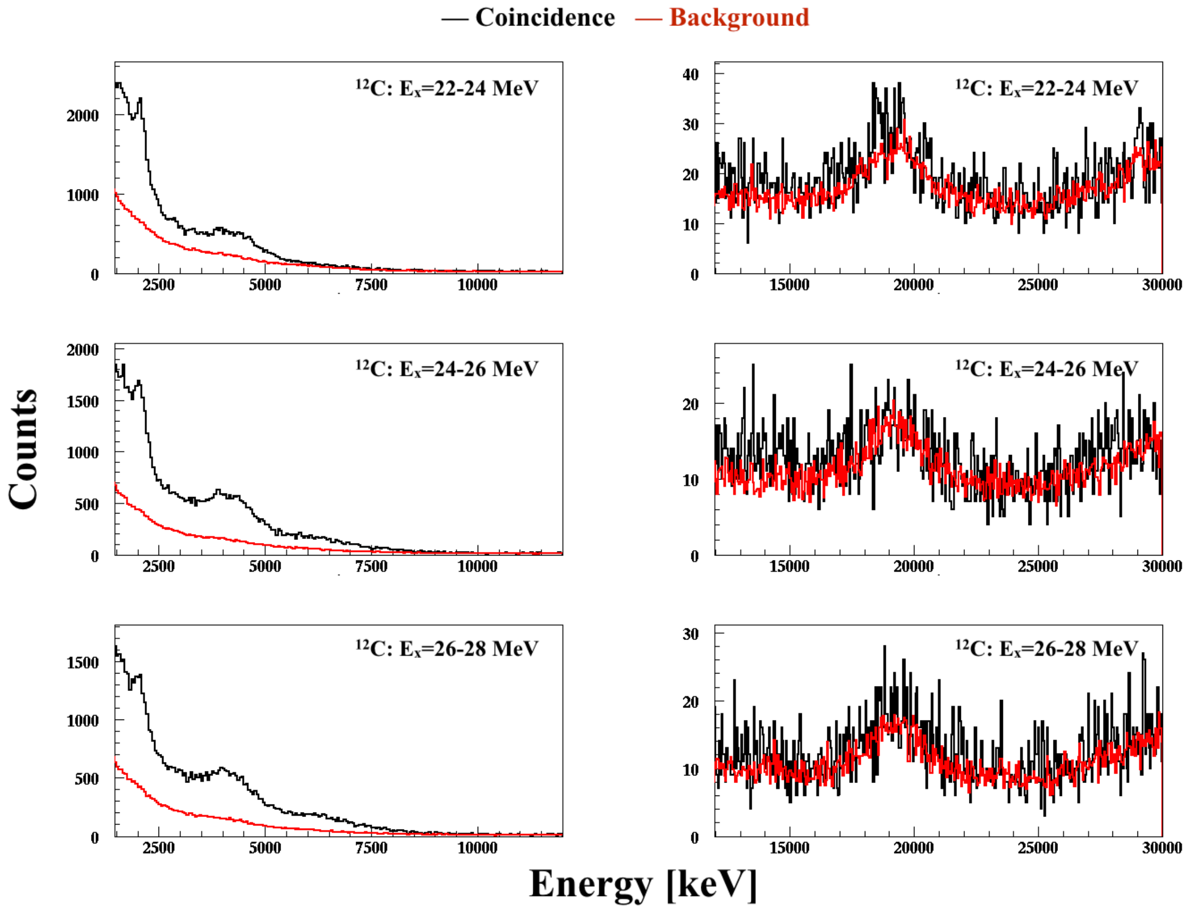

Figure 4.7: Same as Fig.4.6 but for ^{12}C at $E_x = 22 \sim 28$ MeV.

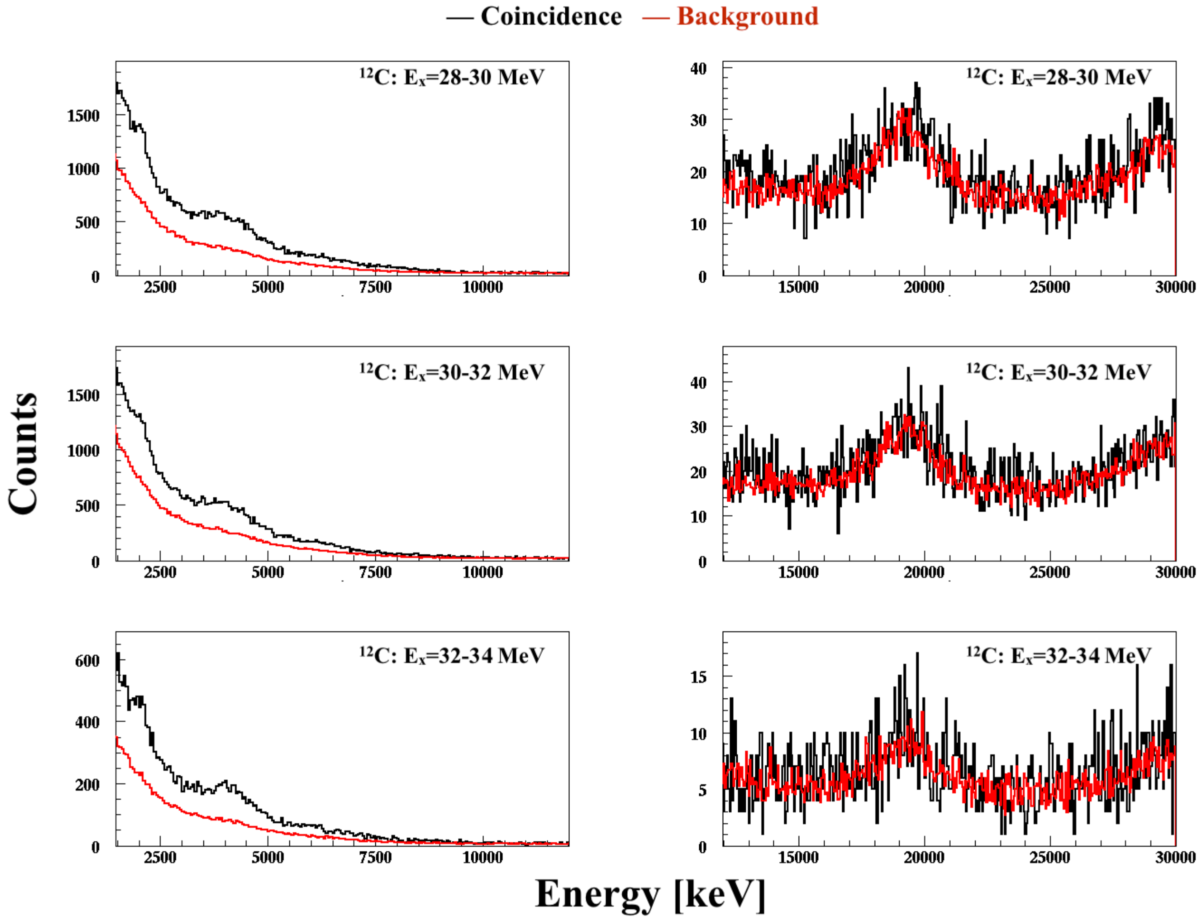

Figure 4.8: Same as Fig.4.6 but for ^{12}C at $E_x = 28 \sim 34$ MeV.

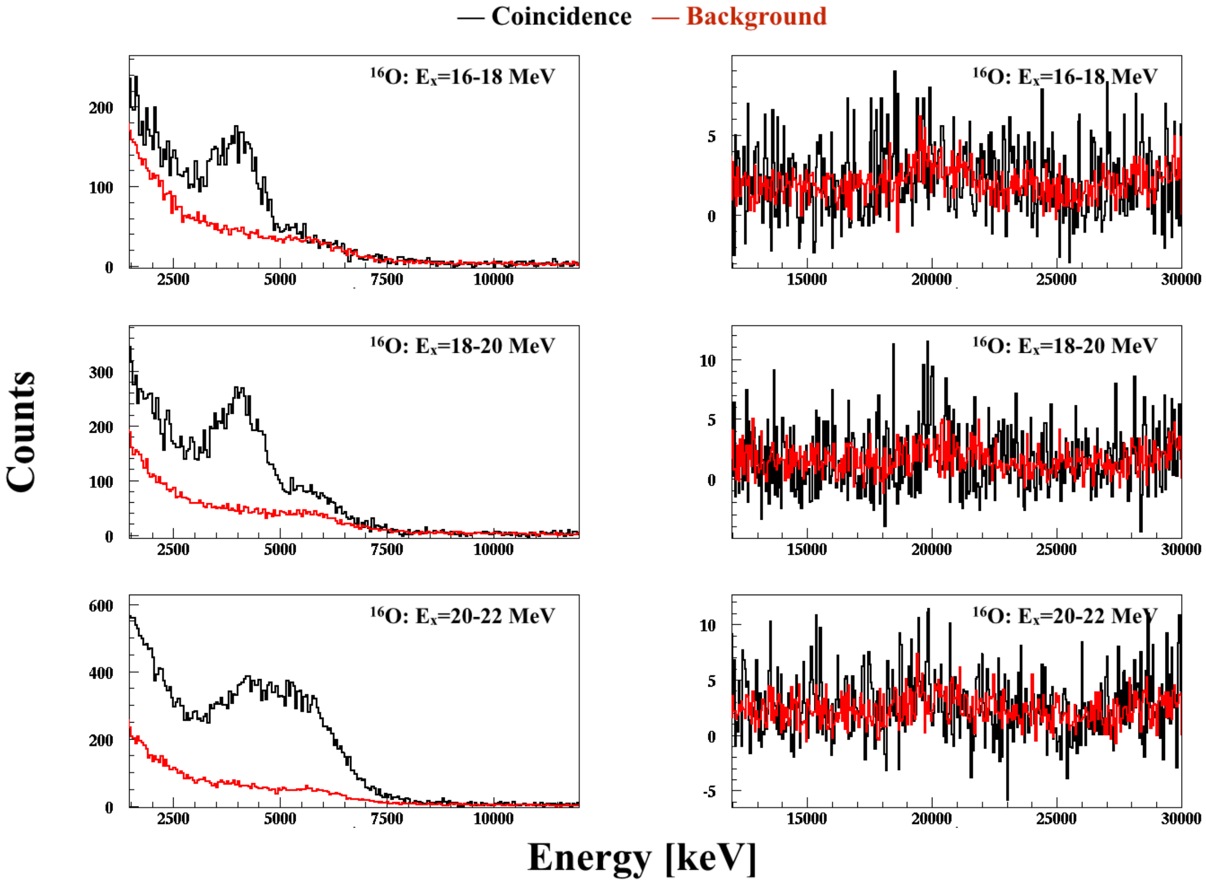

Figure 4.9: Same as Fig.4.6 but for ^{16}O at $E_x = 16 \sim 22$ MeV.

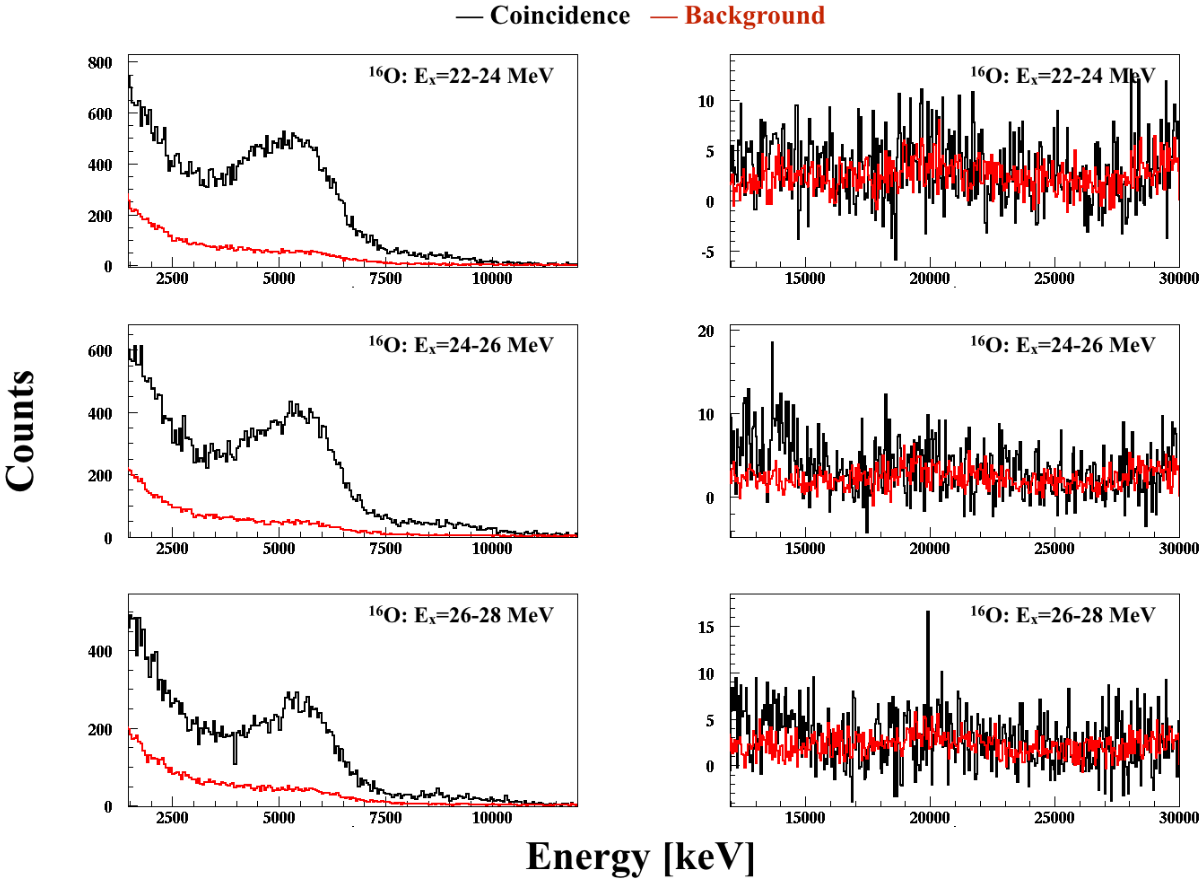

Figure 4.10: Same as Fig.4.6 but for ^{16}O at $E_x = 22 \sim 28$ MeV.

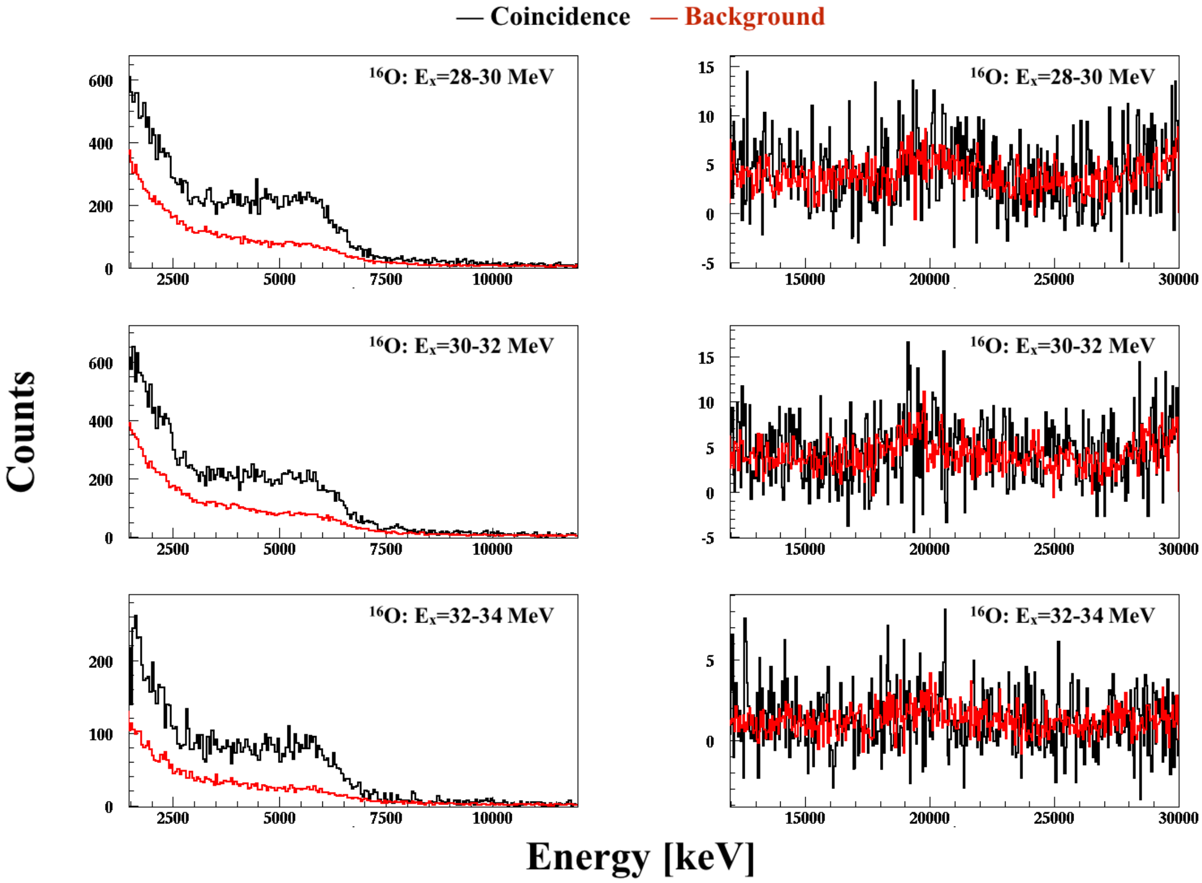

Figure 4.11: Same as Fig.4.6 but for ^{16}O at $E_x = 28 \sim 34$ MeV.

Chapter 5

Discussion

5.1 (p, p') inelastic scattering

5.1.1 Comparison of (p, p') inelastic scattering cross section and photoabsorption cross section

Inelastic proton scattering can excite the target nucleus by both electromagnetic interaction (Coulomb force), which gives mainly dipole E1 transition, and strong interaction (nuclear force). At angles smaller than a grazing angle, where the projectile touches the surface of the nucleus, Coulomb excitation dominates the cross section. The cross sections induced by Coulomb force, nuclear force (free nucleon-nucleon interaction) and the sum of NN and Coulomb including their interference predicted by DWBA calculation are shown in Fig.5.1 (see Sec.5.1.3 for DWBA in detail). At small scattering angles ($\theta < 3^\circ$) the cross section is dominated by the Coulomb interaction.

The proton inelastic scattering cross section induced by Coulomb force (σ_{C}) can be calculated by photoabsorption cross section (σ_γ) using virtual photon method. Since the target is excited in a divergence-free field ($\nabla \cdot E = 0$), Coulomb excitation and photoabsorption reactions involve the same transverse matrix elements [43]. Photoabsoprtion cross section of ^{12}C and ^{16}O are shown in Fig.5.2 [44].

Comparison of (p, p') cross section at very forward scattering angle and photoabsorption cross section has been applied to heavy nuclei such as ^{120}Sn [45] and ^{208}Pb [46] and good agreements were obtained. However, there has been no comparison for the case of light nuclei such as ^{12}C and ^{16}O.

Virtual photon method

From Eq.(11) of Bertulani and Nathan [43], one gets the conversion formula from σ_γ into σ_{C} as

$$\frac{d^2\sigma_C}{d\Omega dE_\gamma} = \frac{1}{E_\gamma} \sum_{\pi l} \frac{dn_{\pi l}}{d\Omega} \sigma_\gamma^{\pi l}, \tag{5.1}$$

where Ω is the solid angle, E_γ is the energy of the photon and π and l denote multipolarity (l and m) for the electric ($\pi = E$) and the magnetic ($\pi = M$) excitaions. n is the virtual photon

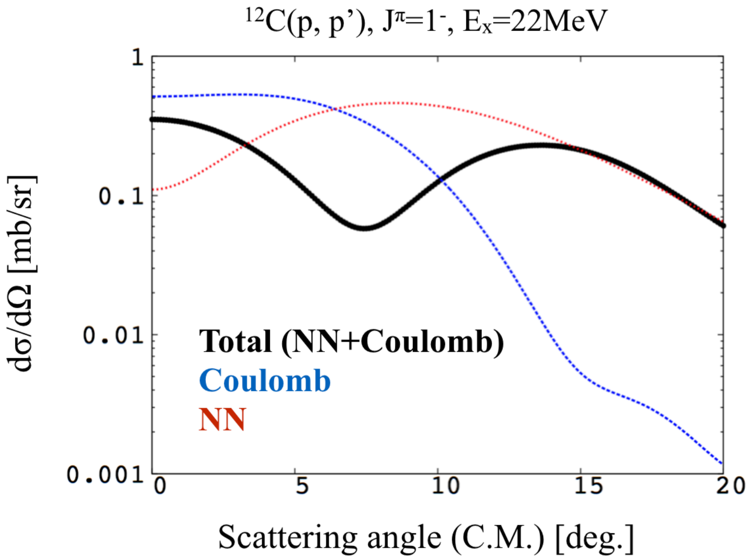

Figure 5.1: The cross section induced by Coulomb force (Coulomb), nuclear force (free nucleon-nucleon interaction, NN) and sum of NN and Coulomb including their interference predicted by the DWBA calculation.

number calculated by eikonal approximation relativistically as

$$\frac{dn_{\pi l}}{d\Omega} = Z_1^2\alpha(\frac{\omega k}{\gamma v})^2\frac{l\ [(2l+1)!!]^2}{(2\pi)^3(l+1)}\sum_m |G_{\pi lm}|^2|\Omega_m(q)|^2 \tag{5.2}$$

where Z_1 is the charge of the projectile, α is the fine-structure constant, m denotes multipolarity, $G_{\pi lm}$ is the Winther-Alder relativistic function and q is the momentum transfer.

Comparison of (p, p') cross section and photoabsorption cross section

The measured (p, p') cross section cannot be directly compared to the photoabsorption cross section, since the former has both spin-flip and non-spin-flip excitations while the latter is dominated by non-spin-flip excitation. Therefore, the non-spin-flip ratio of (p, p') reaction at scattering angle around 0° was taken from previous experiments [47, 38], and multiplied to the measured (p, p') cross section to extract the non-spin-flip cross section. A software angle cut of $\theta < 0.5°$ was applied since the grazing angle (θ_{gr}) is calculated from Eq.(1.14) of Feshbach [48] to be 0.85° for ^{12}C and 1.03° for ^{16}O. In Fig.5.3, the experimental non-spin-flip cross sections of ^{12}C and ^{16}O are compared with the Coulomb excitation cross sections calculated by virtual photon method. Although there remains the systematic uncertainty of non-spin-flip ratio, the two cross sections agree well with each other for both ^{12}C and ^{16}O without any normalization. This implies that the non-spin flip cross section, which is about 60% of the total cross section at E_x >20MeV, is dominated by the Coulomb interaction, thus, iso-vector giant dipole resonances with ΔL=1, ΔT=1 and ΔS=0.

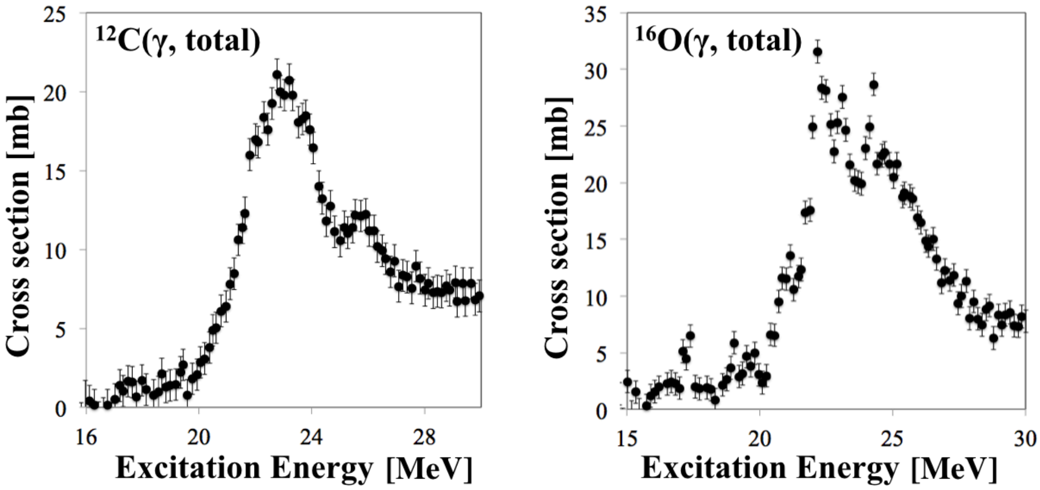

Figure 5.2: Photoabsoprtion cross section of ^{12}C (left) and ^{16}O (right) [44].

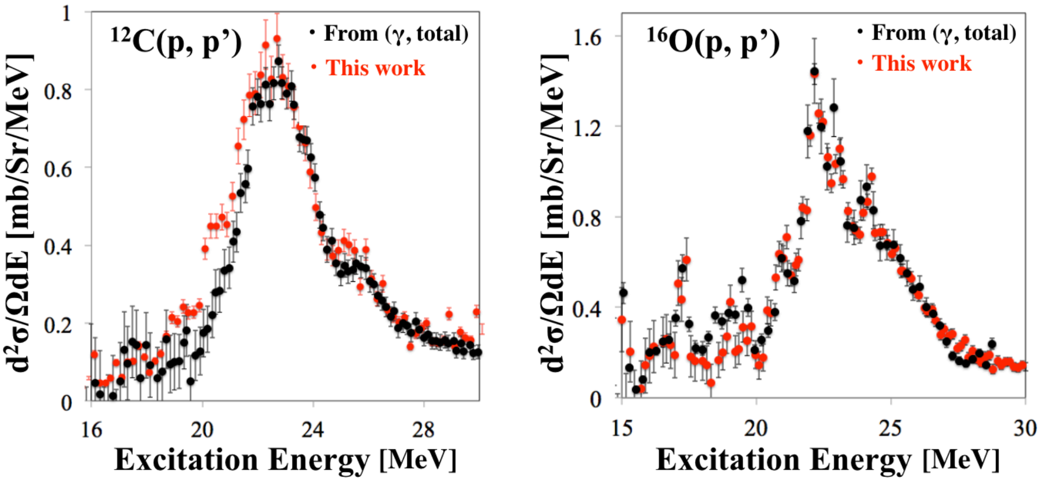

Figure 5.3: The cross section comparison of (p,p') non-spin-flip excitaion (black) and the Coulomb excitation calculated by virtual photon method (red).

5.1.2 Giant resonances populated by (p, p') inelastic scattering

As mentioned in Sec.1.1.3, the giant resonance can be classified by the quantum numbers of each collective mode; multipolarity (L), Spin (S) and isospin (T). The characteristics of the giant resonances observed in the experiment have been well studied by previous experiments using polarization transfer observables (Σ) [47, 38]. The cross sections shown in Fig,4.1 agree well with their results. The giant resonances above 20 MeV are reported to be dominated by ΔL=1 and ΔT=1 transition. On the other hand, the spin transfer (ΔS) can vary depending on the scattering angle (θ).

The cross section and polarization transfer variables in the $^{16}\mathrm{O}(\mathrm{p},\mathrm{p}')$ reaction at 392 MeV were measured between $\theta = 0°$ and $\theta = 14°$ by Kawabata *et al*. Their results at $\theta = 0°$ and $\theta = 4°$ are shown in Fig.5.4 [49]. The previous result suggests that the cross section is dominated by GDR at $\theta = 0°$ and by SDR at $\theta = 4°$. The same feature is expected for ^{12}C and has been reported by the random phase approximation calculation [50]. Since the J^π of the ground states of both ^{12}C and ^{16}O is 0^+, J^π of GDR is 1^-, while J^π of SDR can be 2^-,1^- and 0^-.

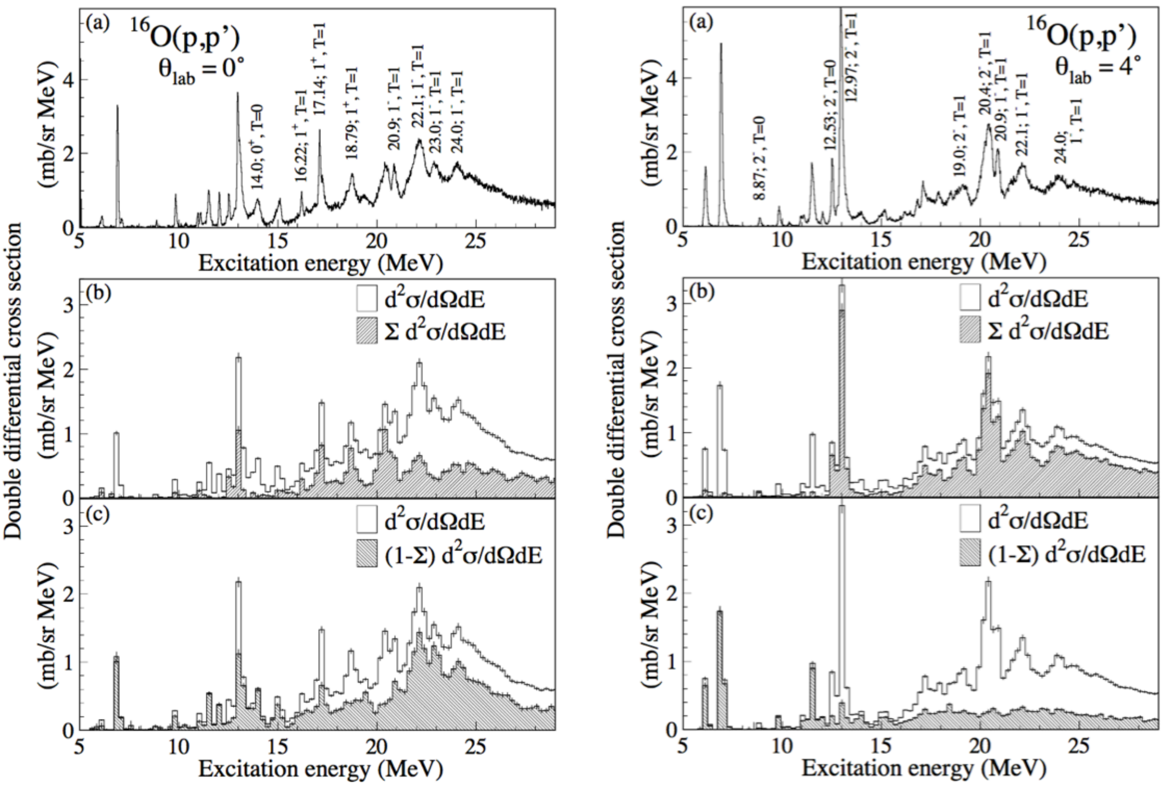

Figure 5.4: Double differential cross sections for $^{16}\mathrm{O}(\mathrm{p},\mathrm{p}')$ reaction at θ=0° (left) and at θ=4° (right) taken from Kawabata *et al* [49]. (a) Total cross section. (b) Total cross section $d^2\sigma/d\Omega dE$ and spin-flip component $\Sigma d^2\sigma/d\Omega dE$. (c) Total cross section $d^2\sigma/d\Omega dE$ and non-spin-flip component $(1-\Sigma)d^2\sigma/d\Omega dE$.

5.1.3 Distorted wave Born approximation

The measured angular distributions of ^{12}C(p, p$'$) cross section shown in Fig.4.4 have been compared to the predictions by the distorted wave Born approximation (DWBA) calculation. DWBA calculation has been performed by a program code DWBA07 [51]. Distorted wave is derived by the global optical potential [5], which reproduces the proton elastic scattering cross section in the same energy region as shown Fig.1.3. The effective nucleon-nucleon scattering is taken from the T-matrix of the free nucleon-nucleon interaction at 425 MeV parametrized by Franey and Love [52].

Discrete states

The 0^+ state at 12.71 MeV and the 1^+ at 15.11 MeV are compared with DWBA calculation in Fig.5.5. The target wave functions are taken from Cohen and Kurath [53] and the DWBA calculation is scaled by 1.5. The shape of the angular distribution is well reproduced by the DWBA calculation for both states.

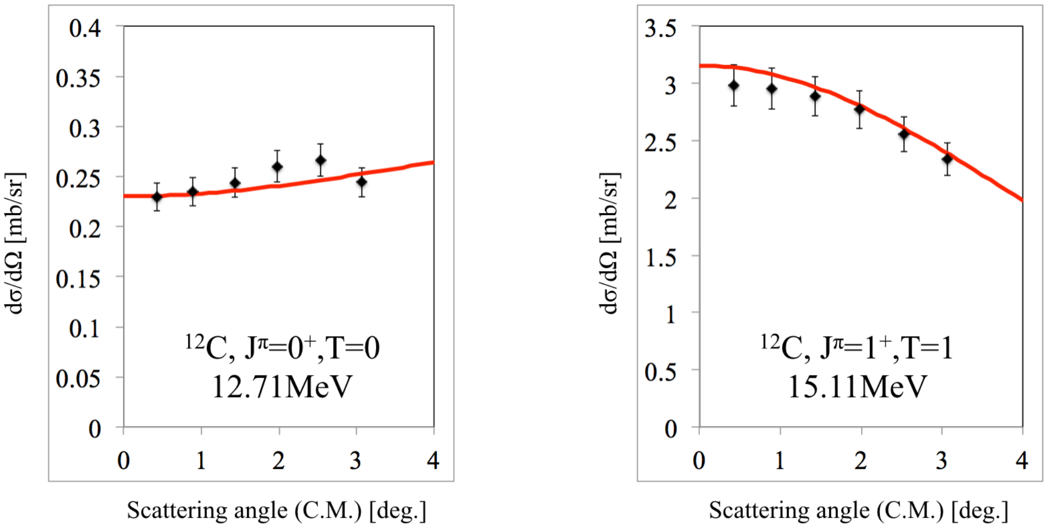

Figure 5.5: Measured differential cross sections (black point) for the 0^+ state at 12.71 MeV (left) and the 1^+ state at 15.11 MeV (right), and predictions by DWBA calculation (red line) using the Franey Love interaction [52].

Giant resonances

The DWBA calculations for GDR of ^{12}C with $J^\pi = 1^-$ and SDR with $J^\pi = 0^-$, 1^- and 2^- at 22 MeV are shown in Fig.5.6. Since a giant resonance is a collective motion of many particle systems, the calculation of the wave function is relatively difficult as compared to the discrete states which are usually assumed to be single particle-hole excitations. Therefore, the wave functions were derived by a program code NORMOD[54], which calculates the wave function so that the matrix element exhausts the sum rule for a given multipolarity.

The DWBA calculations for different J^π states are shown in Fig.5.6. The predictions were normalized at 0°, so only the shapes should compared. In $E_x > 21$ MeV, the shape of the cross section shown in Fig.4.4 agree swith that of GDR 1^- by DWBA calculation, which also supports the discussions in Sec.5.1.1-5.1.2.

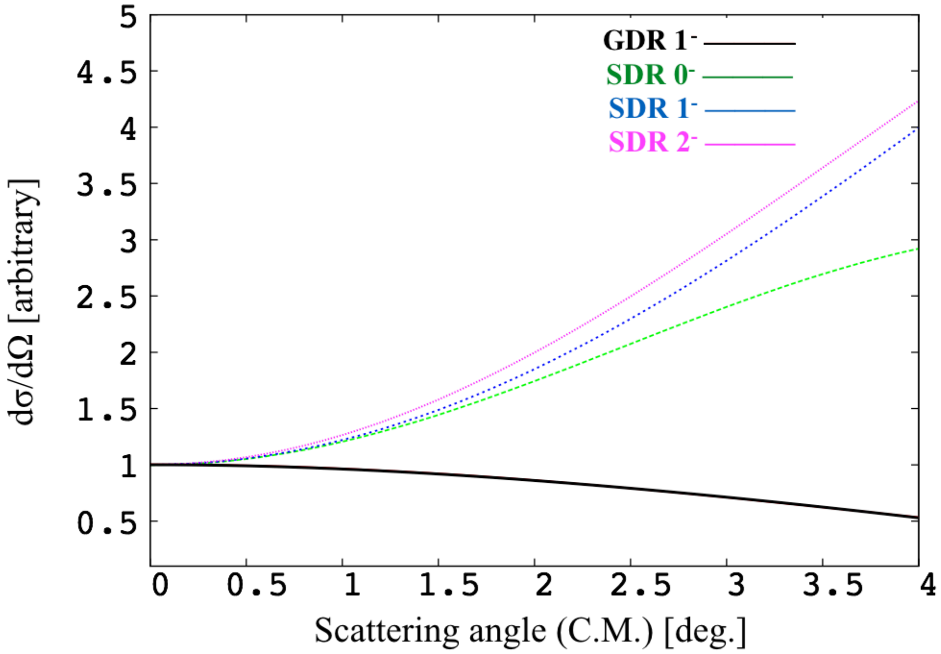

Figure 5.6: DWBA calculations of ^{12}C(p, p$'$) for GDR with $J^\pi = 1^-$ (black line) and SDR with $J^\pi = 0^-$ (green dotted line), 1^- (blue dotted line) and 2^- (purple dotted line) at E_x =22 MeV.

5.2 γ rays from giant resonances of ^{12}C

Spectrum fitting and emission probability

The γ-ray emission probability (Γ_γ/Γ) can be obtained for each E_x step by

$$\frac{\Gamma_\gamma}{\Gamma} = \frac{N_{E_\gamma}}{N_{E_x}} \frac{1}{(\eta\epsilon)_\gamma}, \tag{5.3}$$

where N_{E_γ} is the number of γ counts with energy higher than the threshold of 1.5 MeV, N_{E_x} is the excitation counts taken from Tab.4.3 and $(\eta\epsilon)_\gamma$ is the detection efficiency of the γ-ray detector.

Since the detection efficiency depends on the γ-ray energy as shown in Fig.3.29, the obtained spectra was decomposed into partial spectra of γ-ray candidates predicted by MC. γ-ray candidates were chosen from the level information of daughter nuclei for each E_x region [8].Figures 5.7-5.8 show the measured spectra after the background subtraction (black line) and decomposed γ-ray spectra (colored dotted line) and the sum of them (red line).

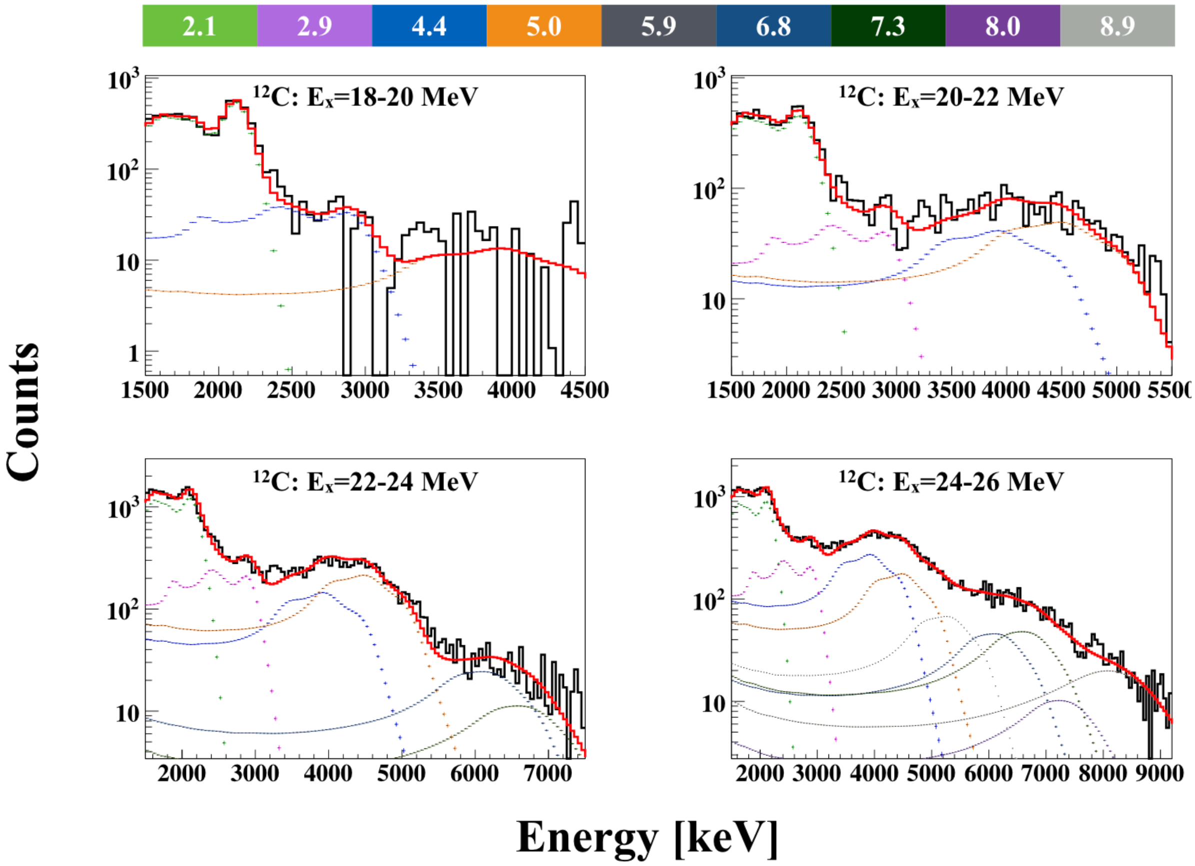

Figure 5.7: Measured γ-ray spectra (black line), decomposed partial γ-ray spectra (colored dotted line) predicted by MC and the sum of them (red line) for ^{12}C at $E_x = 18 \sim 26$ MeV with 2 MeV steps. The colors and enegies of decomposed partial γ-ray spectra are shown on top.

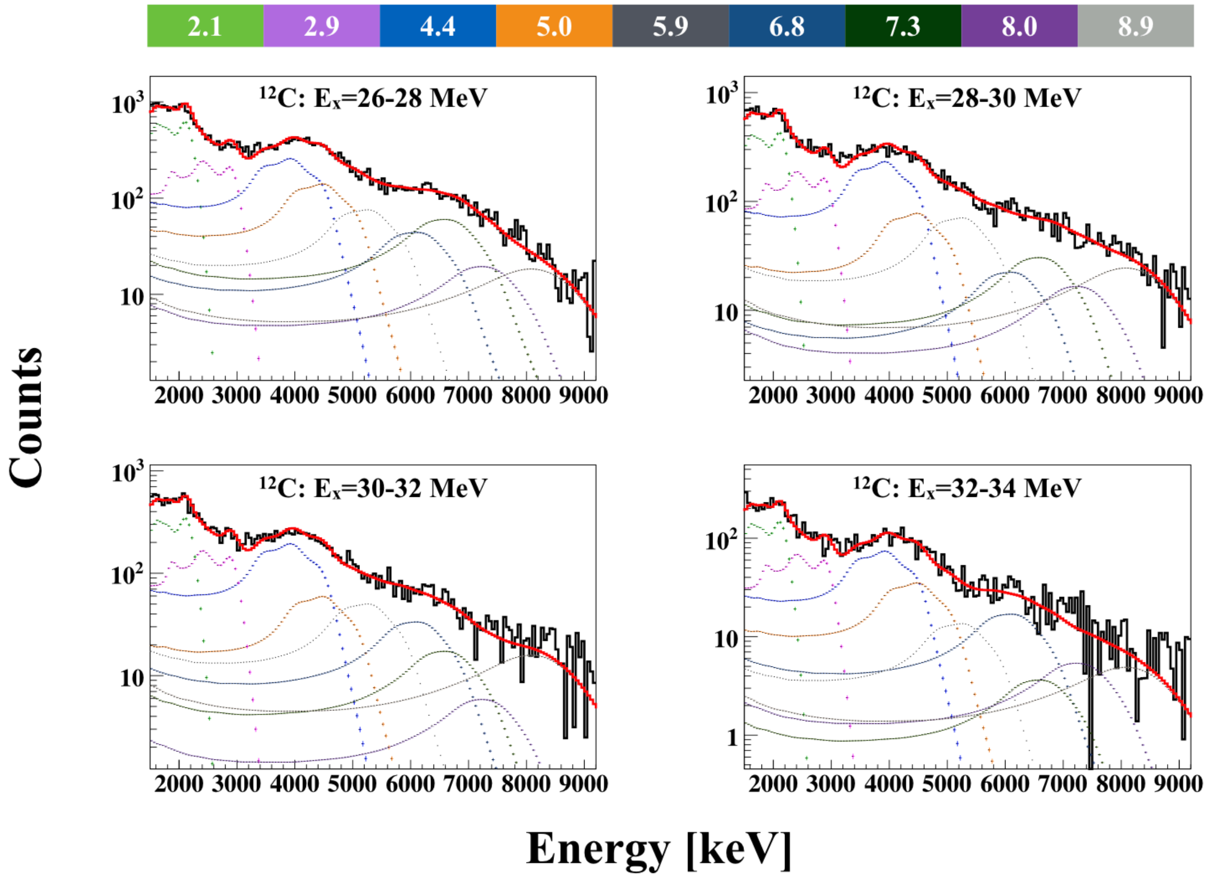

Figure 5.8: Same as Fig.5.7, but for ^{12}C at $E_x = 26 \sim 34$ MeV.

Then the γ-ray emission probability was obtained by

$$\frac{\Gamma_\gamma}{\Gamma} = \sum_i \frac{N_{E_\gamma,i}}{N_{E_x}} \frac{1}{(\eta\epsilon)_{\gamma,i}}, \tag{5.4}$$

where i stands for the number of γ-ray candidates.

Γ_γ/Γ of ^{12}C is shown in Fig.5.9 and summarized in Tab.A.1. The systematic uncertainty is given by

$$\frac{\Delta\Gamma_\gamma/\Gamma}{\Gamma_\gamma/\Gamma} = \sqrt{(\frac{\Delta N_{E_\gamma}}{N_{E_\gamma}})^2 + (\frac{\Delta N_{E_x}}{N_{E_x}})^2 + (\frac{\Delta(\eta\epsilon)_\gamma}{(\eta\epsilon)_\gamma})^2}, \tag{5.5}$$

which is dominated by the systematic uncertainty of the detection efficiency (5%) and the spectrum fitting (~2-10% depending on E_x region). The statistical uncertainty is 10 times smaller than systematic uncertainty and not shown in the figure. The emission probability increases as the excitation energy increases until the separation energy for multi-nucleon decay threshold (S_{2p}=27.19MeV for ^{12}C), and then decreases gradually.

Emission mechanism

The γ-ray energy spectra from the giant resonances of ^{12}C are shown in Figs.4.6-4.8. For 16 MeV $< E_x <$ 18 MeV, the measured γ-ray spectrum is consistent with the background spectrum, that is, no γ ray is emitted. On the other hand, for 18 MeV $< E_x <$ 20.4 MeV, a clear γ-ray signal is observed at around 2.1 MeV, which is the γ ray emitted from the first excited state of ^{11}B by proton emission. This can be easily understood by the energy conservation that ^{12}C must have at least $E_x = S_p$ + 2.12 = 18.08 MeV in order to decay to the first excited state of ^{11}B.

The same feature is seen in the energy spectrum for 20 MeV $< E_x <$ 22 MeV, where 4.44-MeV and 5.02-MeV γ rays emitted from the second and the third excited states of ^{11}B are observed in addition to the dominant 2 MeV γ ray. In this E_x range, the 2.00-MeV γ ray from the first excited state of ^{11}C after the neutron emission has also to be taken into account since the energy threshold is $E_x = S_n$ + 2.00 = 20.72 MeV.

As E_x increases many other channels open and higher energy γ rays are seen. But, no γ rays are clearly observed in $E_\gamma >$9 MeV. This is due to the fact that the separation energies of an α particle from ^{11}B and ^{11}C are 8.66 MeV and 7.54 MeV, therefore, even ^{12}C decays to the excited state of daughter nuclei with $E_x >$ 25 MeV, no γ ray but an α particle is emitted. In addition, this also shows that the direct γ decay to the lower states or the ground state of ^{12}C followed by high energy γ-ray emission has a very small probability compared to hadronic decays.

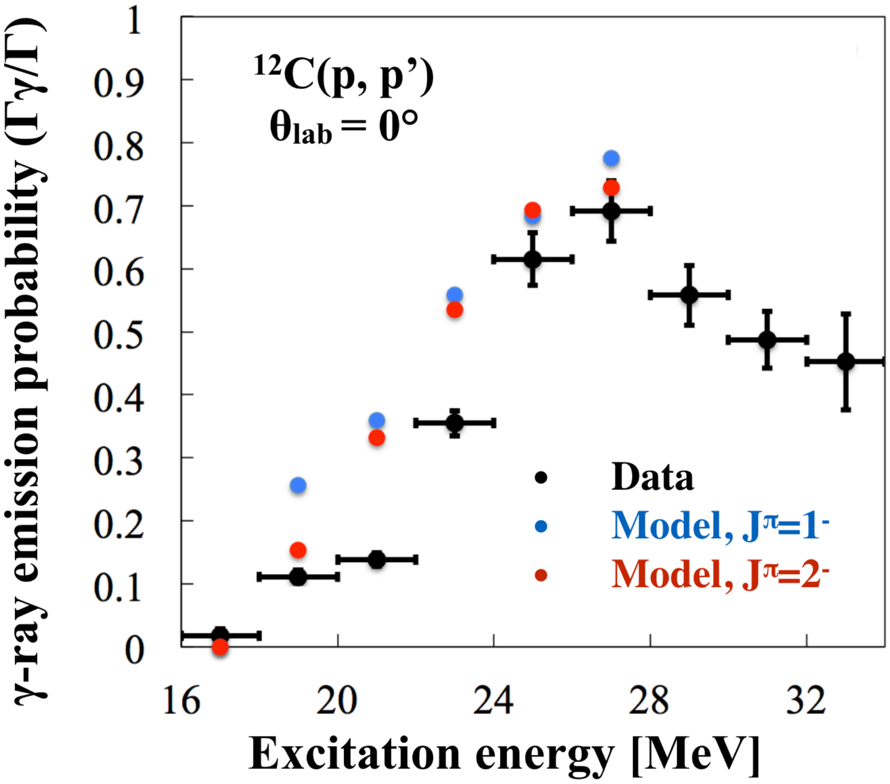

Figure 5.9: The γ-ray emission probability from giant resonances of ^{12}C. Black point is the data with statistical and systematic uncertainties. Blue and red points are the predictions by decay model for (J^{π}, T)=$(1^{-}, 1)$ and (J^{π}, T)=$(2^{-}, 1)$ states, respectively.

5.2.1 Comparison with decay model calculation.

Decay model calculation as described in Sec.1.1.4 has been performed for ^{12}C until the multi-nucleon decay threshold. α decay, p decay, n decay, d decay and t decay were taken into account.

The predictions of the decay model are compared to the experimental data as shown in Fig.5.9 for (J^π, T)=$(1^-, 1)$ state (blue) and for (J^π, T)=$(2^-, 1)$ state (red).

The decay model reproduces the increasing trend of the emission probability, qualitatively, and is also consistent with the data quantitatively for 24 MeV< E_x <28 MeV, where the $\Delta T = 1$ excitation dominates (GDR and SDR) as discussed in Sec.5.1.1-5.1.3. But it fails to reproduce the data quantitatively for 18 MeV< E_x <24 MeV due to the $\Delta T = 0$ excitation. The authors of Ref.[47] mentioned the resonance at 18.4 MeV is dominated by ΔT=0 and ΔS=1 excitation. α decay from ΔT=1 excitation is suppressed due to the isospin conservation, while it is dominant for $\Delta T = 0$ excitation due to the lower separation energy ($S_\alpha = 7.37$ MeV). Moreover the α decay from ^{12}C is followed by 2α decay without γ-ray emission. Therefore the measured values for 18 MeV< E_x <24MeV are lower than the predictions which assume pure ΔT=1 excitation.

The decay model also predicts the difference of the emission probability between J^π=1^- state and J^π=2^- states to be large at E_x =19 MeV since only one $J^\pi = 1/2^-$ state of ^{11}B is involved. On the other hand, for $E_x > 21$ MeV, the differences become smaller since many excited states of daughter nuclei are involved.

5.2.2 Angular distribution of γ-ray emission probability

Angular distribution of the γ-ray emission probability has been obtained in the same way as the (p,p') cross section. Vertical angle (ϕ_t) cuts were applied with 0.8° steps (0°-0.8°, 0.8°-1.6°, 1.6°-2.4°, 2.4°-3.2°), while the horizontal scattering angle cuts were kept same ($0.0° < \theta_t < 0.5°$).

The angular distributions of γ-ray emission probability until E_x = 26MeV are shown in Fig.5.10. The systematic uncertainty of the γ-ray detection efficiency is not taken into account. The γ-ray emission probability increases as the scattering angle for $E_x > 20$ MeV where ΔT=1 dominates. Since the ratio of SDR to GDR increases as the scattering angle as discussed in Sec.5.1.2, the present data suggests that SDR has larger γ-ray emission probability than GDR.

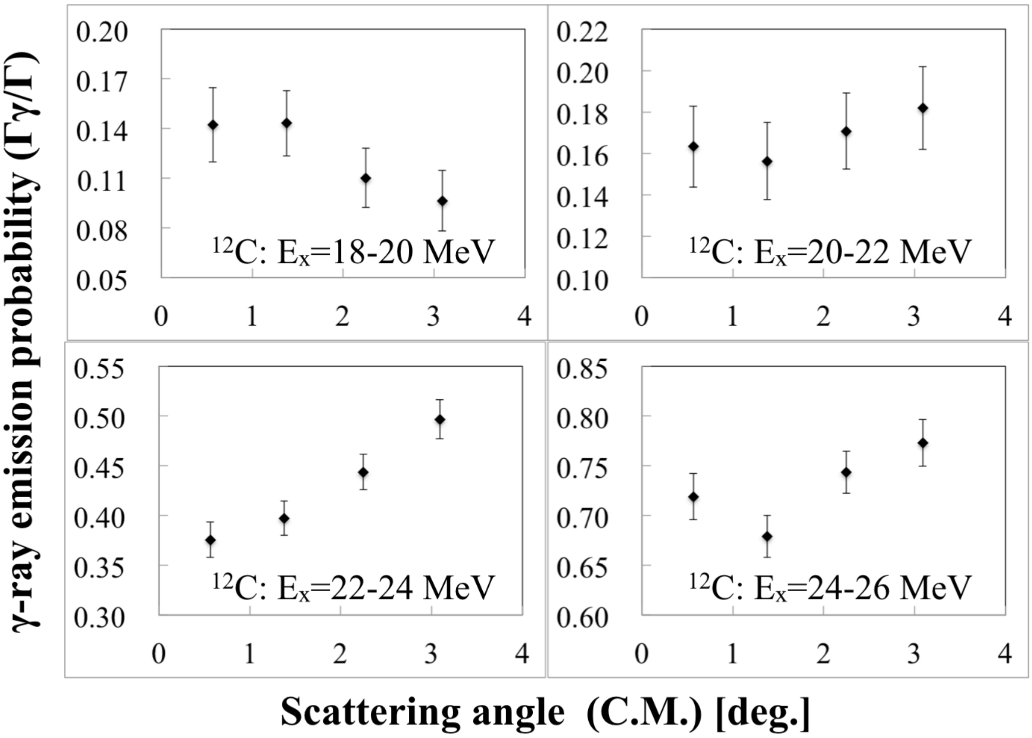

Figure 5.10: Angular distribution of γ-ray emission probability from the giant resonances of ^{12}C. Systematic uncertainty of the γ-ray detection efficiency is ignored (see text).

5.3 γ rays from giant resonances of ^{16}O

Figures 5.12-5.13 show the measured spectra after the background subtraction (black lines) and decomposed γ-ray spectra (colored dotted line) and the sum of them (red line). The γ-ray emission probability and its angular distribution were obtained in the same way as ^{12}C shown in Fig.5.11 and Fig.5.14, respectively, and summarized in Tab.A.1.

The most of the features are the same as ^{12}C. The emission probability increases as excitation energy until the separation energy for multi nucleons decay (S_{2p}=22.33MeV). No γ ray was clearly observed in $E_\gamma > S_p$=10.2 MeV (particle separation energy of daughter nuclei ^{15}N).

The difference is seen in the α decay channel because ^{16}O may decay into the excited states of daughter nuclei even for this channel followed by γ-ray emission. For 16 MeV $< E_x <$ 18 MeV, 4.43-MeV γ ray from the first excited state of ^{12}C after α decay is clearly observed, while the contribution of 5.27-MeV γ ray from the first exited state of ^{15}N after p decay is relatively small. Considering the α decay from ΔT=1 is prohibited by the isospin conservation, the giant resonances for 16 MeV $< E_x <$ 18 MeV are expected to be dominated by ΔT=0 excitation.

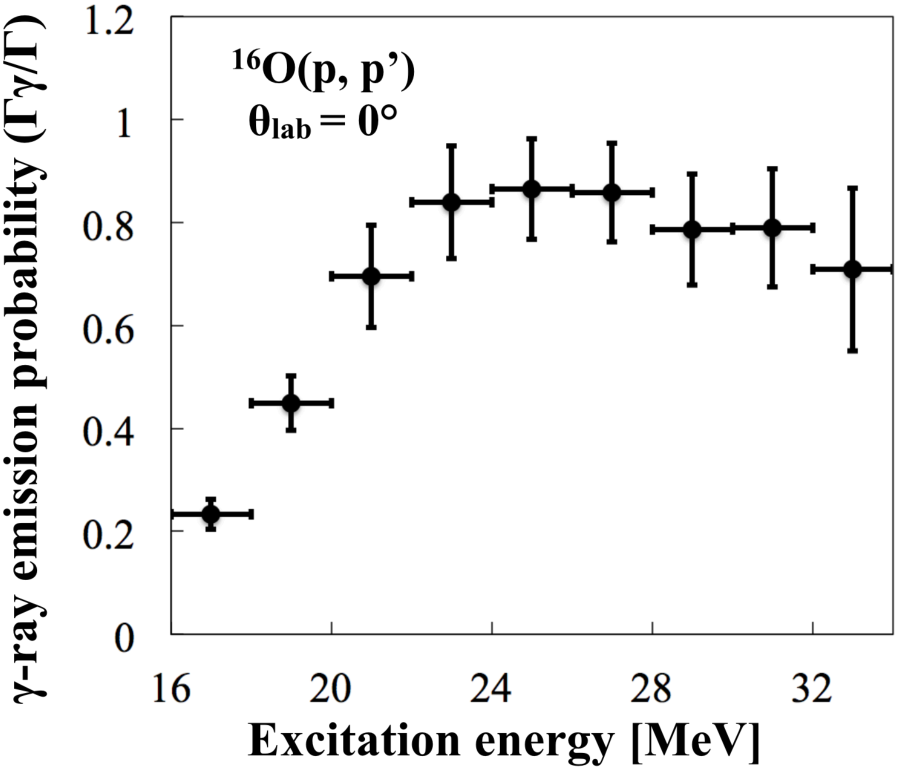

Figure 5.11: The γ-ray emission probability from giant resonances of ^{16}O.

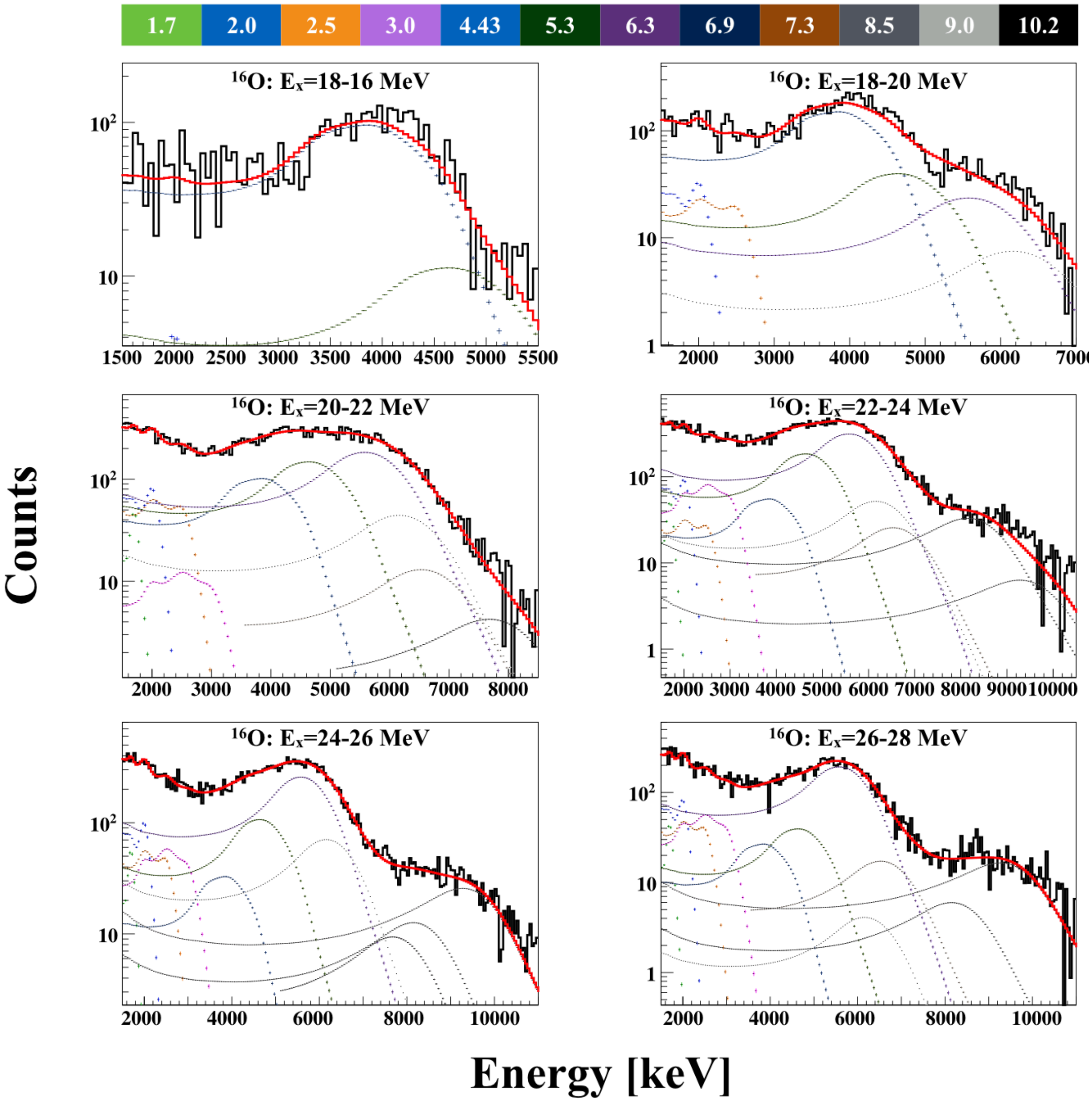

Figure 5.12: Same as Fig.5.7, but for ^{16}O at $E_x = 16 \sim 28$ MeV.

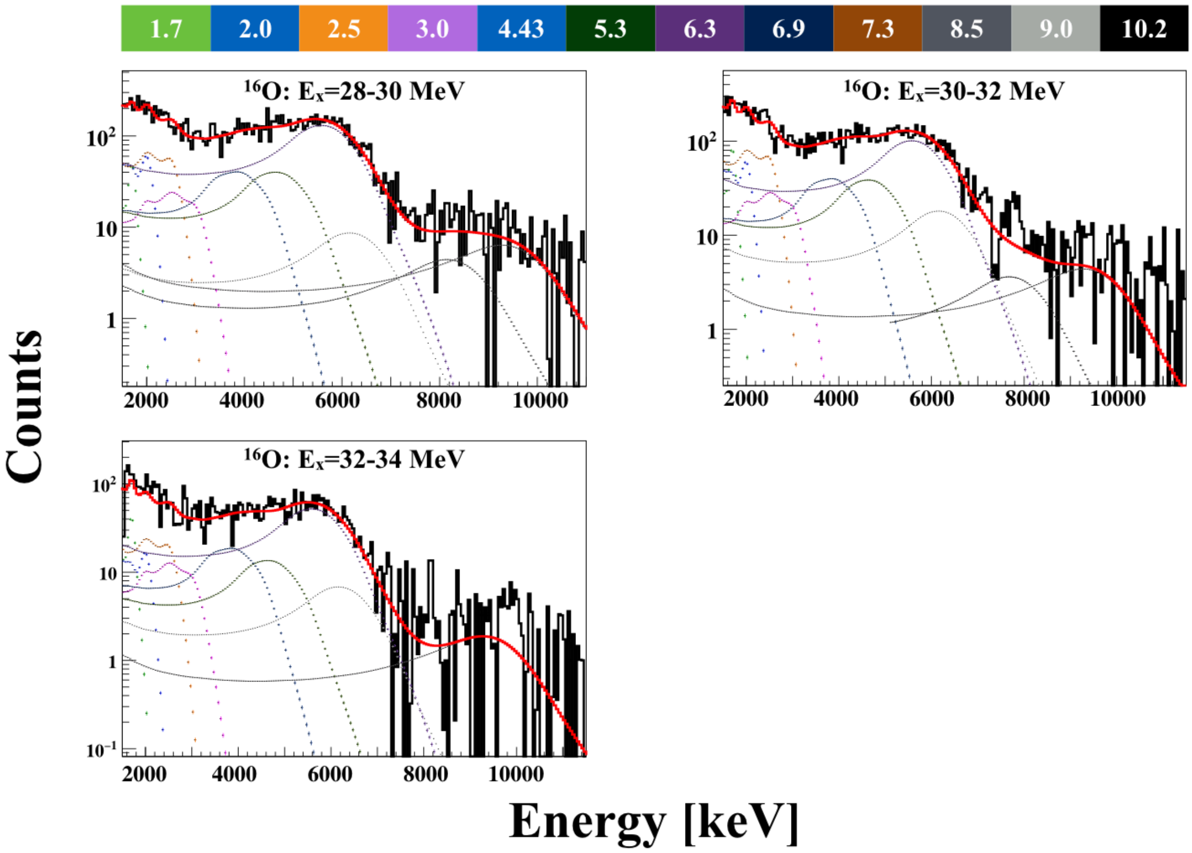

Figure 5.13: Same as Fig.5.7, but for ^{16}O at $E_x = 28 \sim 34$ MeV.

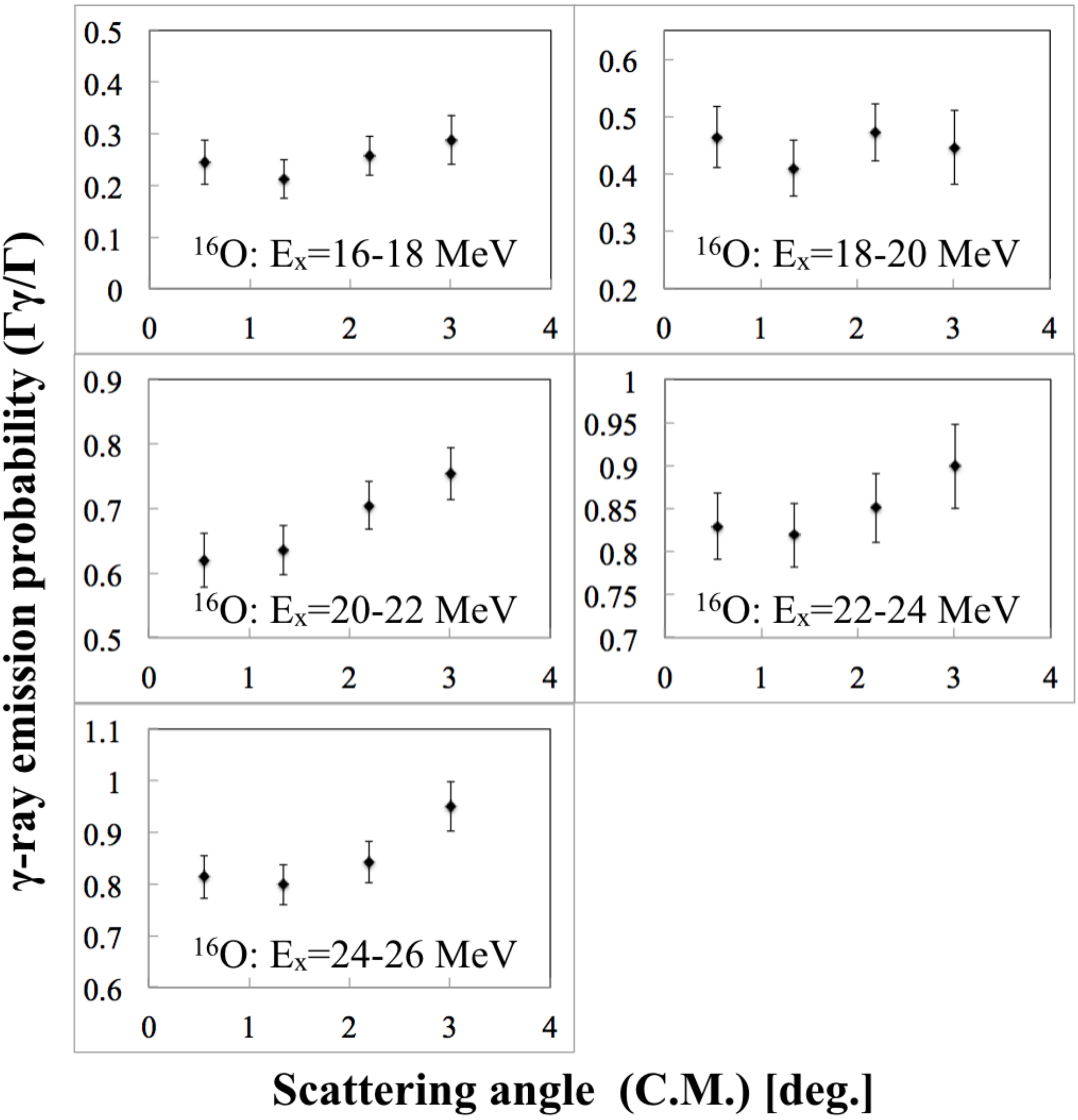

Figure 5.14: Same as Fig.5.10, but for ^{16}O.

Chapter 6

Estimation of supernova neutrino signals

The expected number of events (N_i) from a core-collapse supernova for a detection channel i can be estimated by

$$N_i = C \times Flux_{\nu_j} \times n_{target} \times \sigma_i, \quad Flux_{\nu_j} = C \frac{L_{\nu_j}}{\langle E_{\nu_j} \rangle} \frac{1}{4\pi D^2}, \tag{6.1}$$

where $Flux_{\nu_j}$ is the neutrino flux for ν_j in cm^{-2}, n_{target} is the number of targets, σ_i is the cross section for a reaction i in cm^2, C is the unit conversion constant (6.25×10^{-38} [MeV/erg$\cdot$(kpc/cm)^2]), L_{ν_j} is the total energy in erg, $\langle E_\nu \rangle$ is the mean energy in MeV and D is the distance from the earth in kpc.

The present results are applied for the estimation of N_{NC_γ} for Super Kamiokande (SK) and KamLAND together with CC inverse decay channel ($\bar{\nu}_e + p \rightarrow e^+ + n$) for a comparison. The assumptions and details are described below.

6.1 Assumptions and inputs

Neutrino flux

The NC events are assumed to be induced by only ν_x (ν_μ, ν_τ and their anti-particles), which follows Fermi Dirac distribution (FD) as

$$FD(E,T) = \frac{0.553}{T^3} \frac{E^2}{1 + \exp E/T}. \tag{6.2}$$

where E is the neutrino energy, T is the equilibrium temperature. $T_{\nu_e} = 3.5$ MeV, $T_{\bar{\nu}_e} = 5$ MeV, $T_{\nu_x} = 8$ MeV is assumed [55, 22, 23]. The mean energy $\langle E \rangle$ of Eq.(6.2) is related to T by $\langle E \rangle = 3.15 \times T$.

Total gravitational energy released from a supernova of $L = 3 \times 10^{53}$ erg is assumed (Eq.(1.40)) and carried away equally by all the species, that is, $L_{\nu_e} = L_{\bar{\nu}_e} = L_{\nu_x} = 5 \times 10^{52}$ erg. Fig.6.1 shows the flux for each species. The effect of neutrino oscillations is small and not taken into account (see Ikeda *et al.* [56] for detail). The distance from the galactic center of D =10 kpc is assumed.

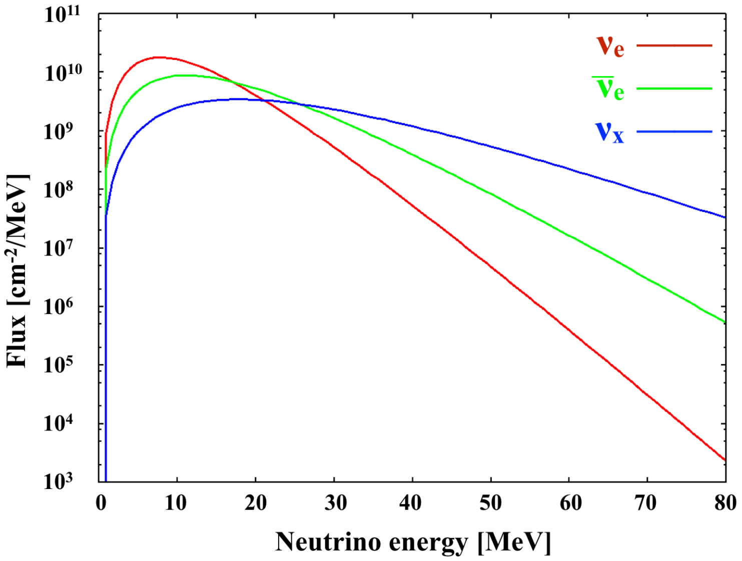

Figure 6.1: Neutrino flux from a core-collapse supernova at 10 kpc.

Number of targets in neutrino detectors

The number of ^{12}C ($n_{\rm C}$) and protons (n_p) in a 1-kton liquid scintillation detector (KamLAND) are 4.30×10^{31} and 8.60×10^{31}, respectively [57]. The number of ^{16}O ($n_{\rm O}$) and protons (n_p) in a 32.48-kton water-Cherenkov detector (Super Kamiokande) are 1.09×10^{33} and 2.17×10^{33}, respectively.

Cross section for the inelastic scattering of nuclei by neutrino followed by γ-rays emission

The differential inelastic scattering cross sections ($d\sigma_{NC}/dE_x$) for ^{12}C(ν,ν') and ^{16}O(ν,ν') folded by Fermi Dirac spectra with T= 8MeV were taken from Langanke *et al.* [24]. $d\sigma_{NC}/dE_x$ was further multiplied by γ-ray emission probability with energy higher than the detector threshold ($E_\gamma > 5$ MeV for SK and $E_\gamma > 0.2$ MeV for KamLAND) from the present data and integrated from the separation energy of neutron (S_p =15.96 MeV for ^{12}C and S_p =12.13 MeV for ^{16}O) up to 70 MeV to obtain the cross section of ^{12}C$(\nu,\nu'\gamma)$ and ^{16}O$(\nu,\nu'\gamma)$ as

$$\sigma_{NC\gamma} = \int_{S_p}^{70} \frac{d\sigma_{NC}}{dE_x} \times \frac{\Gamma_\gamma}{\Gamma}(E_x)dE_x. \tag{6.3}$$

Since $\frac{\Gamma_\gamma}{\Gamma}(E_x)$ is simply taken from the present data, the difference of the giant resonances induced by neutrino and proton inelastic scatterings are not taken into account.

$\sigma_{NC\gamma}$ was obtained to be 1.05 (± 0.10) $\times 10^{-42}$cm^2 for ^{12}C(ν,ν'). In $E_x > 34$ MeV, the emission probability is assumed to be constant. This assumption does not affect the result greatly (<10%) since the cross section for higher excitations is very small. On the other hand, the decay model calculation in the present work gives higher cross section ^{12}C$(\nu,\nu'\gamma)$ = 1.52 $\times 10^{-42}$cm^2 for $J^\pi = 1^-$ and 1.37 $\times 10^{-42}$cm^2 for $J^\pi = 2^-$ (for $E_x >$ 28MeV, $\frac{\Gamma_\gamma}{\Gamma}$ is taken from data).

In addition, the cross section for excitation to the 15.1 MeV state ($\sigma_{NC\gamma_{15.1}} = 3\times10^{-42}\text{cm}^2$) is taken from Kolbe *et al.*[24] with T = 8 MeV.

$\sigma_{NC\gamma}$ was obtained to be 1.61 ± 0.22 $\times10^{-42}\text{cm}^2$ for $^{16}\text{O}(\nu,\nu'\gamma)$. The decay model calculation performed by Langanke *et al.* [9] gives smaller value of 1.34 $\times10^{-42}\text{cm}^2$.

The cross sections are summarized in Tab.6.1.

Table 6.1: The inelastic scattering cross sections induced by supernova neutrinos [24] (T = 8 MeV) and those with γ-rays emission. γ-rays with energy higher than the detector threshold are taken into account ($E_\gamma > 5$ MeV for ^{12}C and $E_\gamma > 0.2$ MeV for ^{16}O).

target	σ_{NC} [10^{-42}cm^2]	$\sigma_{NC\gamma}$ [10^{-42}cm^2]	$\sigma_{NC\gamma_{15.1}}$ [10^{-42}cm^2]
^{12}C	3.84	1.05 ± 0.10	3.00
^{16}O	4.48	1.61 ± 0.22	—

Cross section for inverse β decay reaction

The cross section for CC inverse β decay reaction ($\sigma_{CC}(E_\nu)$) is taken from Strumia and Vissani [58] and is shown in Fig.6.2. The cross section is further weighted by the Fermi Dirac distribution with T = 5 MeV and integrated up to E_ν = 200 MeV to obtain $\sigma_{CC} = 2.26\times10^{-41}\text{cm}^2$.

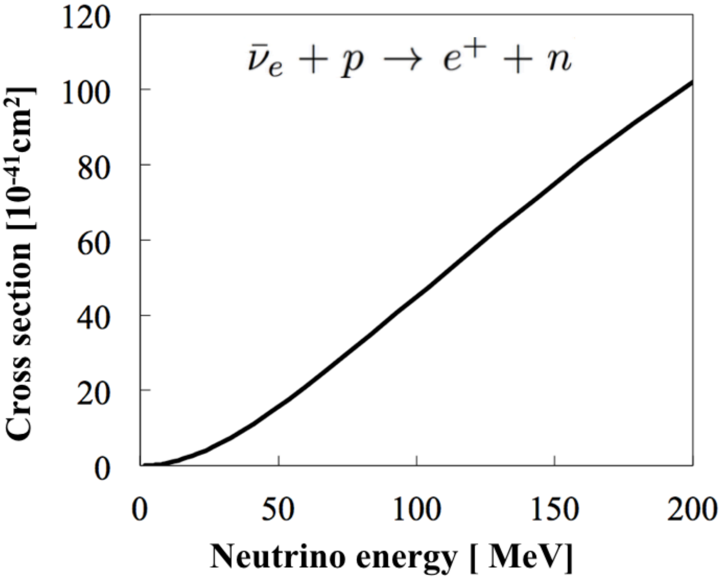

Figure 6.2: The cross section of CC inverse β-decay reaction [58].

6.2 Expected number of events

The expected number of events estimated by Eq.(6.1) is summarized in Tab.6.2.

The expected number of NC events from giant resonances for liquid scintillator type neutrino detector is estimated for the first time to be 19±2. Only the 15.1 MeV γ ray from the 15.1

Table 6.2: Expected number of events for a core-collapse supernova at 10 kpc. Uncertainly of the measured emission probability is shown for NC event. γ rays with energy higher than the detector threshold are taken into account ($E_\gamma > 5$ MeV for SK and $E_\gamma > 0.2$ MeV for KamLAND).

Detector	Interaction	Reaction	N_i
KamLAND	CC	$\bar{\nu}_e + p \to e^+ + n$	321
	NC	$\nu_x + {}^{12}\mathrm{C} \to \nu_\mathrm{x} + \gamma_{15.1} + {}^{12}\mathrm{C}$	53
	NC	$\nu_x + {}^{12}\mathrm{C} \to \nu_\mathrm{x} + \gamma + \mathrm{X}$	19±2
Super Kamiokande	CC	$\bar{\nu}_e + p \to e^+ + n$	8120
	NC	$\nu_x + {}^{16}\mathrm{O} \to \nu_\mathrm{x} + \gamma + \mathrm{X}$	724±99

MeV state has been taken into account before (58 events) (see Tab.1.7 and Suzuki *et al.* [23]). The present work shows that notable number of γ rays from giant resonances are detectable and should be taken into account.

The expected number NC events for SK is estimated to be 724±100 events. Although the assumptions used in the present work are different from Beacom *et al.* [22], the number of the present work is consistent with their value of 710.

Chapter 7

Summary and Conclusion

A core-collapse supernova emits all types of neutrinos with mean energy of 10-20MeV, which carry away nearly 99% of the total gravitational energy. These neutrinos can be detected by existing neutrino detectors such as Super Kamiokande (water, H_2O) and KamLAND (liquid scintillator, $C_{12}H_{26}$). The main signal is induced by CC inverse β decay reaction with proton ($\bar{\nu}_e + p \to e^+ + n$) and sensitive only to $\bar{\nu}_e$. The 2nd largest signal comes from NC inelastic scattering of neutrinos and anti-neutrinos with ^{12}C and ^{16}O. NC events are dominated by ν_μ and ν_τ and their anti-particles, since their mean energies are higher than those of ν_e and $\bar{\nu}_e$. Therefore, the detection of NC events is important for understanding of the underlying mechanism of supernova explosion.

^{12}C and ^{16}O are excited to giant resonances through NC ν-^{12}C and ν-^{16}O inelastic scatterings. Since giant resonances are located above the particle emission threshold, they decay by particle emission into daughter nuclei. The decay model predicts that γ ray will be emitted when the parent nucleus decay to the excited states of daughter nuclei. NC events can be identified by detecting these γ rays. However there have been no systematic experimental data of the γ-ray emission from giant resonances of ^{16}O and ^{12}C

We have carried out an experiment at RCNP (Osaka Univ.) in 2014 to measure γ rays from giant resonances of ^{16}O and ^{12}C using 392 MeV proton beam and magnetic spectrometer "Grand Raiden" to excite the target to the giant resonances and an array of NaI(Tl) γ-ray counters.

The purposes of the experiment are summarized as follows.

1. Tagging the giant resonances by (p,p') inelastic scattering and measurement of the γ rays from them.
2. Study of the γ-ray emission mechanism.
3. Verification of the decay model.
4. Estimation of number of NC events from a core-collapse supernova.

From the spectrometer analysis, differential cross section and angular distribution for (p, p') inelastic scattering are obtained. Giant resonances are clearly observed in 16 MeV$< E_x <$34 MeV. The non spin-flip cross section above $E_x = 20$ MeV, which is about 60% of the total cross section, is consistent with the Coulomb excitation cross section converted from the photoabsorption cross section using virtual photon method. This shows that the observed giant resonances are dominated by giant dipole resonance (GDR, $J^\pi = 1^-$, T=1). The obtained angular distribution of the cross section is also consistent with the DWBA calculations for GDR.

The coincidence γ-ray spectra from the well-known discrete states gated by E_x in the spectrometer analysis were used for the calibration of γ-ray detector. The accidental background is subtracted successfully using the time information between the spectrometer and γ-ray detector. The shape of energy spectra and the detection efficiencies are well reproduced by the Monte Carlo detector simulation with 5% uncertainty level.

The final conclusions from the analysis of the γ rays from giant resonance analysis are summarized as follows:

1. The energy spectrum of γ rays from giant resonances of ^{12}C and ^{16}O and the emission probability ($\Gamma_\gamma/\Gamma(E_x)$) have been measured for the first time as a function of excitation energy (E_x).

2. The γ-ray energy spectra clearly show that γ rays are emitted from the excited states of the daughter nuclei after particle decay of the parent nuclei, while the direct γ-decay with emission of high energy γ rays was not clearly observed.

3. The γ-ray emission probability increases as excitation energy up to $\Gamma_\gamma/\Gamma(E_x)$=0.69±0.05 for ^{12}C at E_x=27 MeV and 0.87±0.10 for ^{16}O at E_x=23 MeV until the energy threshold for two nucleons decay, and then decreases gradually.

4. The γ-ray emission probability has been further estimated for each proton scattering angle ($\theta_p = 0^\circ \sim 3^\circ$) for 16 MeV< E_x <26 MeV. For $E_x > 20$ MeV, it is found to increase as the scattering angle. Previous experiments found that non-spin-flip dipole excitation (GDR) dominates at scattering angle around 0°, while spin-flip dipole excitation (SDR) dominates at scattering angle around 3°. Considering the previous results, the data suggest qualitatively that SDR has larger γ-ray emission probability than GDR.

5. General features of γ-ray emission from ^{16}O are similar to those of ^{12}C since both nuclei are even-even nuclei with closed shell configuration. Difference was observed in the α-decay. ^{16}O can further emit γ ray after α-decay, while ^{12}C decays by 3α emission without γ-ray emission. This is clearly seen in the energy spectrum of ^{16}O for 16 MeV< E_x <18 MeV. Since the α-decay is not allowed for ΔT=1 due to the isospin conservation, the giant resonance in this region is expected to be dominated by ΔT=0 excitation.

6. Decay model calculation based on Hauser-Feshbach formalism has been performed for ^{12}C until the energy threshold for multi-nucleon decay. The decay model reproduces the increasing trend of the emission probability, qualitatively and is also consistent with the data quantitatively for 24 MeV< E_x <28 MeV where $\Delta T = 1$ excitation dominates.

Using the present results, the number of NC events from a core-collapse supernova at 10 kpc has been estimated to be 19±2 for KamLAND for the first time, and 724±99 for Super Kamiokande, which is consistent with the number of 710 estimated by the previous study based on a pure theoretical calculation by J. F. Beacom et. al [22] (, uncertainty of which is estimated by Ikeda *et al.* for SK collaboration [56] to be factor of two). The difference of the giant resonances induced by neutrino and proton inelastic scattering reactions will be taken into account in future study.

Acknowledgments

I would like to express the deepest appreciations to the supervisor, Prof. M. Sakuda and the collaborator, Prof. A. Tamii. They are the spokespersons of the experiment and gave me a great opportunity to study the interesting subject, constructive suggestions and continuous supports for my whole research activities. It was a great honor to work and discuss the physics with them.

I am also grateful to the co-supervisors, Prof. H. Ishino and Y. Koshio for incisive comments.

I want to thank all the laboratory students and stuff for making the research life rich in motion, especially to: Dr. T. Yano, Dr. T. Mori, Mr. Y. Yamada, Mr. A. Okamoto, Mr. T. Kayano., Mr. D. Fukuda, Mr. K. Hagiwara, Mr. T. Nagata, Mr. T. Funaki and1 Mr. T. Sudo.

I am deeply grateful to all the collaborator of RCNP-E398 experiment: Mr. T. Sudo, Mr. M. S. Reen, Dr. R. Dhir, Prof. M. Sakuda, Mr. Y. Yamada, Mr. D. Fukuda, Mr. T. Shirahige, Prof. Y. Koshio, Dr. T. Mori, Prof. A. Tamii, Dr. C. Iwamoto ,Mr. T. Ito ,Mr. M. Miura, Mr. T. Yamamoto, Prof. N. Aoi, Prof. E. Ideguchi, Prof. T. Suzuki, Prof. M. Yosoi, Prof. T. Kawabata, Dr. S. Adachi, Mr. T. Furuno, Ms. M. Tsumura, Mr. M.Murata, Prof. H.Akimune, Dr. T.Yano and Prof. H. Nakada. The success of the experiment owes deeply to their enormous helps and valuable advices.

I would like to give special thanks to Mr. Y.Yamada, Mr. D. Fukuda and Mr. T. Shirahige for the huge contribution during the experimental period and Mr. M. S. Reen and T. Sudo for the huge contirbution in the γ-ray detector analysis.

This work is supported by JSPS Grant-in-Aid for Scientific Research on Innovative Areas (Research in a proposed research area) No. 26104006. I acknowledge the generous financial support from the JSPS Research Fellowship for Young Scientists No. 15J07923.

Finally, I would also like to express my heartfuelt gratitude to my family for their moral support and warm encouragement.

Appendix A

Data table

A.1 γ-ray emission probability from giant resonances

Table A.1: γ-ray emission probability from giant resonances of ^{12}C.

E_x [MeV]	Γ_γ/Γ ± stat. ± sys.
16 - 18	0.017 ± 0.001 ± 0.011
18 - 20	0.111 ± 0.001 ± 0.010
20 - 22	0.138 ± 0.001 ± 0.010
22 - 24	0.355 ± 0.002 ± 0.020
24 - 26	0.615 ± 0.003 ± 0.041
26 - 28	0.692 ± 0.003 ± 0.048
28 - 30	0.558 ± 0.003 ± 0.048
30 - 32	0.487 ± 0.003 ± 0.045
32 - 34	0.452 ± 0.005 ± 0.076

Table A.2: γ-ray emission probability from giant resonances of ^{16}O.

E_x [MeV]	Γ_γ/Γ ± stat. ± sys.
16 - 18	0.233 ± 0.004 ± 0.029
18 - 20	0.449 ± 0.004 ± 0.053
20 - 22	0.696 ± 0.004 ± 0.099
22 - 24	0.839 ± 0.004 ± 0.109
24 - 26	0.865 ± 0.005 ± 0.098
26 - 28	0.858 ± 0.006 ± 0.096
28 - 30	0.787 ± 0.007 ± 0.108
30 - 32	0.790 ± 0.007 ± 0.115
32 - 34	0.709 ± 0.009 ± 0.158

Appendix B

Drawings

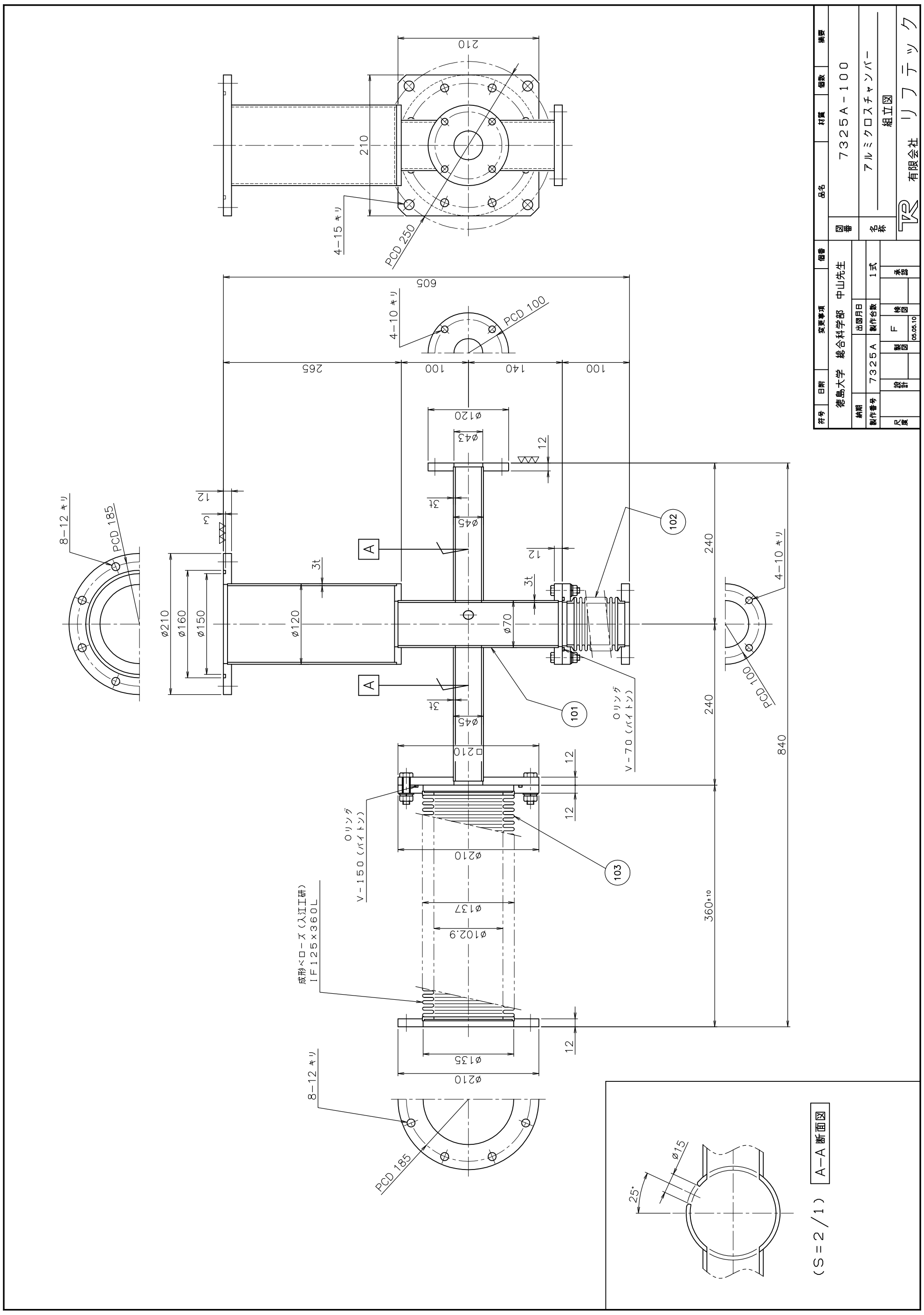

Figure B.1: Drawing of the aluminum scattering chamber.

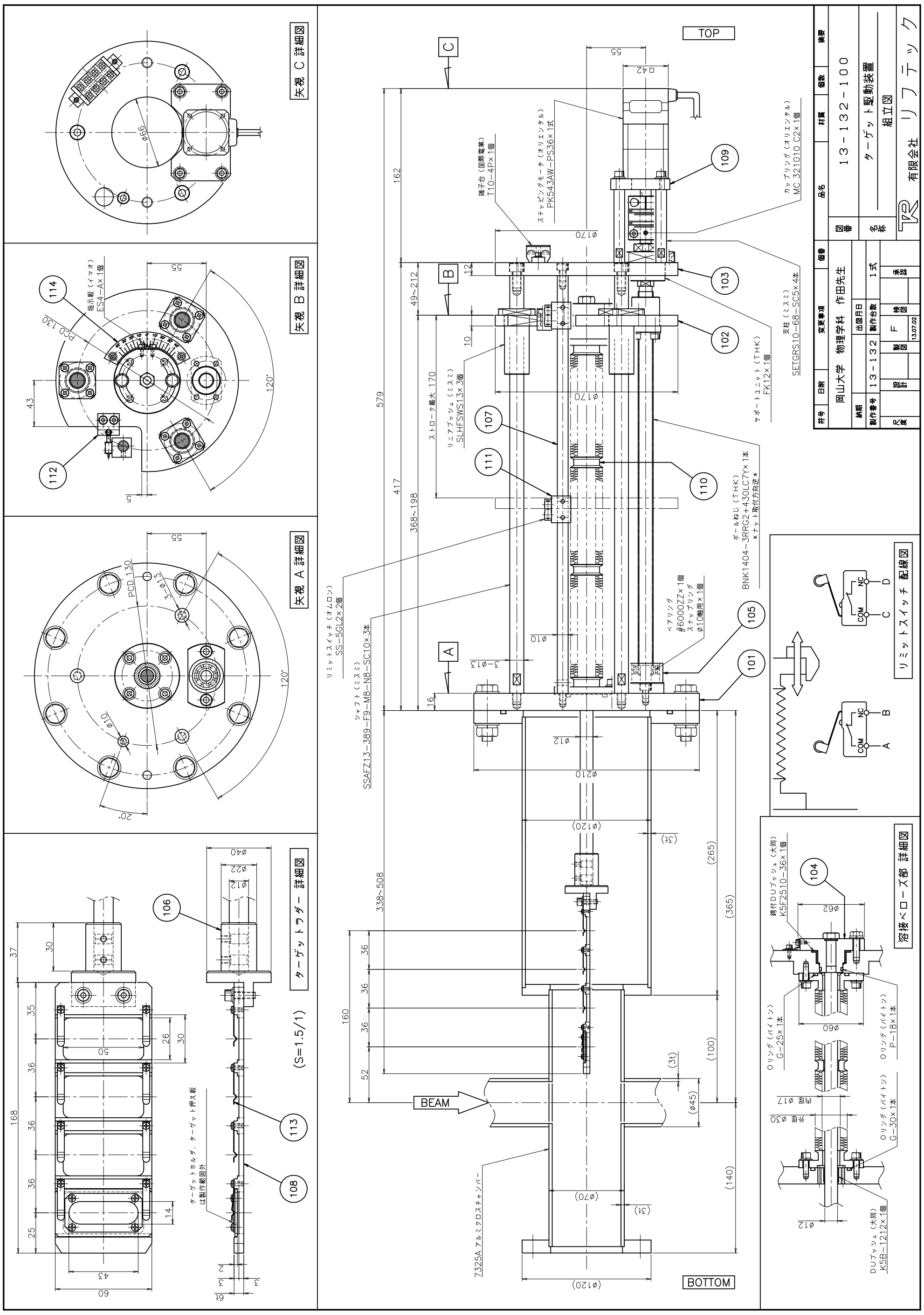

Figure B.2: Drawing of the electric target ladder system.

Bibliography

[1] M. N. Harakeh and A. van der WOUDE: Giant Resonances Fundamental High-Frequency Models of Nuclear Excitation (Oxford University Press, 2001).

[2] 八木浩輔: 基礎物理学シリーズ 4　原子核物理学 (朝倉書店、 1971).

[3] 市村宗武・坂田文彦・松柳研一: 岩波講座　現代の物理学　第 9 巻 原子核の理論 (岩波書店、1993).

[4] K. W. Jones, C. Glashausser, R. de Swiniarski, S. Nanda, T. A. Carey, W. Cornelius, J. M. Moss, J. B. McClelland, J. R. Comfort, J.-L. Escudie, M. Gazzaly, N. Hintz, G. Igo, M. Haji-Saeid, and C. A. Whitten, Jr.: Phys. Rev. C **33** (1986) 17

[5] S. Hama, B. C. Clark, E. D. Cooper, H. S. Sherif, and R. L. Mercer: Phys. Rev. C **41** (1990) 2737

[6] W. Bothe and W. Gentner: Z. Phys. **71** (1937) 236.

[7] P.F. Bortignon, A. Bracco and R. A. Broglia: Ginat Resonances Nuclear Structure at Finite Temperature (Harwood Academic Publishers, 1998).

[8] Table of Isotopes: 1999 Update with CD-ROM, edited by R. B. Firestone, C. M. Baglin, and S.Y. F. Chu (Wiley, New York, 1999), 8th ed.

[9] K. Langanke, P. Vogel, and E. Kolbe: Phys. Rev. Lett. **76** (1996) 2629.

[10] F.Puhlhofer: Nucl.Phys. A**280** (1977) 267.

[11] Wilmore, D.Hodgson Nucl. Phys A**55** (1964) 673.

[12] Becchetti, F.D.Greenless: Phys. Rev. **182** (1969) 1190.

[13] Huizenga, Igo: Nucl. Phys. **29** (1962) 462.

[14] CEA 2380 (1963); CEA 2379 (1963).

[15] H. A. Bethe: Rev. Mod. Phys. **62** (1990) 801.

[16] S. L. Shapiro and S. A. Teukolsky: Black Holes White Dwarfs, and Neutron Stars (Wiley Interscience, New York, 1992).

[17] M. Fukugita and A. Suzuki: Physics and Astrophysics of Neutrinos (Springer-Verlag Tokyo,1994).

[18] K. Nakazato *et al.*: Astrophys. J. Supp. **205** (2013) 2.

[19] IAU circular No. 4316, International Astronomical Union (1987).

[20] K. Hirata *et al.*: Phys. Rev. Lett. **58** (1987) 1490.

[21] R. M. Bionta *et al.*: Phys. Rev. Lett. **58** (1987) 1494.

[22] J. F. Beacom and P. Vogel: Phys. Rev. D **58** (1998) 053010.

[23] A. Suzuki: Nucl. Phys. B (Proc.Suppl.) **77** (1999) 171.

[24] E. Kolbe, K. Langanke, S. Krewald, and F.-K. Thiele-mann: Nucl. Phys. A**540** (1992) 599.

[25] N. Jachowicz, S. Rombouts, K. Heyde, and J. Ryckebusch: Phys. Rev. C **59** (1999) 3246.

[26] A. Botrugno and G. Co: Eur. Phys. J. A **24**,s1 (2005) 109.

[27] T. Suzuki: AIP Conf. Proc. **1663** (2015) 050001.

[28] KARMEN Collaboration: Phys. Lett. **50** (1979).

[29] Y. S. Horowitz, D. B. Mcconnell, J. Ssengabi and N. Keller: Nuc. Phys. A**151** (1970) 161.

[30] K.J.R. Rosman, P.D.P. Taylor: Pure Appl. Chem. **71** (1999) 1593.

[31] M. Fujiwara *et al.*: Nuclear Instruments and Methods in Physics Research A **422** (1999) 484.

[32] P. Ludwig, R. Geller and G. Melin: Review of Scientific Instruments **63** (1992) 2892.

[33] H. Fujita *et al.*: Nucl. Instrum. Methods Phys. Res. A **469** (2001) 55.

[34] I. Ou *et al.*: AIP Conf. Proc. **1663** (2015) 120012.

[35] I. Ou *et al.*: JPS Conf. Proc. **12**, 010048 (2016) 1.

[36] S. Agostinelli *et al.*: Nucl. Instrum. Meth. A**506** (2003) 250.

[37] A. Tamii *et al.*: IEEE Trans. on Nuc. Sci. **43** (1996) 2488.

[38] T. Kawabata *et al.*: Phys. Rev. C **65** (2002) 064316.

[39] F. Ajzenberg-Selove: Nucl. Phys. A**506** (1990) 1.

[40] F. Zijderhand and C. Van Der Leun: Nuc. Phys. A**460** (1986) 181.

[41] F. Fleurot *et al.*: Physics Letters B **615** (2005) 167.

[42] A. Tamii *et al.*: Nuclear Instruments and Methods in Physics Research A **605** (2009) 326.

[43] C.A. Bertulani and A.M. Nathan: Nucl. Phys. A**554** (1993) 158.

[44] J. Ahrens et. al. Nucl. Phys. A**251** (1975) 479.

[45] A.M. Krumbholz *et al.*: Phys. Lett. B **744** (2015) 7.

[46] A. Tamii, P. von Neumann-Cosel, I. Poltoratska: Eur. Phys. J. A **50** (2014) 28.

[47] A. Tamii *et al.*: Physics Letters B **459** (1999) 61.

[48] Herman Feshbach: Theoretical Nuclear Physics Nuclear Reaction (Wiley, New York, 1992).

[49] T. Kawabata.: Doctoral thesis, Kyoto University (2002).

[50] F. T. Baker *et al.*: Phys. Rev. C **48** (1993) 1106.

[51] J. Raynal: program code "DWBA07" NEA-1209/08.

[52] M.A. Franey W.G. Love: Phys. Rev. C **31** (1985) 488.

[53] S. Cohen and D. Kurath: Nucl. Phys. **73** (1965) 1.

[54] S. Y. van der Werf: program code "NORMOD" unpublished.

[55] H. -T. Janka: Comf. Proc. Vol. **40** *"Frontier Objects in Astrophysics and Particle Physics"* , edited by F. Giovannelli and G. Mannocchi, Workshop in Vulcano, Italy, 18-23 May 1992, Italian Physical Society, Bologna, Italy (1993) 345.

[56] M. Ikeda *et al* for Super Kamiokande collaboration: Astrophys. J. **669** (2007) 519.

[57] KamLAND collaboration: Phys. Rev. C **84** (2011) 035804.

[58] A. Strumia and F. Vissanib: Phys. Lett. B **564**, Issue 1-2 (2003) 42.